Politecnico di Torino

Master of Science in Mechanical Engineering

Master Thesis

Thermofluidynamic numerical simulation of microchip cooling devices

A thesis in cooperation with the National Institute for Nuclear Physics (INFN)
and the European Organization for Nuclear Research (CERN)

Supervisors

Prof. Vladimir Viktorov

Prof. Carlo Ferraresi

Dott. Flavio Marchetto

Author

Gabriele Ceglia

Abstract

Thermofluidynamic numerical simulation of microchip cooling devices

NA62 is a particle physics experiment that investigates new physics at CERN SPS accelerator. The aim of this experiment is to measure the rate of kaon decay $K^+ \rightarrow \pi^+ \nu \bar{\nu}$ in order to compare the experimental data with the Standard Model theory. Time, direction, and momentum of the incoming kaon beam are accurately recorded by the GTK spectrometer. The GTK is located into a vacuum chamber and a very low material budget is required to minimize beam interactions. The readout electronics dissipate a lot of thermal power that must be managed by an efficient cooling system in order to keep the temperature of the silicon pixel tracking detectors below 5°C. Indeed, it has been observed that it is possible to reduce maintenance operations and guarantee high performance of the detectors by keeping the temperature below the limit. The goal is achieved by implementing an innovative microchannel heat sink called “Cooling Plate”. Microfabrication techniques are explored to understand how microchannels are etched into the thin silicon wafer and how they are bonded on top. CFD simulations are performed to analyze the thermofluidynamic behavior of the system and empirical tests are carried out to validate the numerical solutions and assess the operating conditions of failure. Furthermore, two alternative updated layouts of the cooling system with zero material budget are proposed. CFD simulations show the best solution taking the first steps towards the new configuration of the GTK heat sink, called “Cooling Frame”.

Contents

List of abbreviations

CERN European Organization for Nuclear Research

NA62 North Area 62

LHCb Large Hadron Collider beauty

GTK Gigatracker

PCB Printed circuit board

ASIC Application specific integrated circuit

MUV Muon veto system

LAV Large angle veto system

SAV Small angle veto system

IRC Intermediate-ring calorimeter

LKr Liquid Krypton calorimeter

CHANTI Charged anti-coincidence detector

KTAG Kaon tagger

LHC Large hadron collider

RICH Ring-imaging Čerenkov

CEDAR Differential Čerenkov counter

HPD Hybrid pixel detector

MCHS Microchannel heat sink

CFD Computational fluid dynamic

DRIE Deep reactive-ion etching

SOI Silicon on insulator

MEMS Micro electro-mechanical systems

HEP High energy physics

EoC End of column

CTE Coefficient of thermal expansion

CAD Computer aided design

CMP Chemical mechanical polishing

SEM Scanning Electron Microscope

NSF Navier Stokes Fourier

SPS Super proton synchrotron

SM Standard model

1. Introduction

1.1 Motivation of the study

In recent years the continuous increase in power and the reduction in the size of electronic devices requires cooling systems capable of dissipating more and more heat [1]. Consequently, new ways of cooling have been investigated to keep pace with this rapidly changing technology. Thanks to their compactness and high heat removal rate, microchannel heat sinks play a primary role in this scenario. Nowadays MCHS are widely used in many fields such as high power electronics, the aerospace industry, automotive heat exchangers, but they are also subject of interest in the field of scientific research [2].

In this context, CERN [3] has gained some interest in this innovative technology so that its experiments can benefit from these cooling systems. Microchannel devices have been successfully implemented so far, respectively in the NA62 and LHCb experiments [4], but much effort is still being made to achieve improvements and to extend their use to other projects. For this purpose, numerical analysis and experimental tests are essential to understand the potential of the system and take full advantage of this technology.

In this dissertation, the mentioned studies are dealt through CFD simulations to predict the thermofluidynamic behavior of the currently employed heat sink in different operating conditions and to design new cooling solutions refining experimental measurements. Specifically, this thesis concerns the pioneering application of microchannels to the electronics cooling system of the GTK spectrometer of NA62 experiment particle detector [5].

1.2 NA62 experiment

CERN [3] is one of the major particle physics laboratories in the world that houses some of the most cutting-edge scientific experiments currently underway. Here, researchers investigate HEP by observing elementary particles and their fundamental interactions to understand the nature of our universe [3]. Large amounts of kinetic energy are usually provided to subatomic particles in accelerators where collisions between these particle beams are observed by means of detectors in order to discover unknown entities. Alternatively, it is possible to indirectly search for the unknown by measuring rare events that are well estimated by theoretical models and searching for any discrepancies. This last working approach is pursued by the NA62 collaboration, that investigates "New Physics" by looking for deviations from the Standard Model by measuring a rare event with very high precision [6].

NA62 is a fixed-target experiment at the CERN SPS accelerator whose goal is to measure the branching ratio of the very rare kaon decay $K^+ \to \pi^+ \nu\bar{\nu}$ [7]. SM theory provides a very precise value of the branching ratio $0.84^{+0.1}_{-0.1}$ with only ten percent uncertainty, therefore this decay channel occurs about once every ten billion kaon decay events [7]. On the other hand, the experimental measurements carried out so far in other experiments are not as accurate [8]. Last experiment in Brookhaven measured a branching ratio equal to $1.73^{+1.15}_{-1.05}$ [7] by slowing down the loaded K until it stopped completely within an "active target" [9]. In contrast, NA62 collaboration has been planning to achieve better results falling within the 10% of uncertainty theoretically predicted, by observing the decays of the charged "in flight" K, thus increasing the chances of new findings [7]. Specifically, it is required to register around 100 events with these specifications in a few years of data collection, achieving a good estimate of the branching ratio to be then compared to the theoretical value [7].

1.2.1 NA62 setup

However, to put this new strategy into practice a very complex experimental setup is needed.

Figure 1 NA62 setup location at CERN [10]

NA62 setup is located at the CERN North Area, Prevessin District. The experiment is served by the SPS accelerator that accelerates protons for LHC and other projects including NA62 [6]. A 75 GeV/c beam is generated through the collision between a 400 GeV proton beam and a beryllium target [7]. The K^+ is characterized by several possible decay channels that occur more and more frequently, whose background signals must be finely rejected [10].

Main decay channels	Branching ratio
$K^+ \rightarrow \mu^+\nu$	63 %
$K^+ \rightarrow \pi^+\pi^0$	21%
$K^+ \rightarrow \pi^+\pi^+\pi^-$	6%
$K^+ \rightarrow \pi^0 e^+\nu$	5%
$K^+ \rightarrow \pi^0\mu^+\nu$	3%
$K^+ \rightarrow \pi^+\pi^0\pi^0$	2%

Table 1 Main decays channels [10]

The $K^+ \rightarrow \pi^+\nu\bar{\nu}$ channel is easily identified thanks to its decaying nature. Indeed, the charged kaon produces a single pion and two "invisible" neutrinos, detected looking at the missing energy between input and output species [10].

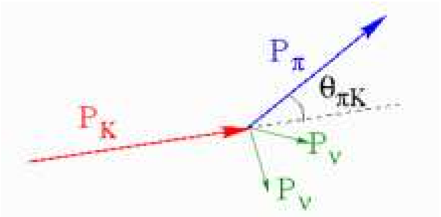

Figure 2 Main decay kinematic scheme [10]

To highlight the desired signal from the background, a series-mounted variety of detectors are implemented. Kinematic analysis, conservation laws and physical phenomena such as the Cherenkov effect represent effective means for identifying photons, pions, muons and electrons, distinguishing them from the background [10]. In this regard, a cylindrical 270 m long high vacuum (10^{-7} mbar) [5] environment has been created to confine the particles, minimizing possible beam interactions [6].

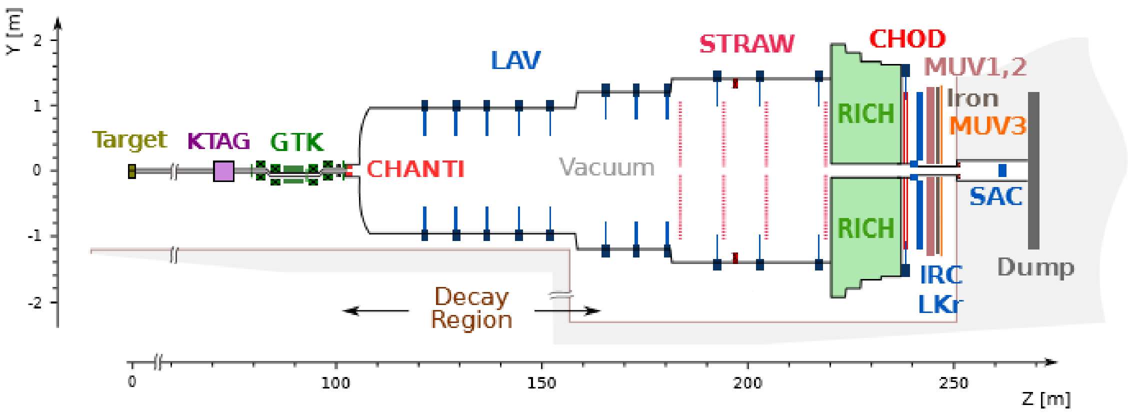

Figure 3 NA62 setup scheme [5]

The experiment setup starts with beryllium target where the charged kaon beam is spilled and identified by a CEDAR differential Cherenkov counter, flanked to the KTAG photon detection system [7]. At this stage, the kinematic properties of the incoming beam are accurately measured by the GTK spectrometer which will be examined in detail in the next paragraph. Any unwanted particles due to inelastic interactions in the previous sector are discarded by CHANTI [6]. A 65 m long decay region is set just over the CHANTI and from this point on, pions are detected by STRAW and RICH as long as all the decays channels containing a photon or a muon are excluded by the rest of the detectors, until the dump of the beam [6].

Figure 4 NA62 setup

1.2.2 NA62 GTK

The GigaTracker spectrometer measures kinematic quantities such as direction, momentum, position and time of the incoming beam particles before entering the decay area [5]. It consists of three planar silicon pixel matrix stations arranged around an appropriate bending magnet configuration and placed into a vacuum environment [5]. The beam is vertically deflected towards the GTK2 allowing the measurement of the momentum, meanwhile the GTK1 and

GTK3 provide the positions of crossing particles necessary to extract information regarding the direction [5].

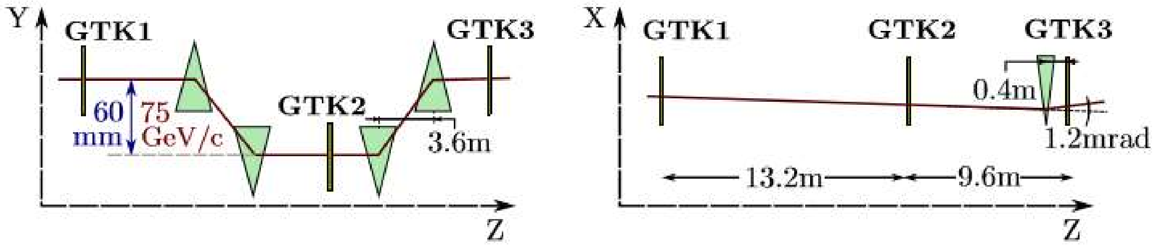

Figure 5 GTK beam deflection [5]

To track the 0.75GHz beam rate, the GTK is equipped with a dedicated electronic device designed to deliver a 150 ps hit time resolution, withstanding a strongly radiative environment [5]. Each station is composed of a silicon HPD bonded to two rows of five ASIC readout chips, called TDCpix [5]. In more detail, the bonding between the 18000 pixels of the sensor and the TDCpix array is realized interposing an equal number of solder bumps made of SnAg alloy, whereas the whole electronic equipment is stick to the cooling device by means of a thin epoxy glue layer [5].

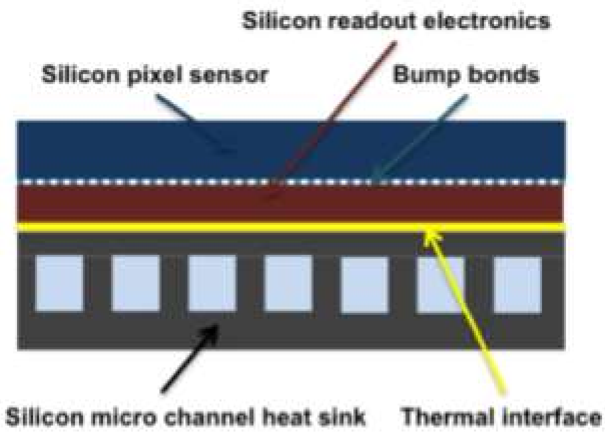

Figure 6 GTK detector assembly [8]

The cooling system has the purpose of removing the heat produced by the reading electronics and by the sensor from the assembly and therefore to ensure high operating performance by reducing leakage currents [5]. It has indeed been shown that by reducing the operating temperature of the sensor it is possible to increase its lifetime and consequently to reduce the number of maintenance operations [5]. Finally, several aluminum wire bonds realize the electrical connection between the readout chips and a PCB, installed on a frame with a vacuum tight flange at one end, resulting in a compact integrated device easy to insert into the vacuum vessel [5].

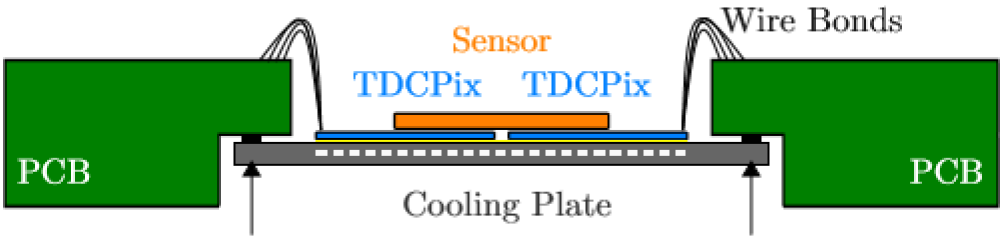

Figure 7 GTK assembly [7]

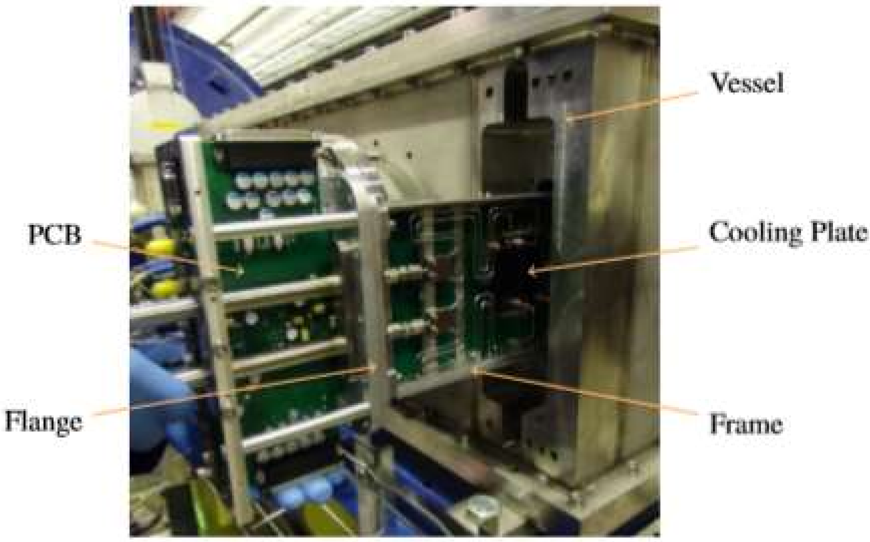

Figure 8 GTK frame installation [5]

As mentioned above, the GTK is an accurate measuring tool that requires peculiar technical specifications to guarantee the desired results. Among these, the thickness of the entire system is definitely the most relevant parameter to be taken into account because it directly affects the probability of interactions with the incoming beam. Inelastic scattering phenomena can in fact be reduced by thinning as much as possible all the components involved, but this inevitably leads to remarkable engineering challenges [5]. For this purpose, the NA62 collaboration has established a maximum thickness limit for each station equal to 0.5% X_0 in the sensitive area, corresponding to about 500 µm of silicon [7]. The constraint is chosen referring to this parameter because, in physics, X_0 is the characteristic radiation length of each material that is linked to the energy lost by a high-energy particle during its electromagnetic interaction with the material traversed. In this regard, the tailored sensor and chips have been implemented and matched to an innovative microchannel cooling plate being in depth studied in the next chapters. Thanks to microfabrication technologies, a cutting-edge cooling system has been created, capable of fulfilling the strict thickness constraint and supporting the electronics stacked on it at the same time. Moreover, the microchannel heat sink is designed to withstand a vacuum and high radiative environment and it is made of silicon to ensure mechanical stability in terms of thermal expansion.

The respective thicknesses of all the items are shown in table below.

Items	Thickness [μm]
Sensor	200
TDCpix	100
Epoxy glue layer	20
Cooling plate	210
Total silicon thickness in the active area	510

Table 2 Thickness of items

Figure 9 GTK station sensor side on the left and cooling plate side on the right [7]

1.3 Thesis outline

The dissertation is structured in six chapters. Chapter 2 explains all the theoretical concepts underlying the studies carried out in the following chapters and provides a literature overview concerning the state of the art of the technologies covered. Chapter 3 lists all the technical requirements of the cooling system, describing in detail the structure of the electronic device to be cooled and introducing future developments on this issue. This is followed by the presentation of the core activities carried out in the thesis shown in chapter 4 and 5. Chapter 4 initially deals with the design of the setup and the simulation of the thermofluidynamic behavior of the system, whereas, in the last part of the chapter, significant microchannel failure mechanisms are investigated by analyzing the results of experimental pressure tests. Thereafter, chapter 5 suggests a new cooling solution capable of satisfying the increasing demands of the experiment collaboration in terms of measurement accuracy. Finally, in the chapter 6 a discussion of the findings is performed and the next steps to be pursued for the definitive implementation of the new cooling system are set out.

2. State of the art

2.1 Heat transfer

A heat sink is a highly conductive metal heat exchanger able to regulate the temperatures of an electronic device by dissipating the heat generated through a fluid to avoid overheating. The heat transfer from the hotspot to the cooling medium, usually air, water or coolants occurs according to three different mechanisms:

- Thermal conduction;
- Thermal convection;
- Thermal radiation.

2.1.1 Thermal conduction

Thermal conduction is the heat transfer between particles having different energy interacting with each other [18]. Conduction occurs mainly in solids due to the transmission of vibrational energy between adjacent molecules or to the motion of electrons, but even in liquids and gases as a result of the random collisions between molecules [18]. The thermal power transmitted is closely related to the temperature difference between two points of the body, but it also depends on the thermal conductivity of the material and its geometry. [18]. In steady-state conditions, that is with temperature which does not vary over time, the conductive thermal power transmitted through a flat wall can be expressed through the Fourier law [18].

$$\dot{Q} = -\lambda \cdot A \cdot \frac{dT}{dx} \tag{2.1}$$

Where:

- $\dot{Q}$ is the conductive thermal power;
- λ is the thermal conductivity of the material;
- A is the wall area;
- $\frac{dT}{dx}$ is the temperature gradient.

The negative sign in the expression above means that the heat flow and temperature gradient always have opposite directions, hence the heat is always transferred from the body at higher temperature to that at lower temperature [18].

2.1.2 Thermal convection

Thermal convection is the heat transfer between a fluid, such as liquid or gas, and the solid wall that laps during its motion [18]. It involves both thermal diffusion and advection and it can be of two types [18]:

- Natural convection;
- Forced convection.

In natural convection the ascensional forces arising from differences in density linked to differences in temperature in the fluid generate the motion of the fluid itself, while in forced convection the motion is induced by the action of a fluid machine [18]. In electronics, both mechanisms are usually used by heat sinks to remove unwanted heat, but forced convection ensures higher cooling efficiency thanks to the promotion of the advective component. Thermal convection is a very complex phenomenon dependent on many physical and kinematic factors, but it can be expressed by a very simple formula known as Newton's law [18].

$$\dot{Q} = h \cdot A_w \cdot (T_w - T_\infty) \tag{2.2}$$

Where:

- $\dot{Q}$ is the thermal power;
- h is the convective heat transfer coefficient;
- A_w is the heat exchange surface;
- T_w is the wall temperature;
- T_∞ is the fluid temperature at a point distant from the wall.

The convective heat transfer coefficient is a complex parameter used to describe the phenomenon as a whole and which therefore depends on numerous factors such as dynamic viscosity of the fluid (μ), thermal conductivity of the fluid (λ), fluid density (ρ), specific heat transfer of the fluid (c_p), fluid velocity (v), geometry and roughness of the wall and fluid regime [18]. In Newton's formula, the temperature of the fluid refers to a point sufficiently distant from the surface because a thermal layer is created near the wall. Its origin is strongly related with the generation of a velocity boundary layer resulting from the adhesion of the first meatus to the wall which involves a zero fluid velocity at the interface [18]. Starting from the first fluid layer, an increasing velocity profile is generated throughout the entire thickness of the boundary layer until reaching the uniform velocity of the free stream. This effect is due to the viscous forces exchanged between the adjacent layers of fluid which create a slowing down of the flow near the wall [18].

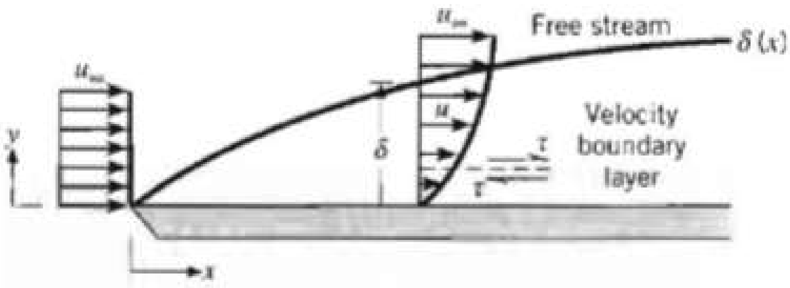

Figure 10 Velocity boundary layer [19]

Similarly, in the case of the motion of a fluid in contact with a wall having a different temperature, a temperature boundary layer is also created due to the thermal equilibrium that is established between the wall and the first layer of the fluid. Consequently, the heat exchange between the adjacent layers of fluid leads to the development of the temperature profile until the core temperature of the fluid is reached.

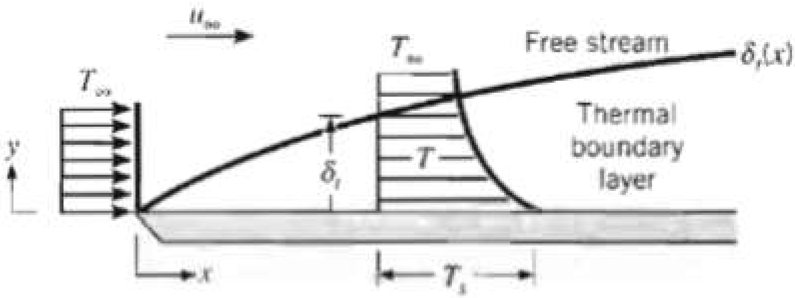

Figure 11 Thermal boundary layer [19]

In the study of the motion of a fluid within a channel, it is also essential to analyze the flow development at the entrance of the channel in order to understand how the velocity and temperature profiles change as the longitudinal coordinate varies. A fluid flow entering a channel at a uniform velocity needs to run a certain length to reach a fully developed flow, thus in the case of channels of modest size such as microchannels, this region can cover a considerable part of the entire path. For this reason, the following paragraph dealing with the description of the microchannels will illustrate how the thermofluidynamic variability in this region influences the heat transfer and therefore the value of important reference quantities.

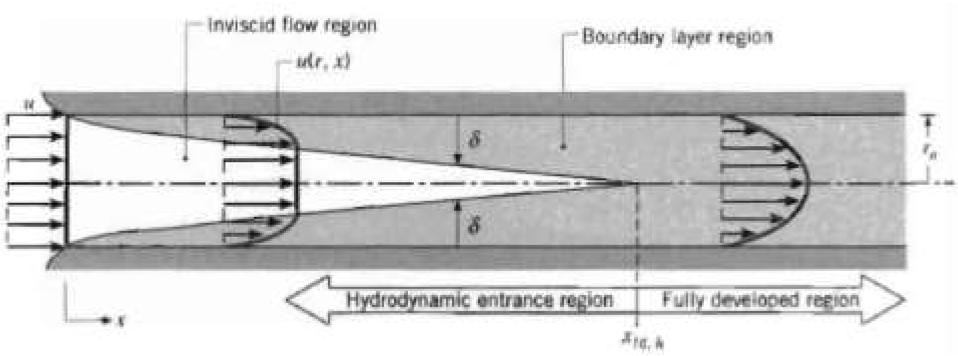

Figure 12 Flow development at the entrance [19]

As mentioned before, convection also depends on the regime of motion which can be laminar or turbulent. Laminar flow is characterized by regular and ordered motion typical of highly viscous mediums and very slow flow, while turbulent flow is irregular, random and chaotic such as the movements of low-viscosity fluids like air or the motions of liquids at high speed [18]. The features of a flow regime depend on numerous factors such as the physical and kinematic properties of the fluid, the geometry and the roughness of the duct, already considered in the convective heat exchange coefficient, therefore it is necessary to have a recognition procedure that takes into account all these aspects. To identify the fluid flow regime it is good practice to analyze the value of the Reynolds number. It is a dimensionless number which, by measuring the ratio between the inertia and viscous forces, foresees the generation of a laminar, turbulent or transition motion. It is expressed as [18]:

$$Re = \frac{(\rho \cdot v_\infty \cdot D)}{\mu} \tag{2.3}$$

Where:

- ρ is the fluid density;
- v_∞ is the fluid velocity far enough from the wall;
- D is the characteristic length of the problem;
- μ is the dynamic viscosity.

The flow is judged to be laminar for Re values lower than 2300 and starts to become turbulent for Re > 4000 [29]. In the middle the flow is instead assessed to be in the transition zone.

In addition to the Reynolds number, other dimensionless numbers are also used to describe thermal convection, such as the Nusselt and Prandtl numbers. Nusselt number expresses the ratio of convective to conductive heat transfer, providing an estimation of the prevailing mechanism and it is expressed with the following formula [18]:

$$Nu = \frac{h \cdot D}{\lambda} \tag{2.4}$$

Where:

- h is the convective heat transfer;
- D is the characteristic length of the problem;
- λ is the fluid thermal conductivity.

Nu is equal to one for mere conduction throughout the fluid [18].

On the other hand, Prandtl number is used to evaluate the velocity and thermal boundary layers and it is expressed by the ratio between the kinematic and thermal diffusivities [18].

$$Pr = \frac{\nu}{\alpha} = \frac{\mu \cdot c_p}{\lambda} \tag{2.5}$$

Where:

- ν is the kinematic diffusivity;
- α is the thermal diffusivity;
- μ is the dynamic viscosity;
- c_p is the fluid specific heat;
- λ is the fluid thermal conductivity.

The temperature boundary layer is larger than the velocity one for Pr << 1 and vice versa for Pr >> 1 [18].

2.1.3 Thermal radiation

Thermal radiation is the heat transfer through electromagnetic waves between two bodies at different temperatures and greater than absolute zero [18]. It is the only heat transfer mechanism that does not require a medium interposed between the two heat exchange sources, therefore it can also take place in a vacuum environment [18]. The maximum thermal power emitted by radiation can be calculated with the Stefan-Boltzmann law [18]:

$$\dot{Q}_{max} = \sigma \cdot A \cdot T^4 \tag{2.6}$$

Where:

- $\dot{Q}_{max}$ is the maximum thermal power emitted by the heat surface;
- σ is the Stefan-Boltzmann constant equal to $5.67 \cdot 10^{-8}$;
- A is the area of the heat surface;
- T is the temperature of the surface.

This relation is valid for a black body having by definition an emissivity coefficient equal to one, whereas the radiation emitted by a non-black body must be multiplied by a coefficient ε less than one [18]. The thermal power transmitted is equal to that emitted minus that absorbed by radiation and in the case of a radiant surface with emissivity ε surrounded by a black surface it is equivalent to [18]:

$$\dot{Q} = \varepsilon \cdot \sigma \cdot A \cdot (T^4 - T_b^4) \tag{2.7}$$

Where:

- $\dot{Q}$ is the net thermal power;
- ε is the surface emissivity;
- σ is the Stefan-Boltzmann constant;
- A is the area of the surface;
- T is the temperature of the surface;
- T_b is the temperature of the surrounding black surface.

Thermal radiation is a very complex physical phenomenon dependent on the properties of the radiating surfaces, their relative orientation and the characteristics of the interposed medium [18], but relevant importance is assigned to the temperature raised to the fourth power. Exclusively for thermal radiation, the absolute temperature values themselves actually plays a fundamental role in the heat exchange beside the temperature difference.

2.2 CFD governing equations

Many standard thermofluidynamic problems can be solved with analytical calculations, but in most cases, it is not possible to introduce some simplifying hypotheses as it is necessary to consider numerous variables and phenomena. In this case, numerical methods are used to obtain an approximate solution by solving the set of Navier-Stokes-Fourier equations.

Continuity equation [20]:

$$\frac{\partial u}{\partial x} + \frac{\partial v}{\partial y} + \frac{\partial w}{\partial z} = 0 \tag{2.8}$$

Momentum conservation [20]:

$$\rho \left(u\frac{\partial u}{\partial x} + v\frac{\partial u}{\partial y} + w\frac{\partial u}{\partial z} \right) = -\frac{\partial p}{\partial x} + \mu \left(\frac{\partial^2 u}{\partial x^2} + \frac{\partial^2 u}{\partial y^2} + \frac{\partial^2 u}{\partial z^2} \right) \tag{2.9}$$

$$\rho \left(u\frac{\partial v}{\partial x} + v\frac{\partial v}{\partial y} + w\frac{\partial v}{\partial z} \right) = -\frac{\partial p}{\partial y} + \mu \left(\frac{\partial^2 v}{\partial x^2} + \frac{\partial^2 v}{\partial y^2} + \frac{\partial^2 v}{\partial z^2} \right) \tag{2.10}$$

$$\rho \left(u\frac{\partial w}{\partial x} + v\frac{\partial w}{\partial y} + w\frac{\partial w}{\partial z} \right) = -\frac{\partial p}{\partial z} + \mu \left(\frac{\partial^2 w}{\partial x^2} + \frac{\partial^2 w}{\partial y^2} + \frac{\partial^2 w}{\partial z^2} \right) \tag{2.11}$$

Energy conservation [20]:

$$\left(u\frac{\partial T}{\partial x}+v\frac{\partial T}{\partial y}+w\frac{\partial T}{\partial z}\right)=\frac{1}{\alpha}\left(\frac{\partial^2 T}{\partial x^2}+\frac{\partial^2 T}{\partial y^2}+\frac{\partial^2 T}{\partial z^2}\right) \tag{2.12}$$

2.3 Microchannels

Microchannels were first introduced to heat sinks by Tuckerman and Peace in 1981 [11]. In their publication entitled "High Performance Heat Sinking for VLSI" they assessed the cooling performance of microchannels by opening the doors to a new frontier for cooling electronic devices. They actually managed to build a microchannel heat sink that could dissipate up to 790 W/cm² [12], by keeping a temperature difference between water and solid wall equal to 71°C and their excellent result gave reason for future study concerning this technology. Several microchannel cross-sections of different shapes have been studied, but greater interest has been dedicated to rectangular channels, thanks to their easy production process and their good and reliable performance. Microchannels are characterized by very high exchange surfaces and they are always built with highly conductive material to remove large quantities of heat from very small heating sources without exceeding the overall dimensions. On the other hand, the micrometric scale requires a more in-depth design than traditional channels because, in this case, many usually negligible effects take on significant importance and influence the prediction of heat transfer. It is therefore essential to know the boundary conditions to be used and correctly evaluate which phenomena to neglect or not according to the geometric and flow parameters of the system. These phenomena in the literature are called scaling effects and some of them are listed below [13]:

- Entrance effects;
- Temperature dependence;
- Rarefaction effects;
- Axial thermal conduction;
- Viscous heating;

ENTRANCE EFFECTS

Entrance effects are due to the development of the fluid at the inlet and they alter the prediction of wall temperatures in the standard case study representing a channel to which a constant heat flux boundary condition is applied. In literature it is reported that, under fully developed motion conditions, the bulk temperature of the fluid and the temperature of the adjacent wall increase at the same rate by keeping the same temperature difference along the longitudinal axis of the channel. It is instead visible from the figure below that near the entrance the temperature difference tends to decrease approaching the fluid temperature.

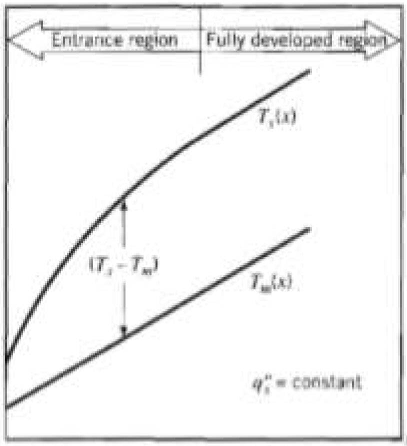

Figure 13 Constant wall heat flux boundary condition [19]

This can also be noticed by analyzing the Nusselt number, an invariable parameter under fully developed motion conditions, that near the inlet has higher values which then tend asymptotically to the value foreseen in the literature for the geometry examined along the longitudinal coordinate. As Nusselt number varies, heat transfer modes also change accordingly in the affected area, so it is very important to take this effect into account for very short channels. It is good practice to check its influence by looking at the Graetz number which must be less than 10 in order to neglect this phenomenon [13]:

$$Gz = \frac{Re \cdot Pr \cdot D_h}{l} \tag{2.13}$$

Where:

- Gz is the Graetz number;
- Pr is the Prandtl number;
- l is the channel length.

Alternatively, it is possible to know the minimum length of the channel to neglect the entrance effects by consulting the diagram below.

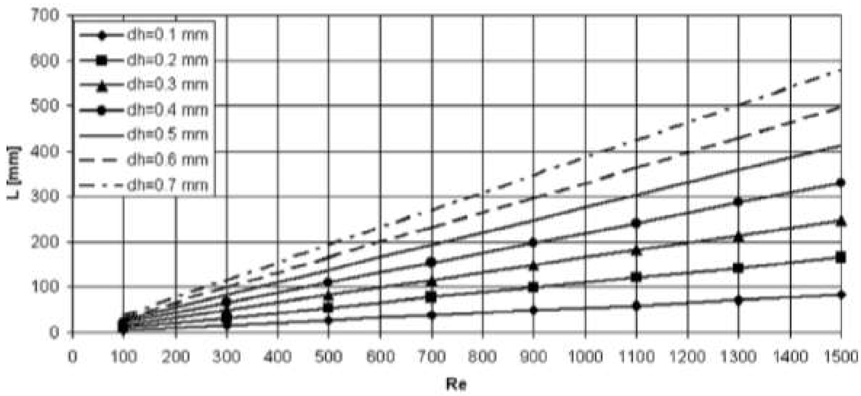

Figure 14 Minimum microchannel length to neglect entrance effects for water at 20°C [13]

TEMPERATURE DEPENDANCE

In microchannels there are usually high differences in fluid temperature between inlet and outlet which can cause variations in the physical properties of the fluid itself [13]. These variations must be estimated and considered during the design, but in this thesis work they will be neglected because the temperature gradients in the fluid will be small.

RAREFACTION EFFECTS

These effects will not be analyzed because liquid coolant flows inside the microchannels of the GTK heat sink.

AXIAL THERMAL CONDUCTION

In microchannels, under certain geometric and flow conditions, it is possible to encounter the conjugate heat transfer phenomenon, almost always negligible in traditional ducts. The conjugative heat transfer occurs for example when a metal plate is wetted on one side by an isothermal hot fluid at rest and on the other is lapped by a moving cold fluid. In this system, convection will be more effective in the fluid inlet area because it heats up during its path reducing its temperature difference with respect to the solid wall. This creates a temperature gradient inside the plate itself from which a conductive flow flows along the longitudinal coordinate of the plate. This heat flow component parallel to the plate reduces the perpendicular heat flow component directed towards the fluid responsible for heat dissipation, resulting in a lowering of the cooling efficiency. The same can happen in a duct if the solid walls are of a thickness comparable to the section of the channel crossed by the fluid. In traditional channels, the fluid section is actually always bigger than the area of the metal pipe that surrounds it, therefore the convection is very privileged compared to the axial conduction. In microchannels the quantity of highly conductive material can be of the same order of magnitude as the fluid one, therefore in conditions of very slow and viscous flow (Re <100) this phenomenon can occur influencing the performance of the microchannel [13]. The axial conduction intensity increases as the hydraulic diameter of the channel decreases and in the case analyzed with rather low Re numbers it is useful to make a check for further investigation [14]. Marazana proposes to neglect the conjugate heat transfer if the homonymous number is less than 0.01 [13].

$$M = \frac{k_w}{k_f} \cdot \frac{A_w}{A_f} \cdot \frac{1}{Re \cdot Pr} \tag{2.14}$$

Where:

- M is the Marazana number;
- k_w is the thermal conductivity of the solid wall;
- k_f is the thermal conductivity of the fluid;
- A_w is the cross-section area of the channel solid walls;
- A_f is the fluid cross-section area;
- Re is the Reynolds number;
- Pr is the Prandtl number.

In the cases subsequently studied, the Marazana number is considerably lower than the recommended limit, therefore this scaling effect can be neglected.

VISCOUS HEATING

Viscous heating is relevant when the circulating fluid has a high dynamic viscosity and the flow has a high Reynolds number. In the GTK cooling system this phenomenon is neglected because Reynold number is less than 1000 [13]. For further verification, viscous heating has been included in the simulation calculations but there has been an increase in fluid temperatures of only 0.1 °C.

After a brief description of the scaling effects that can be encountered, the fluid dynamic study and the calculation of the pressure drops inside the microchannels follows. The flow inside the microchannels is in most cases laminar due to their micrometric section and the fluid velocities controlled in such a way as to limit pumping work. The laminar motion regime does not allow for efficient heat exchange as the turbulent motion but thanks to the high area to volume ratio, the microchannels manage to achieve very high cooling performance. Furthermore, the establishment of a laminar flow simplify the discussion of the problem and the fluid dynamic calculations, providing the opportunity to analytically validate simulations for feedback.

The pressure drops generated in the heat sink can be roughly calculated by using the Poiseuille's law for distributed losses and with the formula for concentrated pressure drops common in the literature.

Poiseuille law for laminar flow [30]:

$$\Delta p = f \cdot \rho \cdot \frac{l}{D_h} \cdot \frac{{v_m}^2}{2} \tag{2.15}$$

Where:

- Δp is the pressure drop;
- v_m is the average fluid velocity;
- f is the Darcy factor for various duct cross-section shapes;
- ρ is the fluid density;
- l is the length of the channel;
- D_h is the hydraulic diameter calculated as:

$$D_h = \frac{4 \cdot A}{P} \tag{2.16}$$

Where:

- A is the channel cross-section area;
- P is the perimeter wet by the fluid.

Formula for concentrated losses [30]:

$$\Delta p = \beta \cdot \rho \cdot \frac{{v_m}^2}{2} \tag{2.17}$$

Where β depends on the piping geometry.

With regard to thermodynamic calculations, it is important to underline that since the temperature of the fluid varies within the section of the microchannel, it is necessary to take the bulk temperature as a reference because it is averaged with respect to the mass flow rate.

Bulk temperature expression for incompressible fluid:

$$T_b = \frac{\int T \cdot v \cdot dA}{\int v \cdot dA} \tag{2.18}$$

To perform a thermodynamic computation, it is always necessary to identify and specify the boundary conditions imposed on the exchange surfaces of the channel, which lead to different temperature profiles. The most common thermodynamic boundary conditions applied in the study of microchannels are shown below [12]:

- T: axially and circumferentially uniform wall temperature;
- H1: circumferentially constant wall temperature and axially constant wall heat flux;
- H2: axially and circumferentially uniform wall heat flux.

In the first case, a temperature profile of the fluid tending asymptotically to the wall temperature is expected.

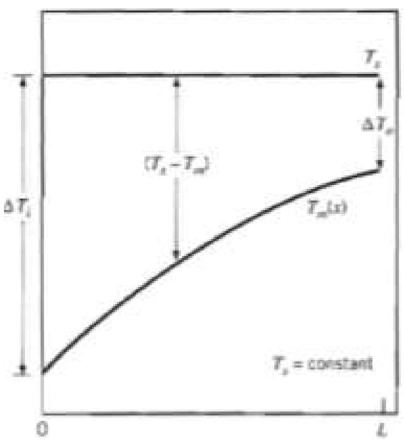

Figure 15 T1 boundary condition: fluid temperature profile [19]

The H1 boundary condition instead, is suitable for channels surrounded by highly conductive material and subjected to a constant thermal flow, as in the GTK cooling system. Finally, the third boundary condition has recently undergone numerous studies as less reliable information concerning heat transfer mechanism has been collected so far.

The heat is mainly dissipated by convection and conduction in microchannels, while the intensity of thermal radiation depends very much on the layout and geometry of the entire cooling system. For example, in the GTK cooling system thermal radiation is negligible compared to the heat exchanged through convection because of the small radiant surfaces, the low absolute values of the temperatures and the small differences in temperatures found within the entire working volume [8].

2.4 Microchannel manufacturing

Microchannel production mainly consists of two steps: etching and bonding. During the etching phase, microchannels are created on a silicon wafer according to the desired shape and size through microfabrication techniques. The most common silicon etching technologies for microchannels are [15]:

- Wet anisotropic etching;
- Wet isotropic etching;
- Dry anisotropic etching;
- Dry isotropic etching.

Basically, wet techniques use KOH based chemical solutions for anisotropic etching and acid solutions for isotropic etching, while dry techniques are performed through plasma etching [15]. For the GTK cooling plate production, a dry anisotropic technique called "Deep reactive-ion etching (DRIE)" is employed, although in paragraph 4.2.2 results from laser etching will be shown. DRIE is a dry plasma etching capable of creating channels with aspect ratios up to 30 [16]. It generates almost vertical walls through an iterative process composed of two essential phases that follow one another repeatedly. The process consists of an initial phase of $\mathrm{SF_6}$ plasma etching followed by the deposition of a polymeric passivating layer capable of protecting the side walls from attack [16]. The $\mathrm{C_4F_8}$ polymer covers the entire cavity obtained in the etching phase, but it is mainly eroded at the bottom because of the anisotropy of the attack, promoting the progressive increase in depth of the channel [16].

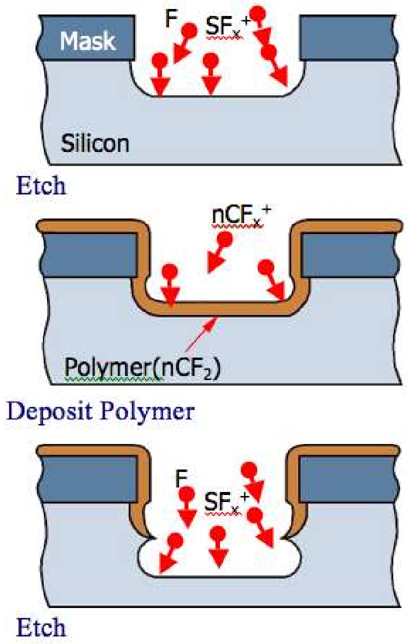

Figure 16 DRIE etching process [16]

This technique known as Bosch process requires many steps to create channels with depths of the order of hundreds or thousands of microns and can reach removal rates ranging from 1 to 4 microns per minute [16]. The geometry of the channel is indicated by the shape of a photoresist mask that protects the surfaces not to be treated and the operating time does not depend on the volume removed but only on the depth reached.

After the creation of the channels it is necessary to cover them with a second wafer at the top, thus shifting to the bonding phase. There are three different types of wafer bonding [16]:

- Direct or fusion bonding;
- Anodic bonding;
- Intermediate layer bonding.

All three techniques require high flatness, smoothness and meticulous cleaning of the mating surfaces in order to achieve a strong and reliable bonding. Inadequate preparation of the surfaces can in fact generate gaps between the two wafers in which high pressure values of the enclosed fluid can be reached, resulting in the detachment of the bodies [16].

Direct bonding is similar to a welding operating on a microscopic scale and is used to join silicon wafers as in the GTK cooling and produce SOI wafers [17]. It exploits intermolecular forces and does not require an intermediate layer as an interface between the two surfaces to be coupled [17]. Before fusion bonding wafer preprocessing and preventive alignment are needed. Subsequently the bonding phase is carried out in two separate steps because a prebonding at room temperature is carried out first and then a high temperature annealing follows to achieve greater tightening [17].

Anodic bonding has a simpler procedure than the previous case and is often used for MEMS packaging and for the GTK cooling plate prototypes specifically. It joins a silicon wafer with an another of Pyrex 7740 through an electric field and high temperature, establishing a bonding characterized by low residual stresses since the two materials have similar thermal expansion coefficients [16].

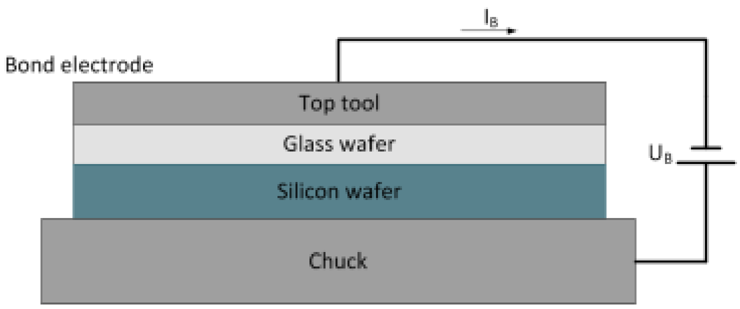

Figure 17 Anodic bonding process [17]

By applying a positive voltage to the silicon wafer and placing the system in a high temperature chamber, a considerable migration of the Na^{+} ions from the Pyrex towards the interface of the two wafers is generated [16]. This mechanism negatively charges the Pyrex wafer thus allowing the fusion between the two materials [16].

3. Research questions: GTK cooling system requirements and development

Cooling is one of the most critical aspects in the design of the HEP silicon tracking detectors. It is in fact essential to ensure reliable performance and a longer lifetime of the electronics which is strongly influenced by thermal effects. The electronic components are usually cooled by natural or forced convection generated by ordinary air vents that remove the heat, preventing them from reaching temperatures that could affect their operation. Unfortunately, this simple solution is not suitable for cooling HEP detectors because they often must face with stringent requirements that inevitably ask for greater design efforts.

HEP detectors are often located in a harsh vacuum and high radiative environment that inhibits cooling by forced air convection and that requires a radiation hard coolant. As mentioned in the previous paragraphs, low mass cooling systems are required to avoid multiple scattering, but this weakens the structure and makes it more subject to thermal runaway since less heat can be diffused through thermal conduction. Moreover, non-magnetic material must be used to prevent possible displacements in the assembly due to the strong magnetic field in which the detector is set. Last but not least, the integration process of the cooling in the structure must not cause any issues or difficulties during maintenance operations.

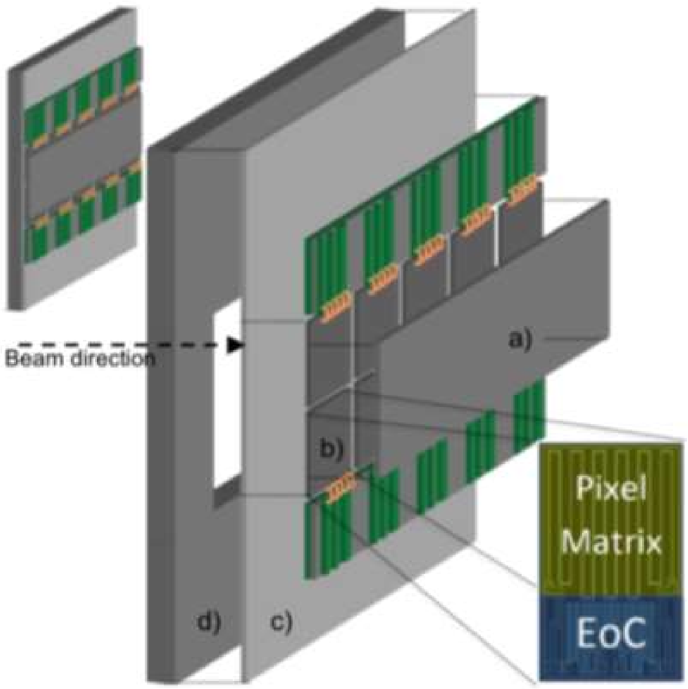

Figure 18 a) Sensor, b) TDCpix ASIC, c) Cooling Plate, d) Support and alignment structure [8]

Beside all these requirements, the GTK cooling system must also act as a mechanical connection with the PCB and as a support for the heat source itself represented by the ASIC chips. The purpose of the ASIC chips is to read out the signals coming from the sensor, but in doing so they dissipate a certain amount of heat. Each TDCpix is arranged into two parts: a pixel matrix that digitalizes the signals produced by the sensor and the End of Column (EoC) area where the signals are mainly processed keeping track of time intervals [5]. The pixel matrix is entirely covered by the 60.8 x 27 mm² sensor surface and it generates a heat flux density of about 0.4 W/cm². On the other hand, the EoC area takes place outside the field crossed by the beam and it dissipates about 4.8 W/cm².

The main dimensions of the entire electronic system to be cooled is shown in figure 19.

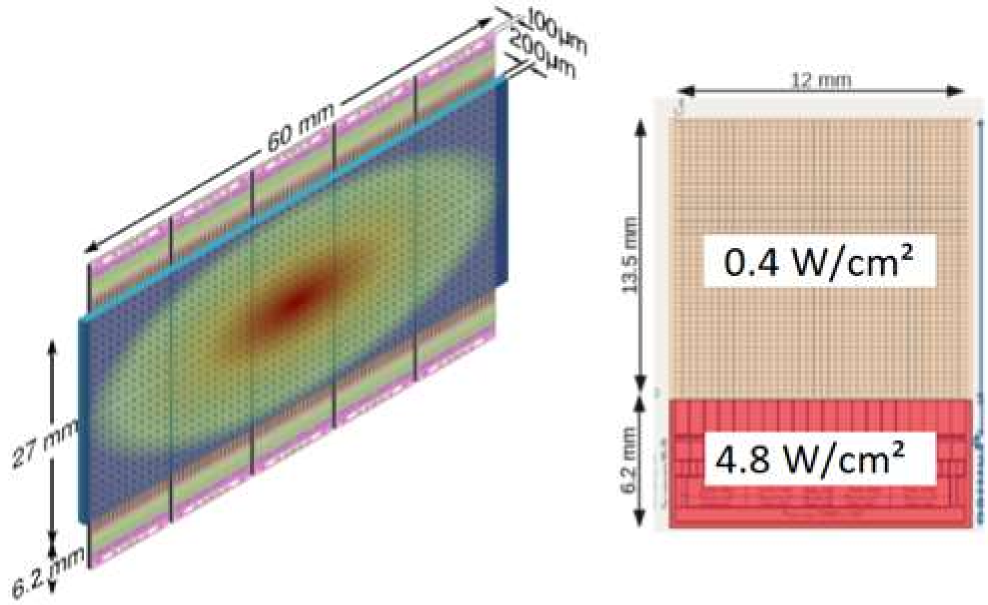

Figure 19 Electronics main dimensions [8]

The GTK cooling device is therefore required to manage a total of about 45 W of thermal power fulfilling the following specifications:

- The maximum sensor operating temperature should be less than 5°C in order to achieve a transducer lifetime of up to 100 working days;
- The temperature difference in the sensor must not exceed 10°C so that measuring performance is not significantly affected;
- A strongly limited material budget is provided in the sensitive area to respect the 0.5% X_0 radiation length limit, established to prevent the deflection of the incoming particles trajectories;
- No material budget constraints outside the active area;
- The overall system operates in a vacuum environment.

In the next chapter the cooling solution currently deployed in the experiment will be introduced and it will be discussed how this engineering challenge has been overcome.

Nevertheless, NA62 collaboration has been exploring the possibility of updating the current cooling configuration in order to further reduce the amount of material crossed by particles in the sensitive area.

On this issue, a new cooling layout without material in the active area is proposed and investigated in chapter 5, opening up prospects for improvement in terms of measurement accuracy.

4. GTK heat sink: Cooling Plate

This chapter shows the successful implementation of the innovative cooling system conceived by the CERN PH department, describing the setup currently in operation and the reasons that led to this solution. To respond to these unique engineering requirements, a microchannel heat sink was designed taking advantage of today's MEMS microfabrication technologies. The GTK cooling represents the pioneering application of microchannels in HEP cooling and, above all, it demonstrates their remarkable suitability to this field of research [5].

4.1 Setup

The GTK heat exchanger is a very thin cooling plate located right below the heat source, able to meet all the project requirements by using the microchannel technology. Thanks to the remarkable heat exchange surface achievable through microchannels, it is possible to create an extremely compact product that removes large amounts of heat at the same time. As mentioned above, the heat exchanger is placed in direct contact with the readout chips to achieve greater cooling efficiency and it is made of silicon which is a material characterized by an excellent thermal conductivity coefficient.

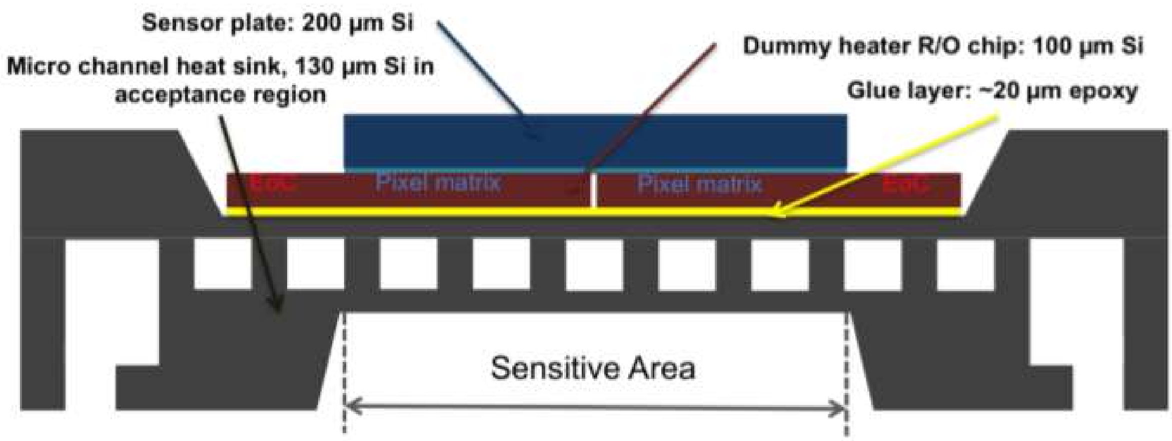

Figure 20 Cooling plate integration [8]

The plate is made of silicon also to better integrate the component with the electronic system and limit thermal expansion mismatches by keeping the CTE approximately constant throughout the assembly. The cooling device is composed of 150 microchannels that are etched into a silicon wafer and sealed at the top by a second wafer. Microchannels have got a rectangular cross-section and are placed under the whole heat source area, thus even acting as a support for the electronics above. The number of channels depends on their width and pitch, set equal to twice the width to maintain a perfect alternation between full and empty spaces and therefore to ensure a reliable bonding between the two wafers. Their length is influenced by the size of the area to be cooled, while the depth is imposed by the strict material budget. On the other hand, the cross-section dimensions are enforced by the criterion according to which is recommended not to exceed an aspect ratio equal to 3 [8]. This assumption is proven with CFD calculations by looking at the mass flow rate behavior as the width of the channel varies, keeping the pressure difference and the depth of the channel constant. The graph below actually shows that consistent increase in flow rate is no longer achieved over an aspect ratio of 3.

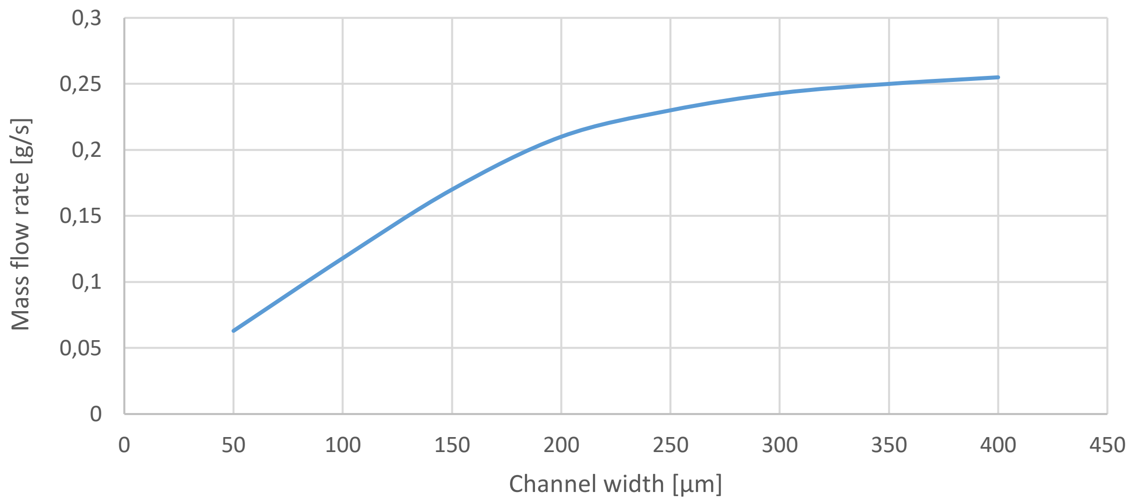

Chart 1 Mass flow rate for different aspect ratios

The main microchannel dimensions are shown in the following table.

Microchannel dimensions	[mm]
Length	42
Width	0.20
Depth	0.07
Pitch	0.40
Aspect Ratio	2.86

Table 3 Microchannel dimensions

Microchannels are arranged in parallel and splitted into two groups of 75 each in order to create two identical hydraulic circuits and thus reduce the load losses at the same mass flow rate. Each set of microchannels is served by two 1.60 mm x 0.28 mm manifolds integrated in the silicon plate whose purpose is to distribute and collect the fluid inside the heat exchanger.

The inlet and outlet are placed in a diametrically opposite position to obtain equally long fluid pathways in the circuit. This layout allows to have the same flow rate of coolant in all the channels and therefore to uniform the cooling performance along the whole surface of the plate. A picture representing the realistic product and a CAD drafting of the described assembly are shown in figure 21.

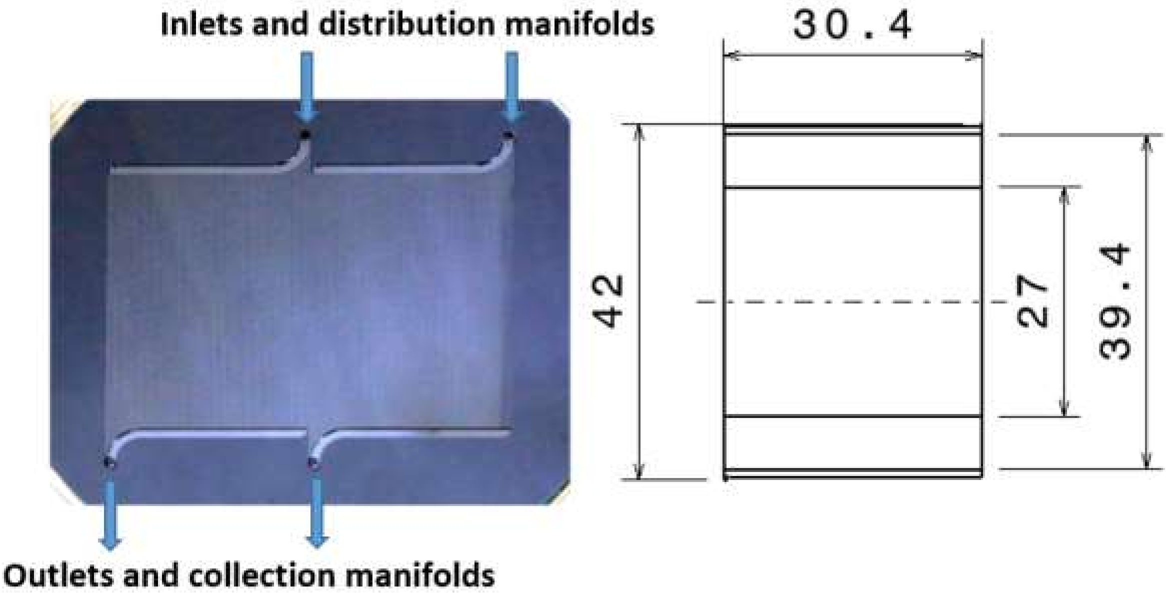

Figure 21 Two independent networks of microchannels on the left [8]. Single network main dimensions on the right

The 60.8 x 42 mm² cooling plate is then connected to the pipe system by four custom molded connectors which will be described in paragraph 4.2.3. The pipe system is composed of two 1/8'' capillaries that manage the flow rate of the fluid entering and leaving the GTK assembly. To feed the two input connectors, the input 1/8'' pipe branches into two further 1/16'' capillaries through an intermediate manifold, and the same occurs at the outlet to collect the fluid coming from the two output connectors. It is important to underline that the distribution of the flow in two parallel hydraulic circuits also facilitates the integration of the capillaries in the connectors and their bending thanks to their smaller diameter. Finally, a set of insulated pipes convey the coolant from the GTK module to the cooling plant.

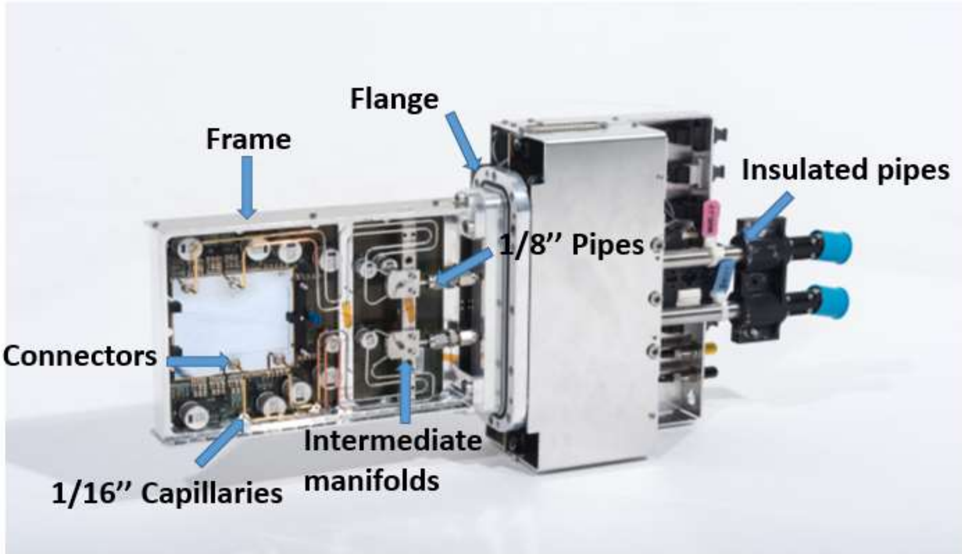

Figure 22 GTK cooling system [7]

The fluid leaves the plant at a temperature of -25°C but the inlet temperature in the GTK module turns out to be equal to -15°C because of the heat losses along the pipes. Nevertheless, the cooling plate manages to keep the sensor temperature below 5°C, recording a fluid outlet temperature of about 0°C.

Figure 23 GTK cooling plant

4.2 Cooling Plate manufacturing

The Cooling Plate production involves many manufacturing technologies belonging to the electronics industry, and in particular to the production of MEMS devices. Microfabrication techniques are therefore essential to build the designed microfluidic devices. The heat sink production must then be followed by other processes and assembly operations that allow its installation on the carrier board and consequently its placement in the area devoted to the GTK within the general structure of the experiment.

4.2.1 DRIE etching microchannel production process

The micro-channel pattern of the GTK cooling system is realized by performing several production steps briefly summarized below.

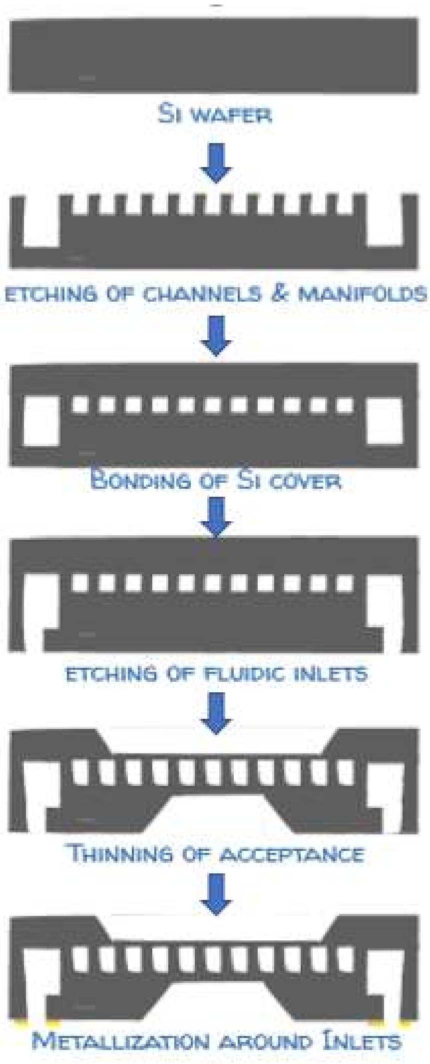

Figure 24 Cooling Plate manufacturing process [21]

The process starts from a thin silicon wafer on which the microchannel pattern and the manifolds are engraved by means of the DRIE etching technique. The shape of the pattern depends on the geometry of the photoresist mask created through photolithography whereas the working time depends on the groove depth. Once the grooves have been created, they are sealed by joining a second wafer on the top, creating a direct bonding between the two silicon wafers. However, for a successful direct bonding, an accurate mechanical polishing is needed in order to obtain a mirror surface [21]. For this purpose, CMP is used to level the roughness and to clean the surface, removing impurities. After the bonding, the product results to be a sort of monolithic element characterized by excellent mechanical strength and extremely compact dimensions. The next step involves the realization of the fluidic inlets where the connectors are accommodated and right after the thickness of the plate is reduced in the active area, again by DRIE etching. During this last step, some processing problems occur and some corrective actions are necessary to achieve the desired result. The difficulties encountered are due to the accumulation of SF_6 at the edges of the engraved surface where accelerated etching has been observed [21]. This however does not allow to obtain the desired flatness of the surface that is achieved by developing a more complex cooling plate production process.

Figure 25 Production issues. Desidered result on the left, accelerated etching on the right [21]

Process re-engineering demands the use of two pairs of SOI wafers, bonded to form an intermediate layer of insulating silicon oxide, useful for effectively delimiting the depth of the etching [5]. First of all, a reduction of the thickness of both the wafer stacks is performed in order to obtain the desired plate thickness in the next thinning step of the assembly [5]. The channels are then engraved on the first stack whereas on the second one an additional oxide layer is added [5]. Only at this stage the two wafers are coupled to seal the channels acts and, afterwards the thinning phase on both sides is regulated by the thickness of the two stacks [5].

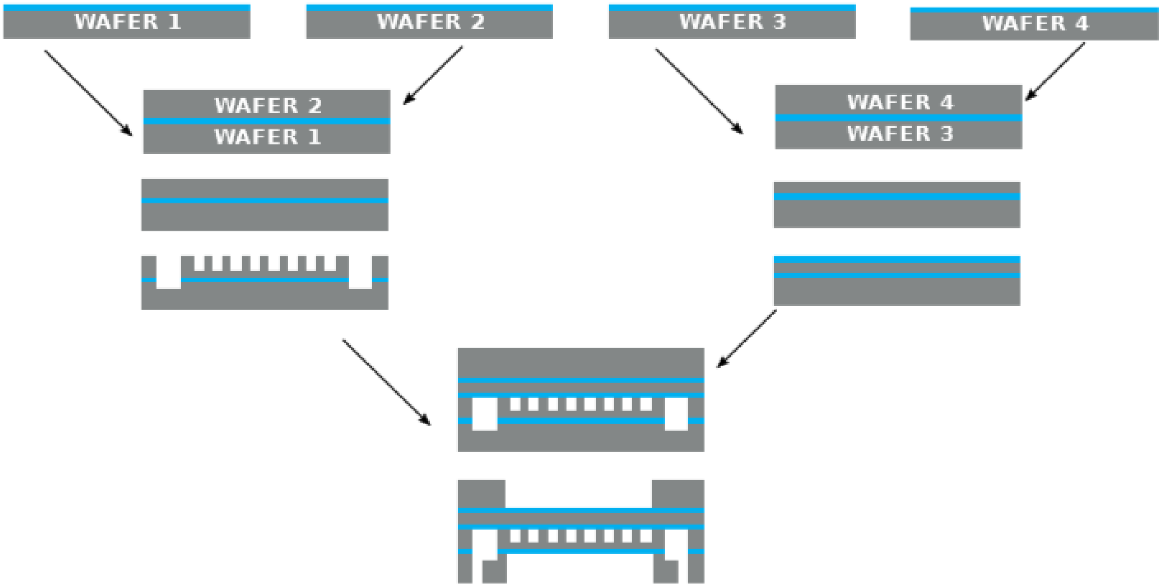

Figure 26 Cooling Plate production with SOI wafers [5]

In this way it is possible to build plates with a thickness of 280 micrometers without flatness problems, with satisfactory detail quality and with good repeatability. In detail, two complete patterns for cooling plates and several samples for testing are obtained from each processed silicon wafer. Once the etching has been carried out, the wafer is diced to divide and extract the individual components created.

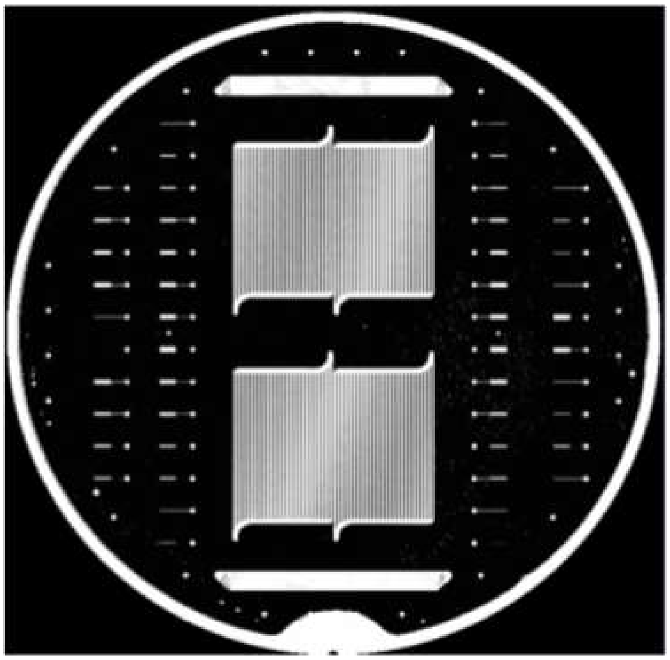

Figure 27 Wafer pattern [5]

4.2.2 Laser etching microchannel production

An alternative method for etching microchannels has also been evaluated, which uses laser etching to speed up production times and reduce costs. This technique is interesting because in the case of modest volume of material to be removed, it is possible to considerably reduce the duration of the etching phase, but it is first necessary to carry out a feasibility study to judge the quality of the machining process.

In this regard, studies and quality tests were carried out by a collaboration between the University of Marseille and the CERN PH department.

So far, two wafers with a surface layer of silicon oxide 1000 nanometers thick have been laser processed at University of Marseille and analyzed in the cleanroom at the CMi (University of Lausanne) with successful results.

Figure 28 Laser etched wafers

Here, the first steps have been taken towards the creation of the first prototypes with Pyrex microchannel coverage conducted by anodic bonding.

To judge the feasibility and quality of the process, the study analyzes both the geometry of the channels and the presence of surface impurities by using specific microfabrication equipment available at CMi.

The examination starts with the preparation of the samples, that requires a careful cleaning of the surfaces divided in the following steps:

1. Rinsing in the pool 1 containing distilled water.
2. Rinsing in the pool 2 containing distilled water.
3. Centrifugal drying.

Figure 29 Cleanroom cleaning equipment

After the cleaning step, the microchannel cross-section is observed by means of a Bruker mechanical profilometer to evaluate its geometric and dimensional accuracy. The profile of the section results rather consistent with the expectations in terms of size, instead some deviations are noted in terms of geometric shape suitability. The main discrepancies from the ideal geometry are the imperfect verticality of the side walls, the arched profile of the lower base and the hump visible on the surface probably due to the high temperatures reached in the silicon during etching.

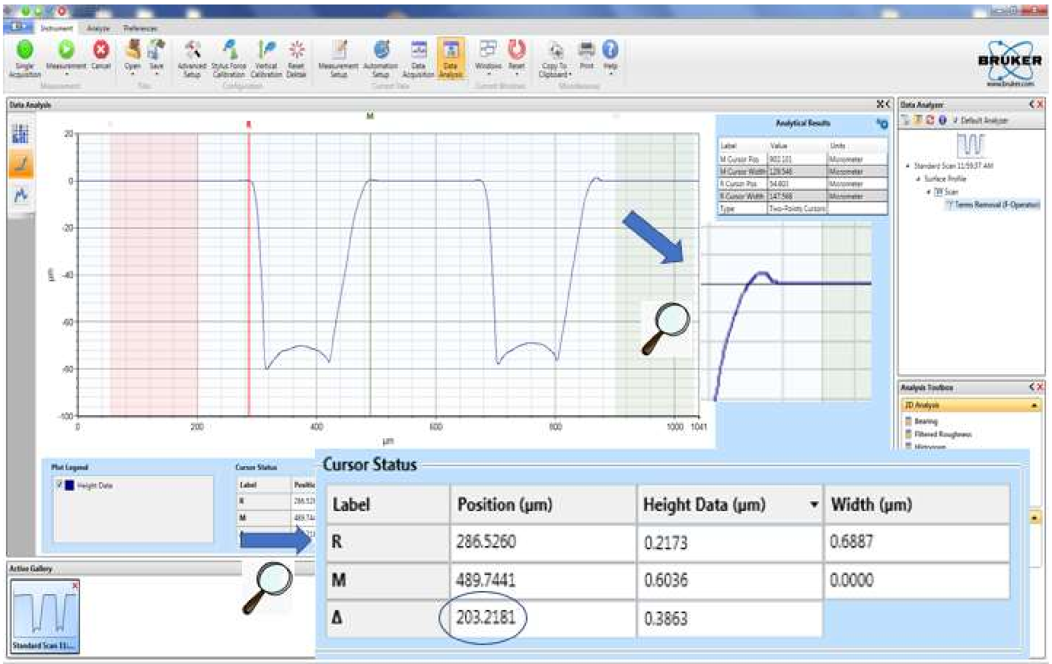

Figure 30 Mechanical profilometer output

The figure above illustrates the profile of two microchannels of the pattern, while the table below shows some dimensional values for some of the analyzed channels.

Microchannel dimensions	[µm]
Width	203.22
Depth	70.03
Max Depth	79.92
Height of the hump	2.57

Table 4 Laser etched microchannel dimensions

The visual analysis at the light microscope reveals some macroscopic impurities on the surface probably due to silicon spatter that occurs during the etching. Furthermore, the marks left by the processing along the perimeter of the incisions are clearly visible, since the laser etching causes thermal alterations in the material regions affected.

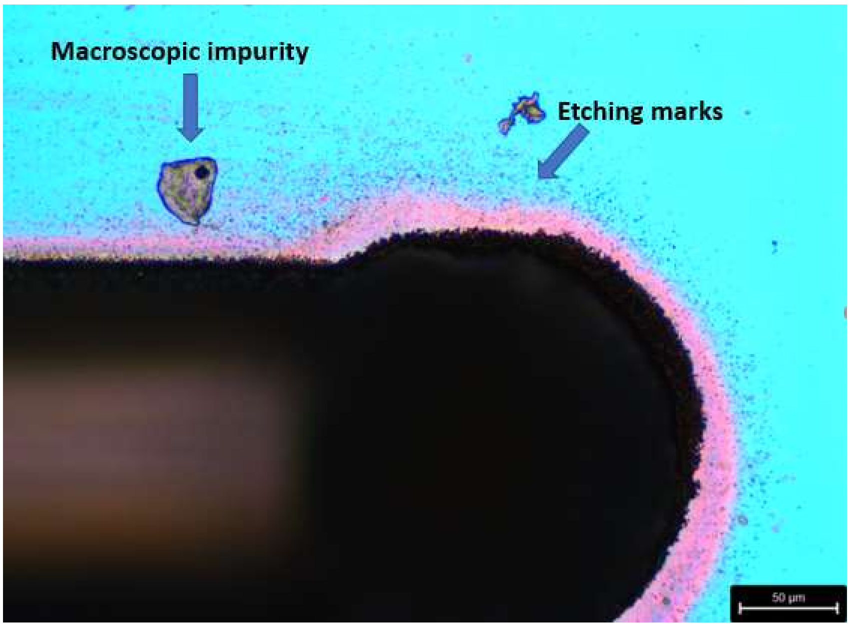

Figure 31 Impurities near the channel before removing the oxide

To inspect the surface even more in detail, the protective silicon oxide layer is removed by immersing the wafer in a BHF-based acid bath. The acid bath is followed by the previously explained cleaning procedure, after which the sample is again examined under the optical microscope and the mechanical profilometer. After the bath, the mechanical profilometer shows that the humps of material along the perimeter of the canal have been eroded, whereas some impurities can still be found under the optical microscope. The impurities turn out to be quite resistant to manual abrasion performed with a simple pad soaked in propanol, so further investigations are needed.

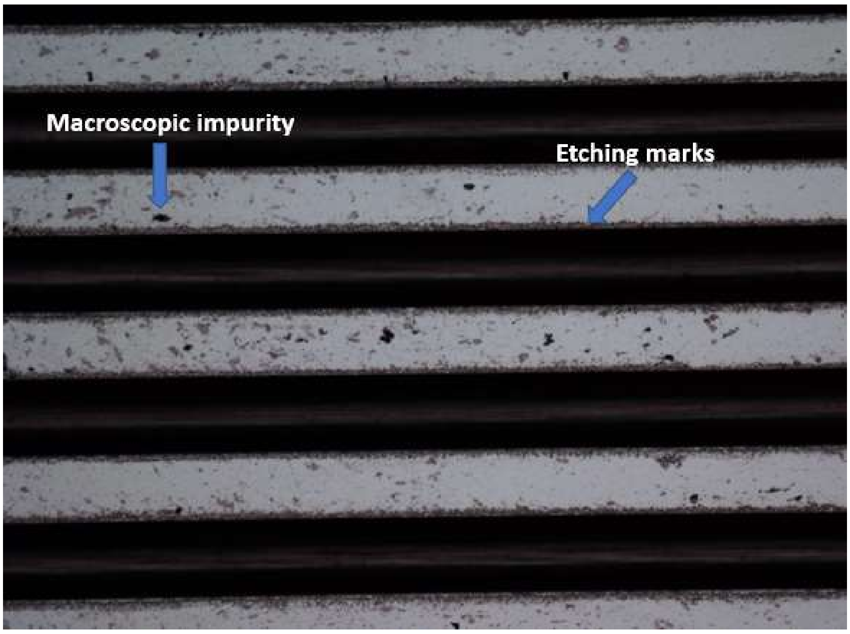

Figure 32 Macroscopic impurity and etching marks after removing oxide

Unfortunately, it is not possible to establish from the optical microscope images if these impurities are bumps or cavities, so investigations have also been made under an electronic microscope. Before the electron microscope analysis the sample is immersed in a Piranha solution (96% $\mathrm{H_2S0_4}$+ 200ml $\mathrm{H_20_2}$) bath to remove any organic substance lying on the wafer. The SEM Zeiss Merlin microscope images show that the impurities are in relief with respect to the free surface of silicon, so it is necessary to abrade them in order to have no adhesion problems during the next bonding phase.

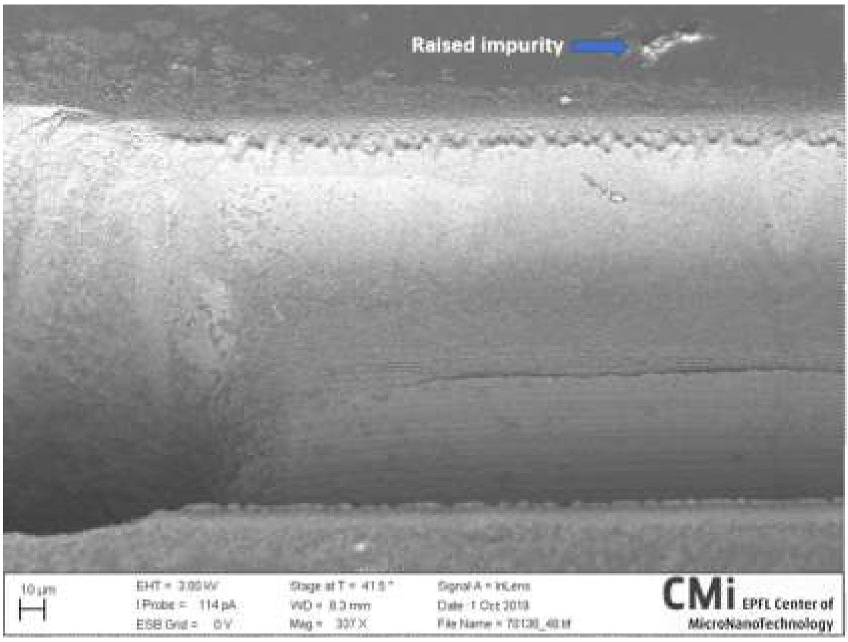

Figure 33 Impurities near the channel after removing the oxide (Raised silicon hump)

To remove impurities and flaws in processing, the wafer is subjected to CMP polishing, which make the surface smooth and suitable for bonding. The CMP is a wet abrasive polishing which combines the action of a rotating and extremely flat pad with the translation and the pressure imposed by a carrier that keeps the wafer in a horizontal position through the vacuum. This mechanism associated with the simultaneous dispersion of slurry on the pad allows obtaining the desired smoothness.

Figure 34 CMP at CMi

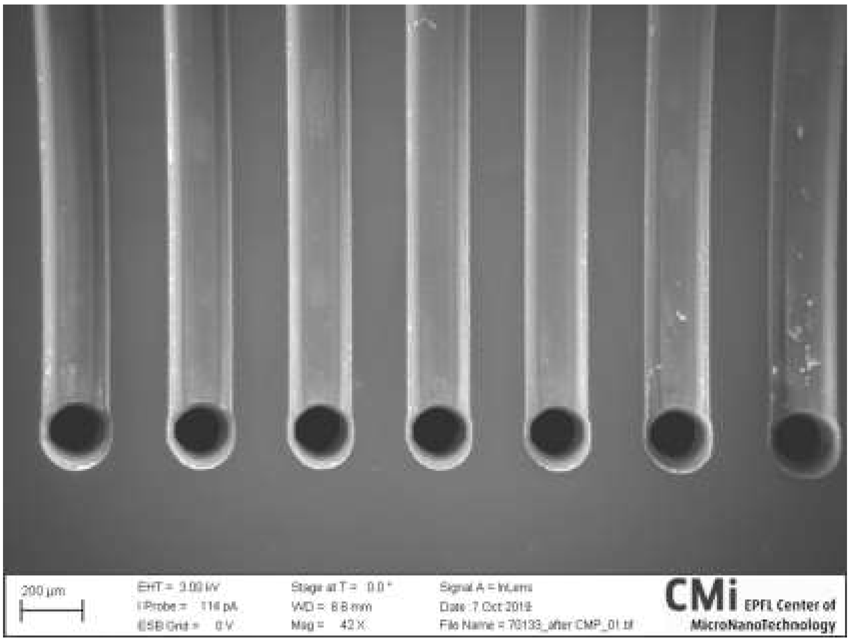

Figure 35 Silicon surface after CMP

After preparing the wafer containing the channel pattern it is now possible to perform anodic bonding with a specific tool available at CMi. The lower wafer is first loaded onto a slide where it is clamped to a vise with three clamps spaced 120 degrees apart from each other. In the same way, a second layer of Pyrex glass is laid down and tightened on the first, afterwards the slide re-enters the main body of the tool to begin processing.

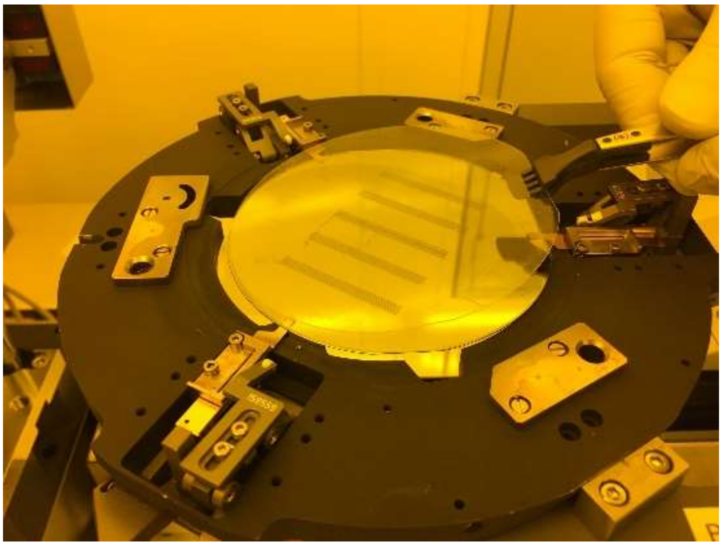

Figure 36 Before anodic bonding

For this prototype a glass upper wafer is used to take advantage of its transparency which allows to see the channels and the quality of the bonding. The anodic bonding tool works in vacuum and it is necessary to provide proper process parameters to achieve the expected results. The table below shows the list of process parameters used.

Process parameters	
Top heater temperature	350 °C
Bottom temperature	350 °C
Tool pressure	150 kPa
Voltage	1206 V

Table 5 Anodic bonding process parameter

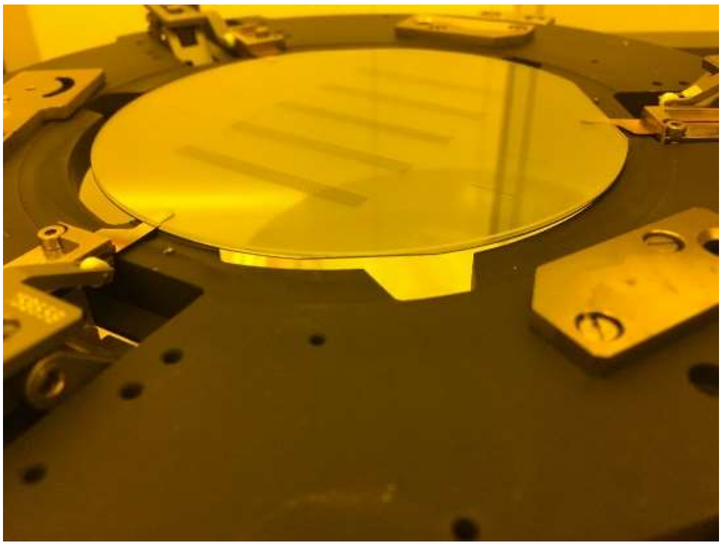

Figure 37 After anodic bonding

Evaluating the overall result obtained, it can be stated that laser etching can certainly be a valid alternative to DRIE etching in the future, but further efforts and tests are needed to fully exploit the potential of this technology.

4.2.3 KOVAR connectors and piping

Once the cooling plate has been produced, the connectors and metal pipes must be connected following the steps listed below [22]:

1. Manufacturing of KOVAR connectors;

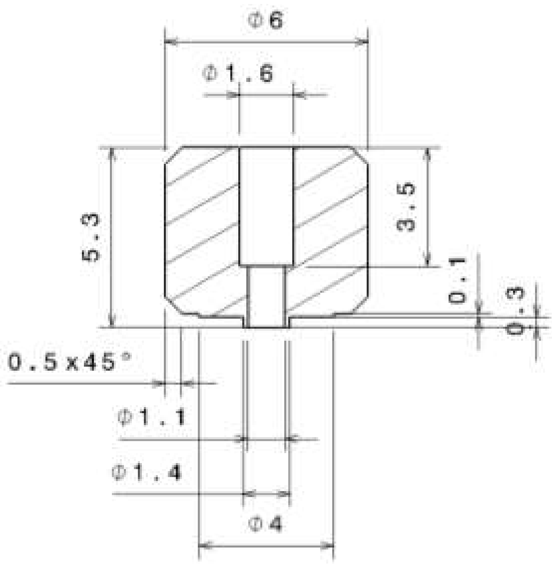

Figure 38 KOVAR connector

2. Brazing connectors to capillaries;
3. Capillaries bending;
4. Brazing capillaries to manifolds;

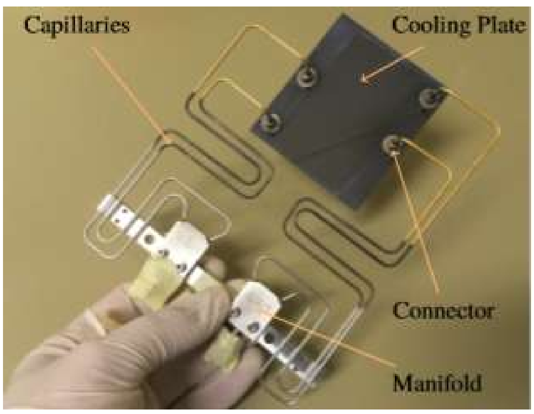

Figure 39 Cooling Plate piping [5]

5. NiAu plating of the connectors;
6. Soldering the connectors to the cooling plate.

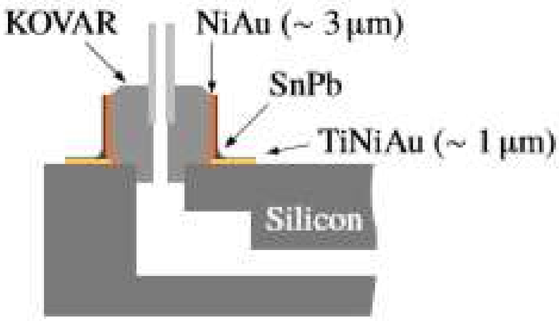

Figure 40 KOVAR connector soldering process [5]

After completing the assembly of the entire cooling circuit, it is possible to glue the electronics on the cooling plate and fix the entire apparatus on the carrier. The wire bonding is carried out only at the end of the assembly when the structure turns out to be sufficiently rigid not to break the very fragile electronic connections.

4.3 Cooling Plate CFD simulations

The design of a cooling system able to pursue the project guidelines requires the use of mathematical tools useful for understanding the fluid dynamic and thermal behavior of the whole system. In many cases, the engineering challenge can be solved with the help of consolidated analytical methods, but often these results are used as a general reference to establish the starting geometries and parameters because the models considered are too simple or based on unrealistic assumptions.

In this context, commercial CFD software allow to overcome the complexity limit imposed by solving analytical models. The generation of models of greater complexity provides a deeper knowledge thanks to which it is possible to optimize the product and at the same time reduce the number of prototypes built to achieve the desired result.

The investigations shown in this chapter aim to compare the numerical simulation solutions with the values of the main thermal and flow parameters recorded in the previous studies and in the empirical tests performed on the setup currently used in all three GTK stations. The good agreement between virtual simulations and reality can in fact become a very powerful tool for predicting the physical behavior of the system as the operating conditions change, capable of drastically reducing the design and testing times of the component. The overall study concerns only half a cooling plate since it consists of two identical hydraulic circuits of 75 channels and two manifolds each.

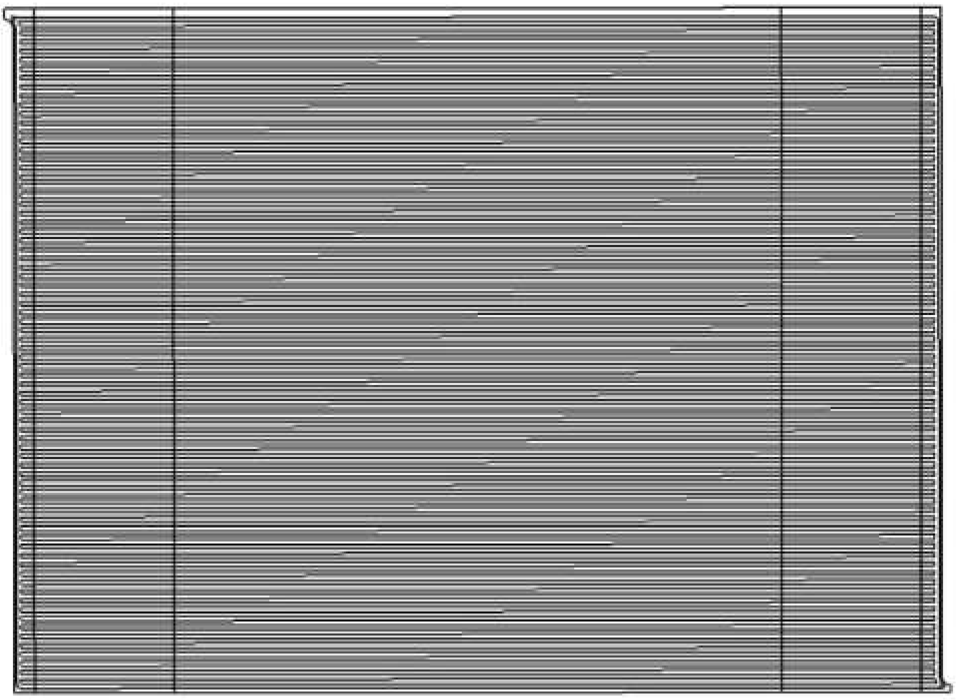

Figure 41 Overall geometry under investigation

The geometry is reproduced by means of CATIA V5 commercial software and imported to Ansys wherewith the CFD simulations run. The chapter is divided into several subparagraphs that investigate the different physical aspects of the problem by subdividing the geometric areas for reasons of computational savings.

4.3.1 Fluid dynamic analysis of a single microchannel

The efficiency of a cooling device is strongly influenced by the fluid dynamic parameters and the flow characteristics. The fluid flow conditions indeed determine the heat transfer methods (diffusive or macroscopic) and the quantities of heat exchanged on which the thermodynamic indicators taken into account to evaluate the heat sink thermal performance depend. For this reason, it is essential to know the fluid dynamic properties of the coolant before considering the thermal effects in the calculations.

In this paragraph the flow of C_6F_{14} inside a single microchannel is analyzed, calculating the pressure drop, speed, flow parameters in order to validate the numerical simulation results. The parallel arrangement of the channels suggests considering only an intermediate duct in the calculation to neglect possible edge effects at once. As shown in the previous paragraphs, the layout of the channels is designed in such a way that the total flow rate of 3 g/s is theoretically shared equally in the 150 cooling plate channels. Consequently, each channel has a coolant flow of 0.02 g/s, which corresponds to an average fluid velocity of 0.79 m/s for a 0.2 mm x 0.07 mm cross-section. Given the physical properties of the fluid and the kinematic quantities, Reynolds number may be calculated to verify the flow regime, essential for understanding the theoretical model to use for the calculation. Reynolds number turns out to be less than 2300, so the fluid regime can be defined as laminar and the fluid dynamic problem falls within the range of applicability of the Poiseuille law [18].

ANALYTIC CALCULATIONS

Data:

Microchannel geometry	[mm]
Length (l)	42
Width	0.20
Depth	0.07
Hydraulic diameter (D_h)	0.104

Table 6 Fluid dynamic simulation microchannel geometry

Working fluid	Perfluorohexane (C_6F_{14})
Density (ρ)	1805 [kg/m³]
Cinematic viscosity (ν)	$8.2 \cdot 10^{-7}$ [m²/s]
Dynamic viscosity (μ)	$1.48 \cdot 10^{-3}$ [kg/m·s]

Table 7 Working fluid properties

Reynolds number equation (2.3):

$$Re = \frac{v_m \cdot D_h}{\nu} = \frac{0.79 \cdot 1.04 \cdot 10^{-4}}{8.2 \cdot 10^{-7}} = 100.1 < 2300$$

Where:

- Re is the Reynolds number;

- v_m is the average fluid velocity.

Poiseuille law for laminar flow (2.15):

$$\Delta p = f \cdot \rho \cdot \frac{l}{D_h} \cdot \frac{{v_m}^2}{2} = \frac{67.48}{Re} \cdot 1805 \cdot 403.85 \cdot 0.31 = 1.54 \cdot 10^5\ Pa = 1.54\ bar$$

Where:

- Δp is the pressure drop;

- v_m is the average fluid velocity;
- f is the Darcy factor for a rectangular duct cross-section calculated by interpolating.

Cross-section	Aspect ratio	Nu constant temperature	Nu constant heat flux density	Darcy factor
Rectangular	1	2.98	3.61	56.92/Re
	2	3.39	4.12	62.20/Re
	3	3.96	4.79	68.36/Re
	4	4.44	5.33	72.92/Re
	6	5.14	6.05	78.80/Re
	8	5.60	6.49	82.32/Re
	∞	7.54	8.24	96.00/Re

Table 8 Nusselt number and Darcy factor values for different aspect ratios [18]

$$\text{Aspect Ratio} = 2.86 \;\Rightarrow\; \text{Darcy factor } f = \frac{67.48}{Re}$$

SIMULATION WORKING HYPHOTESIS

The mathematical model developed is based on the following simplifying hypotheses:

- Steady fully developed flow after the developing length at the entrance;
- The fluid can be treated as a continuum medium;
- Incompressible flow;
- Laminar flow;
- Surface roughness has negligible effects (No data available on the matter).

SIMULATION DOMAIN

The geometry is a simple channel whose dimensions are specified in the table above, which represents the fluid domain of the problem. The sidewalls are defined by the boundary condition imposed in the following steps.

MESH

The simulation domain is divided into hexahedral volumes with the aim of creating a structured mesh, beneficial for time calculation reduction and for an easier mesh generation. The mesh is even self-contained with a view to the grid independence analysis, in order to keep approximately the same general shape and structure of the mesh as the number of elements increases. In addition, smooth inflation mesh near the walls and at the entrance are generated to reproduce the boundary layer and to notice more details about velocity profiles in the flow developing zone respectively.

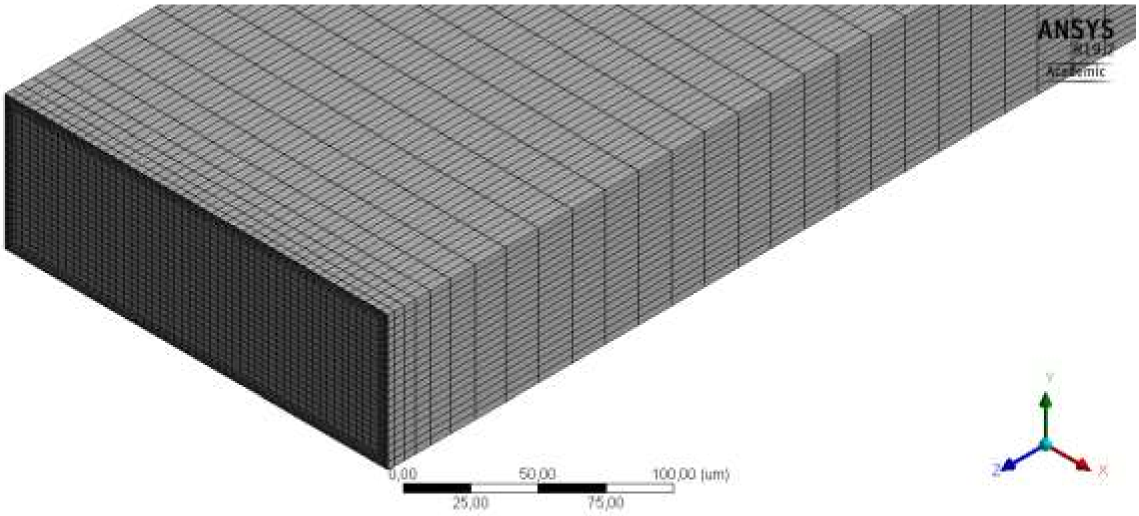

Figure 42 Generated mesh showing inflation both near sidewalls and at the entrance

BOUNDARY CONDITIONS

The boundary conditions applied to the model are listed below:

- Mass flow inlet equal to 0.02 g/s at the inlet;
- Atmospheric outlet pressure;
- No slip condition at sidewalls.

SIMULATION SOLUTION AND CONVERGENCE

The solution of the NSF system of differential equation is entrusted to the solver "Ansys Fluent", which uses a pressure-based solution method.

Convergence is judged by following the standard of convergence of the scaled residuals according to which the scaled residuals must decrease to 10^{-6} and 10^{-3} respectively for the energy equation and all the other equations in the system [23]. However, it is good practice to also check the convergence of balance equations and of significant integral quantities such as pressure or temperature.

This simulation does not manage thermal phenomena, therefore the energy equation has been excluded in the calculation. The model is properly structured and the convergence fully acceptable, since all the criteria taken into account have been met.

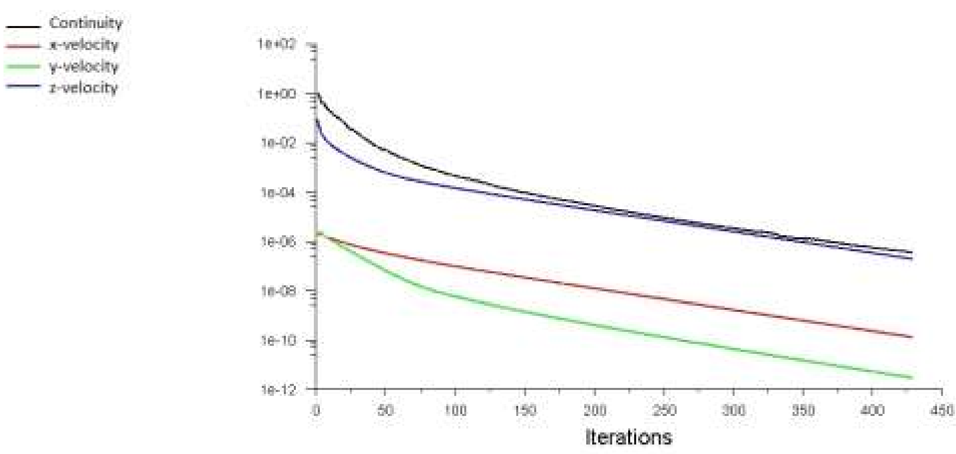

Figure 43 Scaled residuals convergence plot

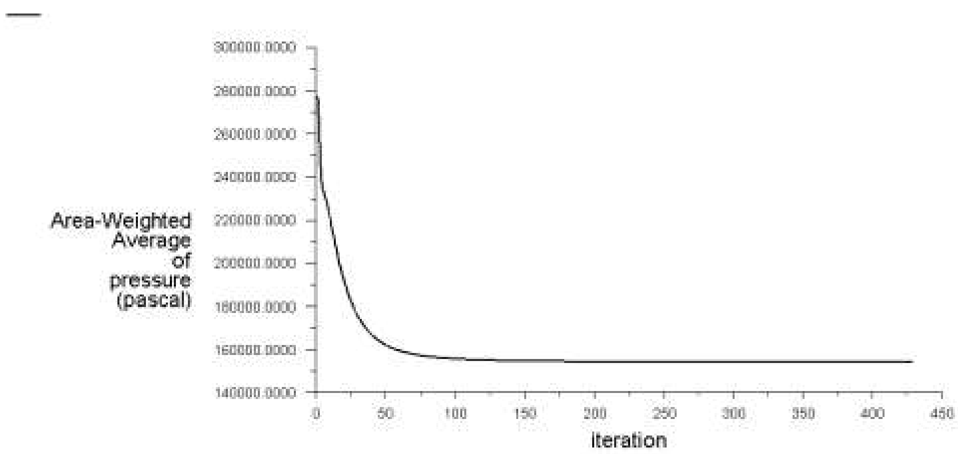

Figure 44 Inlet pressure convergence plot

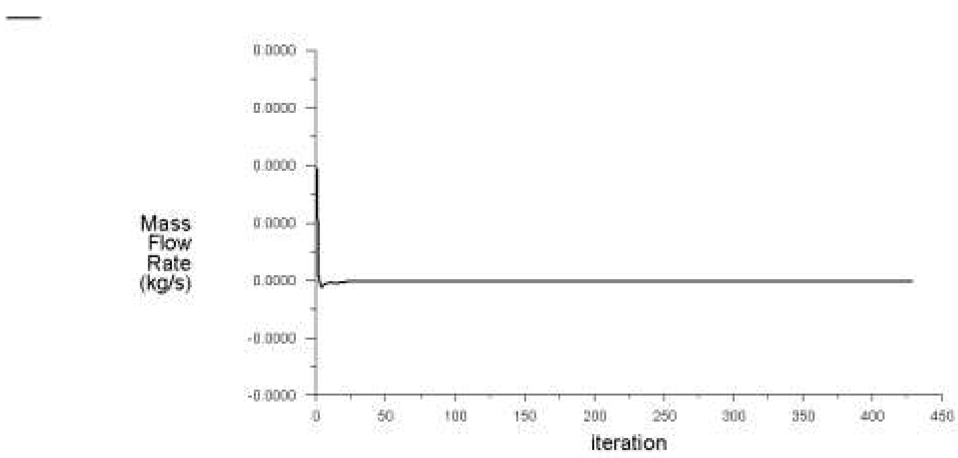

Figure 45 Conservation of mass convergence plot

SIMULATION RESULTS

The simulation post-processing reveals that the parabolic velocity profiles of laminar motion in both cutting planes have been obtained. The boundary layer and the developing flow zone are clearly visible while the definitive parabolic profile is reached 1.9 mm beyond the entrance section. Finally, the values of pressure drop and average speed meet the expected values.

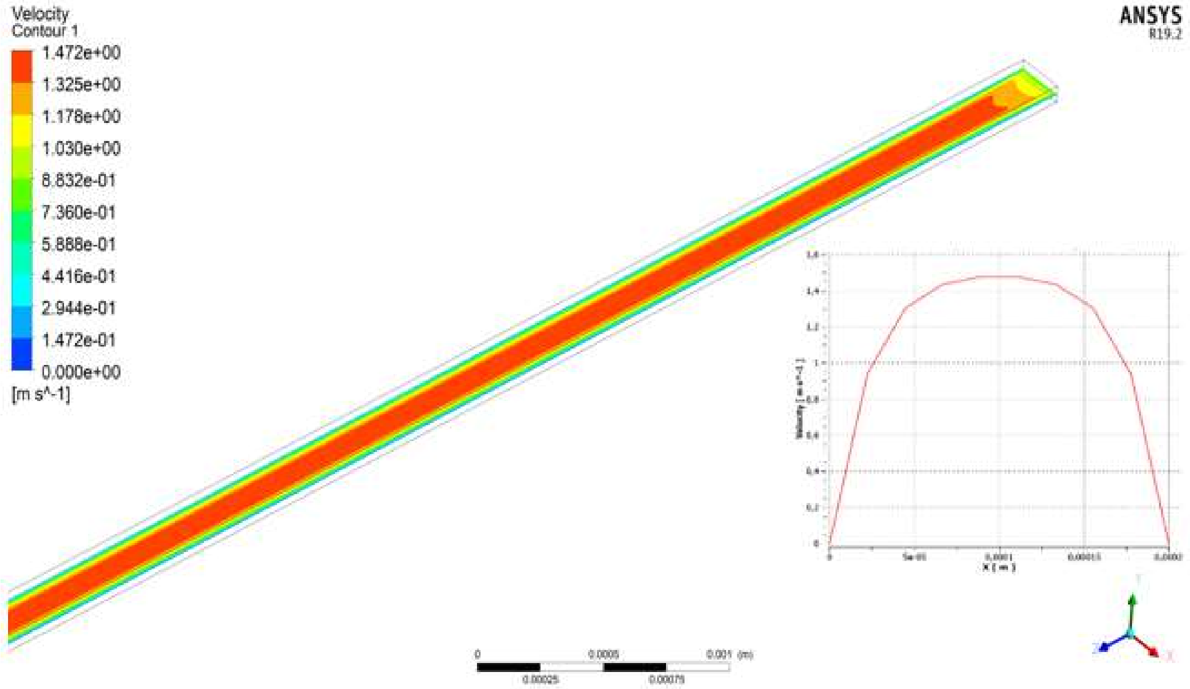

Figure 46 XZ Cutting plane velocity contour. The chart shows the developed flow parabolic profile

GRID INDEPENDENCE STUDY AND VALIDATION

It is usually recommended to iterate the numerical calculations, decreasing the size of the elements of the discretization to assess the stability of the solution. In this regard, it is very important that the numerical values tend to a constant value as the number of elements of the mesh increases. This check is commonly called “Grid independence analysis”. In this case, the mesh density is expressed by the number of nodes. As the number of nodes increases, there is always an increase in the computational time per iteration, therefore it is worth to seek a compromise between the computational burden and the accuracy of the result. Table 9 shows the results derived from simulations performed with three different meshes. Validation of the results follows through comparison with analytical calculation.

	N° of nodes	Inlet pressure	Computational time/iteration
Mesh 1	2977051	1.54 bar	10.93 s
Mesh 2	1590226	1.54 bar	5.73 s
Mesh 3	669591	1.53 bar	2.29 s
Analytic solution		1.54 bar	

Table 9 Fluid dynamic simulation results

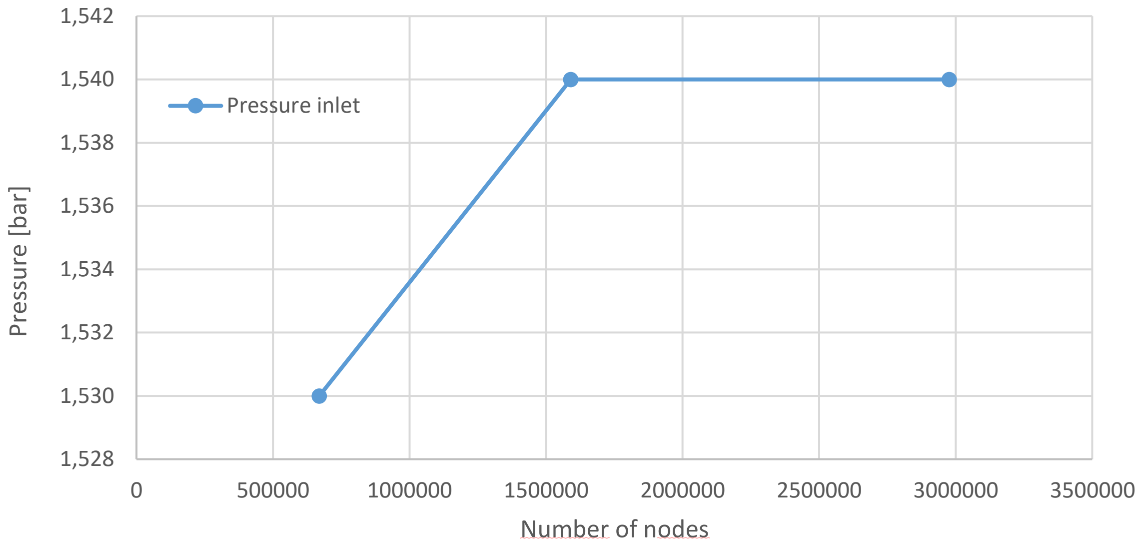

Chart 2 Fluid dynamic simulation grid independence: pressure inlet

4.3.2 Thermofluidynamic analysis

To evaluate the thermal performance of the cooling plate, it is necessary to develop a second model which introduces both the heat sources and the components to be cooled. On this occasion, the solver also needs to solve the energy equation, set aside in the fluid dynamic simulation, to calculate the temperature at any point of the domain. The calculation therefore becomes more expensive in terms of computational cost and this entails the need to reduce the number of elements as much as possible. The quantity of elements can be reduced by increasing their size, but this has a strong impact on the accuracy of the result if the grid is not dense enough to effectively understand the characteristics of the phenomenon. The best solution is to reduce the size of the computing domain, looking for the most compact model representative of the problem. The model developed (Figure 47) considers a section of the entire system including electronics and radiator, that represents an intermediate microchannel of the cooling plate and the respective overlying portions of the ASIC chips and sensor. The width of the model depends on the pitch between the channels, because a specific area to be cooled is assigned to each channel. The geometry does not include the integrated manifolds to not simulate 75 parallel channels and because they do not lie directly under the heat sources. Although the silicon, in which the manifolds are etched, has a high coefficient of thermal conductivity, it is necessary to make this simplification to reach a compromise between the accuracy of the model and the computational burden.

ANALYTIC CALCULATION

Before running the simulations, a simple analytical calculation is performed with Excel, to roughly reproduce the temperature profile of the fluid inside the channel. The object of study is a rectangular cross-section channel as long as the largest dimension of the TDCpix under which the channel lies. A constant heat flux density is applied to the side walls of the channel. The heat flux density value varies according to the longitudinal coordinate of the channel that crosses the two EoC areas and the pixel matrix which dissipate 4.8 W/cm² and 0.4 W/cm² respectively. Since silicon is a good thermal conductor, the temperature at the edges of the channel is constant and therefore the boundary condition H1 described in chapter 2 can be used. The analytical model operates with a fully developed flow and neglects the thermal effects at the inlet, therefore the temperature difference between the fluid and the adjacent walls is constant as the longitudinal coordinate of the channel changes.

The fluid temperature profile is obtained solving the capacity heat transfer equation for Tout and reformulating the term of thermal flow so as to distribute the thermal flow generated on the upper surface of the chip on the lateral surface of the channel.

Capacity heat transfer equation [8]:

$$T_{fout} = T_{fin} + \frac{\dot{Q}}{c_p \cdot G} \tag{4.1}$$

Where:

- T_{fout} is the fluid outlet temperature;
- T_{fin} is the fluid inlet temperature;
- $\dot{Q}$ is the heat flux dissipated from the TDCpix upper surface;
- c_p is the specific heat coefficient;
- G is the mass flow rate.

Heat flux density:

$$\dot{q} = \frac{\dot{Q}}{A} \tag{4.2}$$

Equivalent heat flux density:

$$\dot{q}_c = \frac{\dot{q} \cdot A}{A_c} \tag{4.3}$$

Where:

- $\dot{q}_c$ is the equivalent heat flux density;
- $\dot{q}$ is the heat flux density dissipated from the TDCpix upper surface;
- A_c is the channel lateral surface;
- A is the TDCpix area deriving from the product between the pitch and the length of a couple of TDCpix (equal to microchannel length).

$$A = l \cdot p \tag{4.4}$$

The next step is to calculate the linear heat flux density and to make the longitudinal coordinate explicit in the T_{fout} formula.

$$\dot{q}_l = \dot{q}_c \cdot P \tag{4.5}$$

Where:

- $\dot{q}_l$ is the linear heat flux density;
- P is the perimeter of the channel cross-section.

At this point it is possible to calculate the temperature of the fluid along the x coordinate.

$$T_{fout} = T_{fin} + \frac{\dot{q}_l \cdot x}{c_p \cdot G} \tag{4.6}$$

The adjacent wall temperature or rather the temperature offset to be added to the temperature of the fluid at the inlet is obtained by combining the convective heat transfer equation with the capacity heat transfer equation [8].

$$\frac{d\dot{Q}_c}{dx \cdot P} = h \cdot \left(T_w(s) - T_f(s)\right) \tag{4.7}$$

Where:

- $\dot{Q}_c$ is the equivalent heat flux;
- h is the convective heat transfer coefficient;
- T_w is the adjacent wall temperature;
- T_f is the fluid temperature.

For a round channel (2.4):

$$Nu = \frac{h \cdot D}{k}$$

The diameter can be reduced:

$$\frac{d\dot{Q}_c}{dx} = \pi \cdot Nu \cdot k \cdot \left(T_w(s) - T_f(s)\right) \tag{4.8}$$

For a round channel $\dot{Q}_c$ is independent from the diameter [8].

To take the rectangular section into account, a multiplicative coefficient must be added [8]:

$$C = \frac{\pi \cdot D_h}{2w \cdot 2h} \tag{4.9}$$

Where:

- w is the channel width;
- h is the channel depth.

C is a ratio between the two perimeters and it is equal to 1 if a round cross-section is considered and < 1 for a rectangular channel [8].

$$\frac{d\dot{Q}_c}{dx} = \frac{\pi \cdot Nu \cdot k}{C} \cdot \left(T_w(s) - T_f(s)\right) \tag{4.10}$$

$T_f(s)$ can be expressed as follows [8]:

$$T_f(s) = \frac{1}{G \cdot c_p} \cdot \int_0^x \frac{d\dot{Q}_c}{dx} dx \tag{4.11}$$

The power dissipated by the readout electronics is constant, so inserting into (4.10) [8]:

$$\frac{d\dot{Q}_c}{dx} = \frac{\pi \cdot Nu \cdot k}{C} \cdot \left(T_w(s) - \frac{1}{G \cdot c_p} \cdot \frac{d\dot{Q}_c}{dx} \cdot x\right) \tag{4.12}$$

The Poiseuille law for rectangular channel can be solved for the mass flow rate in that way [24]:

$$G = \frac{K_f(h,w) \cdot \min(h,w)^3 \cdot \max(h,w) \cdot \Delta p}{12 \cdot \nu \cdot l} \tag{4.13}$$

Where:

- K_f is a geometric dimensionless coefficient [8];

$$K_f(h,w) = 1 - \sum_{i=1}^{\infty} [\frac{1}{(2i-1)^5} \cdot \frac{192}{\pi^5} \cdot \frac{\min(h,w)}{\max(h,w)} \cdot \tanh\left[\frac{(2i-1) \cdot \pi}{2} \cdot \frac{\min(h,w)}{\max(h,w)}\right] \tag{4.14}$$

K_f is equal to 0.78 for a 0.2 mm x 0.07 mm cross-section [8].

$$T_w(s) = \frac{d\dot{Q}_c}{dx} \cdot \left(\frac{C}{\pi \cdot k \cdot Nu} + \frac{12 \cdot \nu \cdot l}{c_p \cdot K_f \cdot \min(h,w)^3 \cdot \max(h,w) \cdot \Delta p} x\right) \tag{4.15}$$

Data:

Microchannel geometry	[mm]
Length (l)	39.4
Width	0.20
Depth	0.07
Hydraulic diameter (D_h)	0.104

Table 10 Thermofluidynamic simulation microchannel geometry

Working fluid	Perfluorohexane (C_6F_{14})
Density (ρ)	1805 [kg/m³]
Cinematic viscosity (ν)	$8.2 \cdot 10^{-7}$ [m²/s]
Dynamic viscosity (μ)	$1.48 \cdot 10^{-3}$ [kg/m·s]
Specific heat (c_p)	975 [J/(kg·K)]
Thermal conductivity (k)	$6.27 \cdot 10^{-2}$ [W/(m·K)]

Table 11 Working fluid thermofluidynamic properties

Solid	Silicon
Density (ρ)	2330 [kg/m³]
Specific heat (c_p)	700 [J/(kg·K)]
Thermal conductivity (k)	124 [W/(m·K)]

Table 12 Silicon properties

RESULTS

The calculation shows a fluid outlet temperature of 272.4 K and the plot of results is in line with expectations. The constant temperature difference between the solid wall and the fluid mass is evident, as well as unrealistic temperature jumps in the areas that dissipate different amounts of heat.

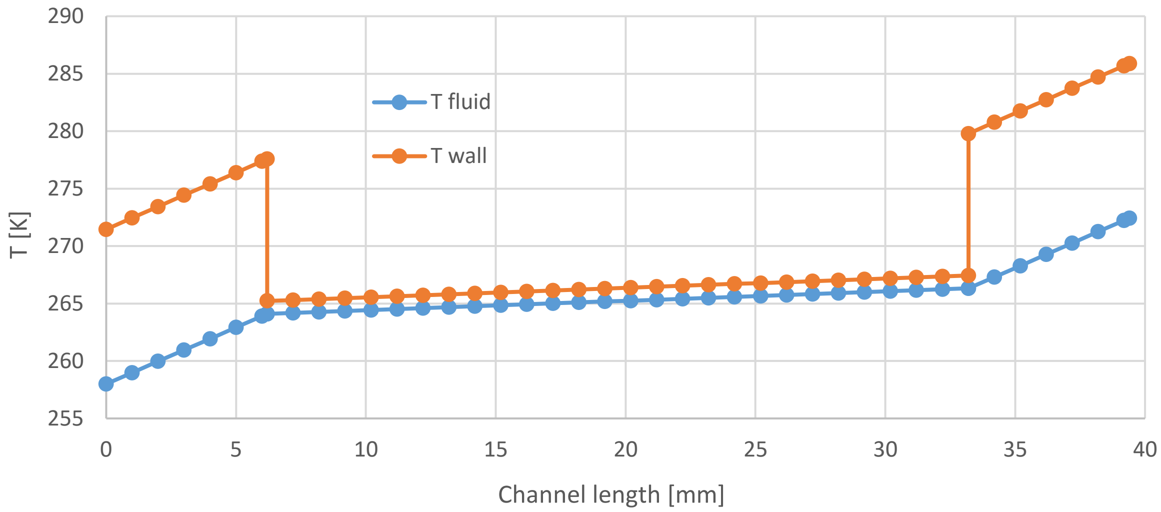

Chart 3 Temperatures along the channel

ENTRANCE EFFECT NEGLECTION

As stated in chapter 2, the development of the flow at the entrance of the channel causes alterations in the thermofluidynamic behavior of the system, but in this case, they can be neglected because the Graetz number (2.13) is lower than the threshold value [13].

$$Gz = \frac{Re \cdot Pr \cdot D_h}{l} = \frac{100.1 \cdot 23 \cdot 1.04 \cdot 10^{-4}}{4.2 \cdot 10^{-2}} = 5.5 < 10$$

Where:

- Gz is the Graetz number;
- Pr is the Prandtl number;
- l is the channel length.

SIMULATION WORKING HYPHOTESIS

The mathematical model developed is based on the following simplifying hypotheses:

- Steady fully developed flow after the developing length at the entrance;
- The fluid can be treated as a continuum medium;
- Incompressible flow;
- Laminar flow;
- Surface roughness has negligible effects (No data available on the matter);
- The thermophysical properties of the fluid do not vary with the temperature;
- Viscous heating can be neglected (Only 0.1°C of temperature increasing).

SIMULATION DOMAIN AND BOUNDARY CONDITIONS

The simulation domain is divided exactly in half to halve the number of elements obtaining the same result. it is therefore necessary to reduce the input flow from 0.02 g/s to 0.01 g/s and apply the symmetry constraint along the whole sectioned surface of the model. The outlet pressure is set at 0 bar and the no slip condition is used on the walls of the channel. Three constant wall heat flux boundary conditions are imposed on the upper TDCpix surface whereas all the other external walls of the model are considered adiabatic, since the entire system operates in vacuum and the radiative heat exchange is neglected.

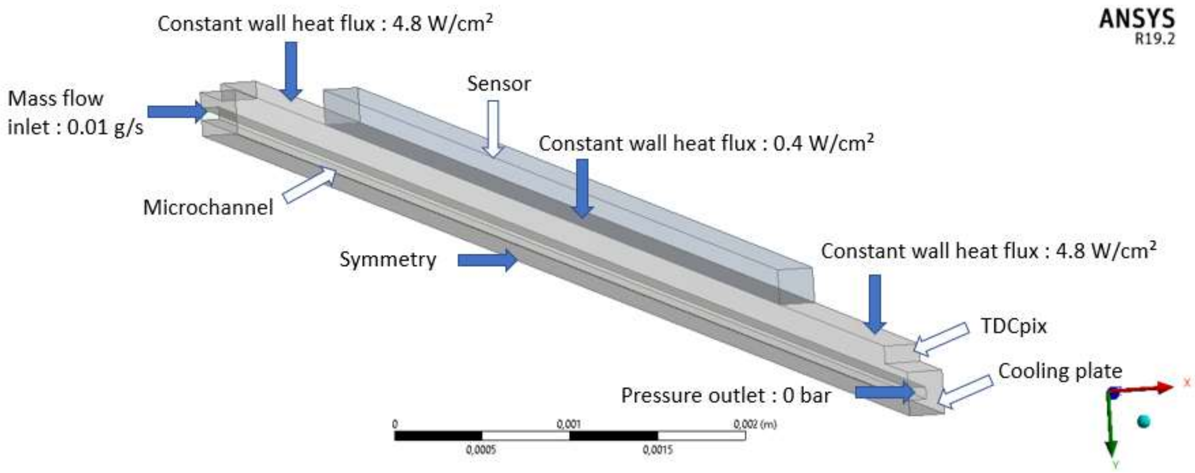

Figure 47 Boundary conditions

MESH

The mesh has the same characteristics described in the previous simulation as regards the fluid part, while it does not have boundary layers and inflations in the solid part where the elements are larger, since only diffusive phenomena occur outside the perimeter of the channel.

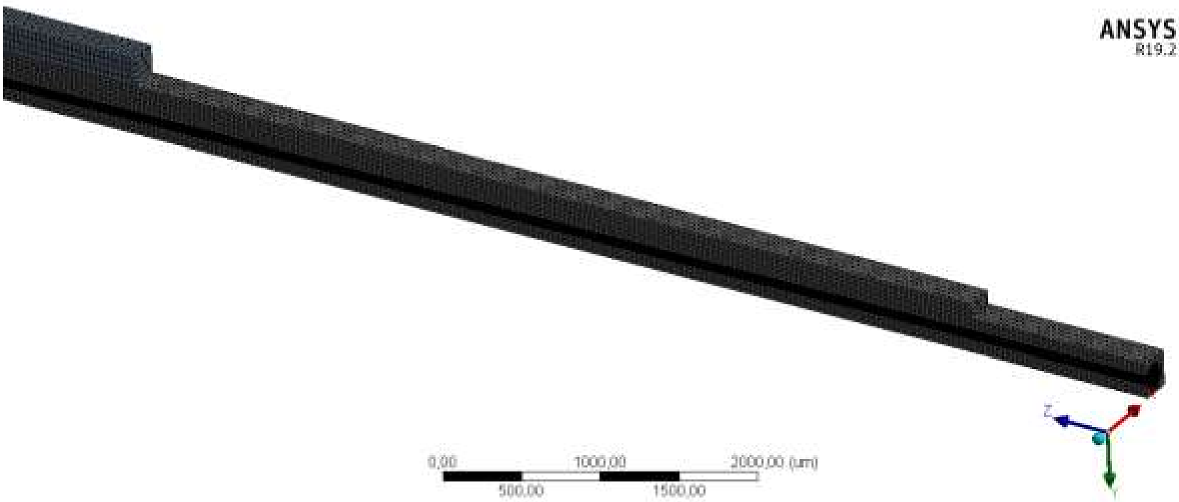

Figure 48 Mesh

SIMULATION SOLUTION AND CONVERGENCE

The criteria considered for judging the convergence are the same as those stated in the previous chapter, but the convergence of the value of the fluid outlet temperature and the balance of heat fluxes is also assessed. All the convergence requirements have been fulfilled again.

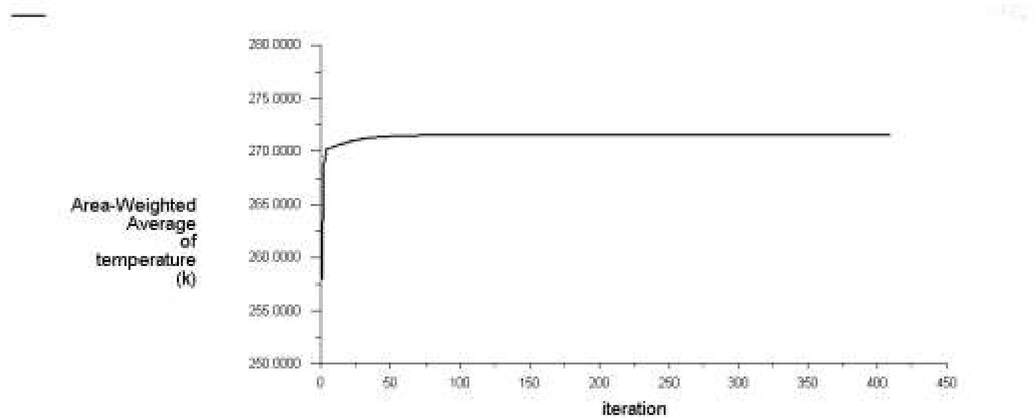

Figure 49 Fluid outlet temperature convergence plot

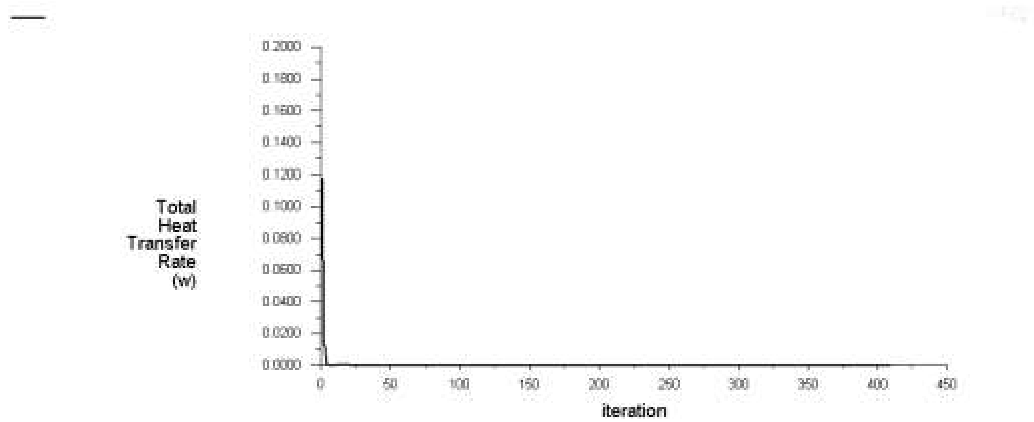

Figure 50 Energy conservation convergence plot

SIMULATION RESULTS

Simulation results show a temperature trend consistent with that obtained analytically. In the figure below the temperature plot is clearly visible and it differs from the theoretical outcome in the continuity of temperature variations. The boundary condition H1 is adequate for the theoretical description of the model even though the CFD analysis shows variations at the entrance of the channel and at the areas bordering two different heat flux boundary conditions. A certain channel length is therefore needed to replicate the same response suggested by the analytical model. The decrease in temperature difference recorded at the two ends of the channel is due to the lack of thermal source above these areas. Furthermore, in the entrance area this is partly due to the presence of thermal effects at the entrance described in chapter 2.

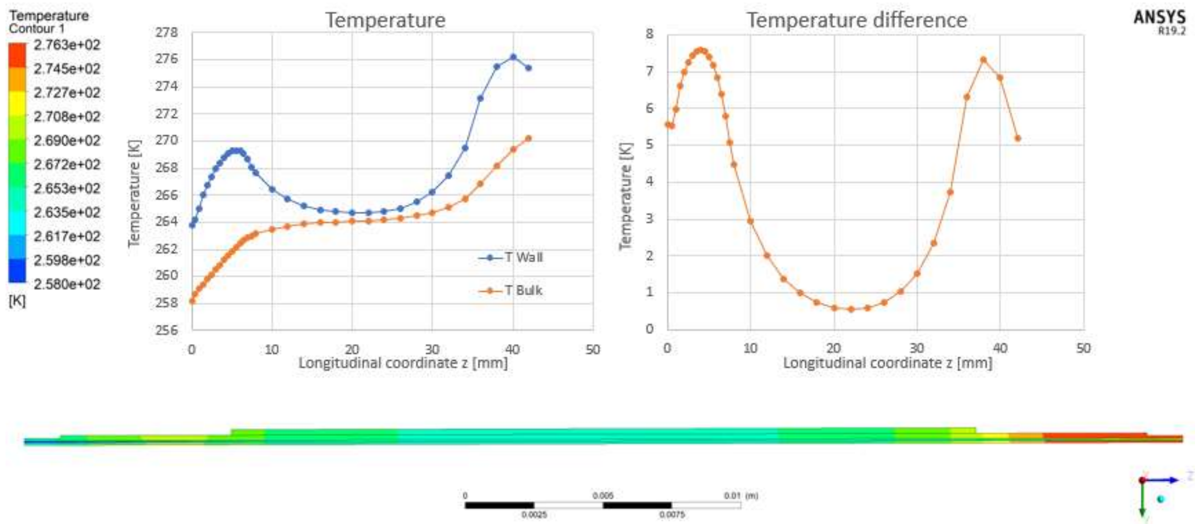

Figure 51 Temperature plot and contour

GRID INDEPENDENCE AND VALIDATION

The solution is stable when the size of the elements changes and the recorded values are validated both experimentally and analytically. The analytical measurement is carried out with a temperature probe positioned about 50 cm from the exit of the cooling plate, because of the modest size of the channels and the difficulty of accessing the area of interest. Much effort is being made to reproduce the temperature profile with a thermal imaging camera, but adequate accuracy has not yet been achieved to validate the CFD simulations.

	N° of nodes	Inlet pressure	Mean outlet temperature	Computational time/iteration
Mesh 1	2349723	1.54 bar	271.65 K	15.57 s
Mesh 2	1210120	1.54 bar	271.64 K	6.59 s
Mesh 3	582142	1.50 bar	271.58 K	2.31 s
Mesh 4	220322	1.47 bar	271.46 K	1.12 s
Mesh 5	130114	1.46 bar	271.43 K	0.60 s
Measurement			272.50 K	
Analytic solution		1.54 bar	272.40 K	

Table 13 Thermofluidynamic simulation results

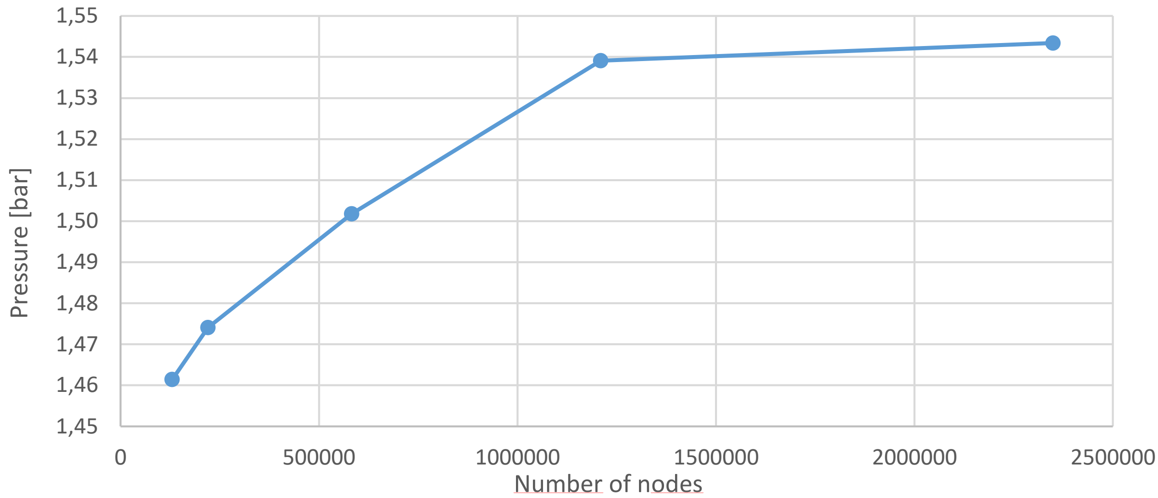

Chart 4 Thermofluidynamic simulation grid independence: pressure inlet

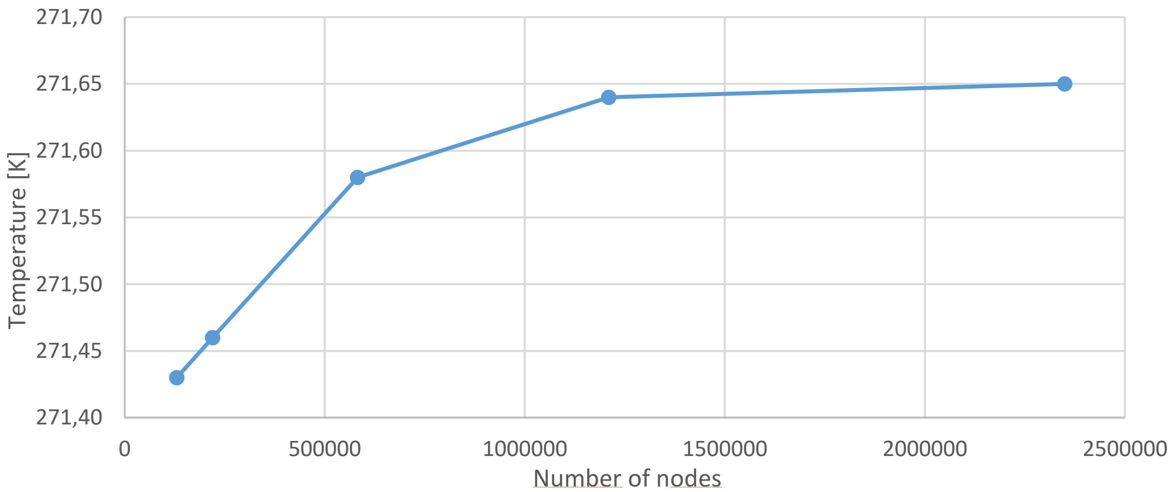

Chart 5 Grid independence: mean outlet temperature

Deviations from empirical data less than 1°C, are judged fully acceptable considering the simplifications introduced by the model, but further investigations have been made by observing the response of the system to the increasing complexity of the model.

SIMULATION MODEL REFINEMENT

In order to try to better understand the behavior of the system, the degree of detail of the virtual model has been increased. Two further thermal interfaces have been introduced by adding the bump bonds connections and the glue layer between the sensor and the ASIC chips into the geometric domain. Barrel-shaped bump bonds are modeled as cylinders of 30 microns in diameter and 25 microns in height and are positioned at each pixel. They are made of a

SnAg alloy while the adhesive tape interposed between the two electronic components is 20 microns thick and is in epoxy glue.

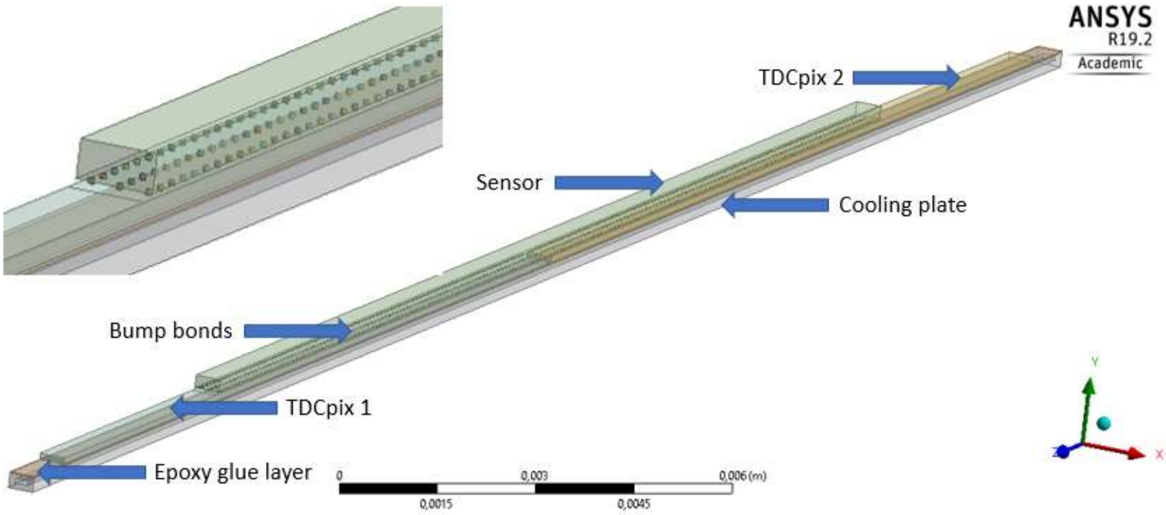

Figure 52 Simulation domain

Material properties	SnAg alloy	Epoxy glue
Density [kg/m³]	7300	1200
Thermal conductivity [W/m·K]	9	0.6
Specific heat [J/kg·K]	228	1256

Table 14 Bump bonds and glue material properties

The density and specific heat values for the bump bonds and for the glue are obtained respectively from the physical characteristics of the tin because the alloy composition is mainly tin based and from the average values of a solid phase epoxy polymer. These data are used because more detailed information about these materials is not available. The thermal conductivity coefficients are instead acquired from previous studies carried out at CERN using the same materials [25].

SIMULATION RESULTS AND VALIDATION

Simulation results reveal a general increase in the temperatures of the electronic components due to the greater difficulty encountered during the heat transfer caused by the introduction of two thermal interfaces with low thermal conductivity. The following figure shows the chip and sensor temperatures as the longitudinal coordinate changes by comparing the two simulations performed. The chip temperatures in the complex model are higher along the entire length of the channel and their trend appears shifted towards the entrance compared to the previous simulation. There are also temperature rises in the sensor, but despite this the temperature distribution in the sensor is rather different from that provided by experimental measurements. The measurements provided come from experimental tests held on a test bench and carried out using 4 resistance thermometers installed on the silicon upper surface. It is assumed that the high temperature values obtained may be due to the poor adhesion of the probe on the silicon surface. It is reported that by improving the adhesion of the probe to the surface the recorded temperature decreases, probably because the sensor surface is colder than the probe contact element. The temperature profile provided by the simulations is therefore experimentally validated while the differences found in terms of absolute value can be attributed to the causes mentioned above.

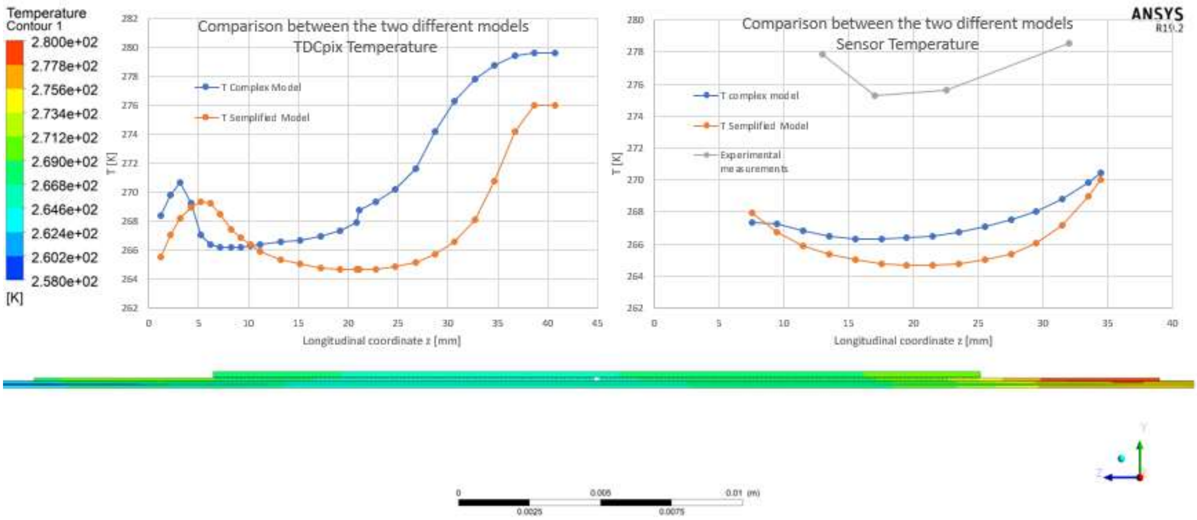

Figure 53 Temperature contour and comparison with the simplified model

4.3.3 Flow simulation in manifolds

This paragraph analyzes the flow of the coolant inside the manifolds which has so far been neglected. Manifolds are responsible for distributing and collecting the fluid, but they must also exhibit a low pressure drop and a ensure regular flow. The pressure drop generated in the two manifolds is added in series to that created in the microchannel, therefore it is important to correctly design the shape and size of the collectors so as not to exceed the 3 bar limit established. Since experimental estimates of pressure losses in the cooling plate are not available, simulation results are validated by means of an analytical model. Three different simulations are performed concerning the input manifold, the output manifold and the entire hydraulic circuit respectively with the aim of comparing the results obtained by adding the head losses generated in the two manifolds and in the microchannel with a single computationally expensive simulation.

ANALYTIC CALCULATION

Before calculating the pressure losses, it is essential to understand the type of flow occurring in the manifolds. As happens in microchannels, the flow is laminar also inside the manifold (2.3).

$$Re = \frac{\rho \cdot v_m \cdot D_h}{\nu} = \frac{1805 \cdot 1.85 \cdot 4.76 \cdot 10^{-4}}{8.2 \cdot 10^{-7}} = 1078.1 < 2300$$

Hence, the Poiseuille law for laminar flow can be used. The calculation is performed with an Excel file in order to replicate the aforementioned formula for head losses as the flow rate in the manifold decreases. This decrease is due to the progressive filling of the parallel channels. The calculation takes into account both distributed and concentrated head losses.

Distributed head losses formula (2.15):

$$\Delta p = f \cdot \rho \cdot \frac{l}{D_h} \cdot \frac{{v_m}^2}{2}$$

Concentrated head losses formula (2.17):

$$\Delta p = \beta \cdot \rho \cdot \frac{{v_m}^2}{2}$$

Coefficient	$\boldsymbol{\beta}$
T-junctions (branching)	0.5
Narrowing cross-section	0.45
Widening Cross-section	0.75
T-junctions (confluence)	0.5

Table 15 Concentrated head losses coefficients [31]

Results:

Manifolds	**Δp [bar]**
Distributed	0.06
Concentrated	0.01
Total	0.07

Table 16 Manifolds pressure drop

Microchannel	**Δp [bar]**
Distributed	1.54

Table 17 Microchannel pressure drop

Hydraulic circuit	**Δp [bar]**
Total	1.61

Table 18 Total pressure drop

SIMULATION DOMAIN

Both the inlet and outlet manifolds have a 1.6 mm x 0.28 mm rectangular cross-section and a length of 30.2 mm, but in order to replicate the same geometry of the analytical model, the curved section near the connectors has been neglected. Lastly, 75 channels long enough to guarantee the flow development are connected to the collector.

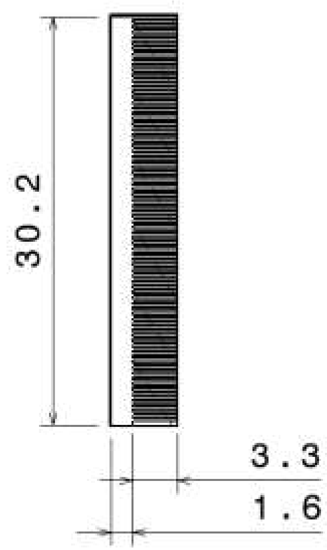

Figure 54 Manifold main dimensions

WORKING HYPHOTESIS AND BOUNDARY CONDITIONS

The working hypotheses are the same described in paragraph 4.3.1 while the boundary conditions listed below are common to all three simulations.

- Mass flow inlet equal to 1.5 g/s;
- Atmospheric pressure outlet;
- No slip condition at sidewalls.

SIMULATION RESULTS AND VALIDATION

INLET MANIFOLD

Inlet manifold	N° of nodes	Pressure drop*	Computational time/iteration
Mesh 1	221816	0.03 bar	0.53 s
Mesh 2	823536	0.05 bar	2.34 s
Mesh 3	2124558	0.06 bar	6.99 s
Analytic solution		0.07 bar	

Table 19 Inlet manifold simulation results

* The pressure drop of the channel is excluded.

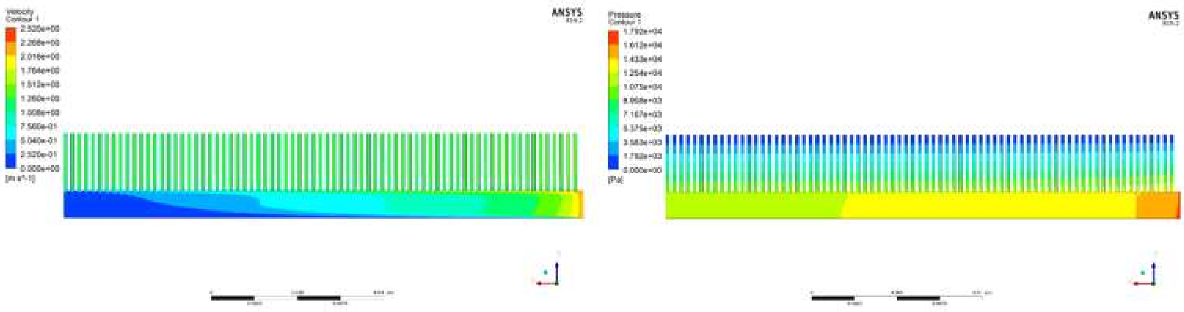

Figure 55 Inlet manifold. Velocity contour on the left and pressure contour on the right

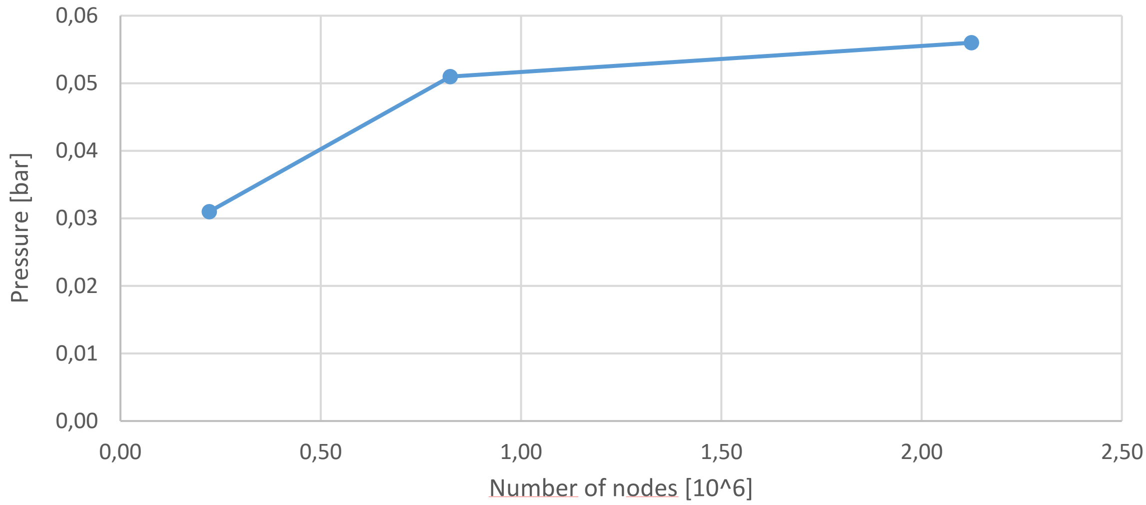

Chart 6 Grid independence: inlet manifold pressure drop

OUTLET MANIFOLD

Outlet manifold	N° of nodes	Pressure drop*	Computational time/iteration
Mesh 1	221816	0.09 bar	0.57 s
Mesh 2	823536	0.11 bar	2.51 s
Mesh 3	2124558	0.11 bar	6.49 s

Table 20 Outlet manifold simulation results

* The pressure drop of the channel is excluded.

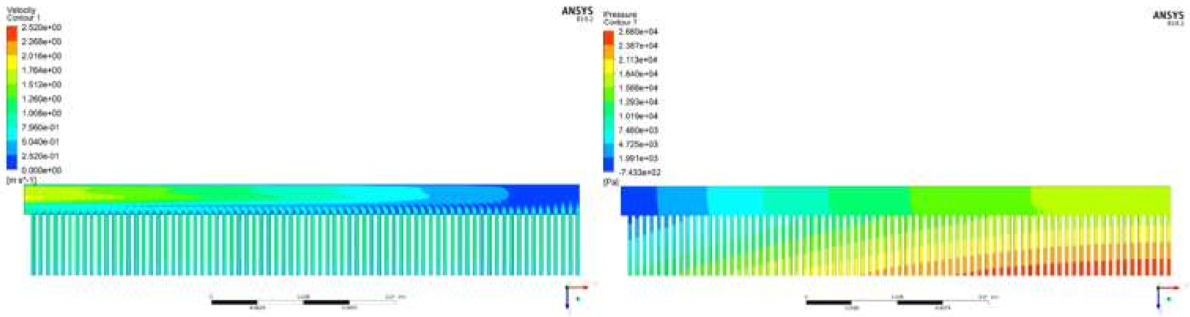

Figure 56 Outlet manifold. Velocity contour on the left and pressure contour on the right

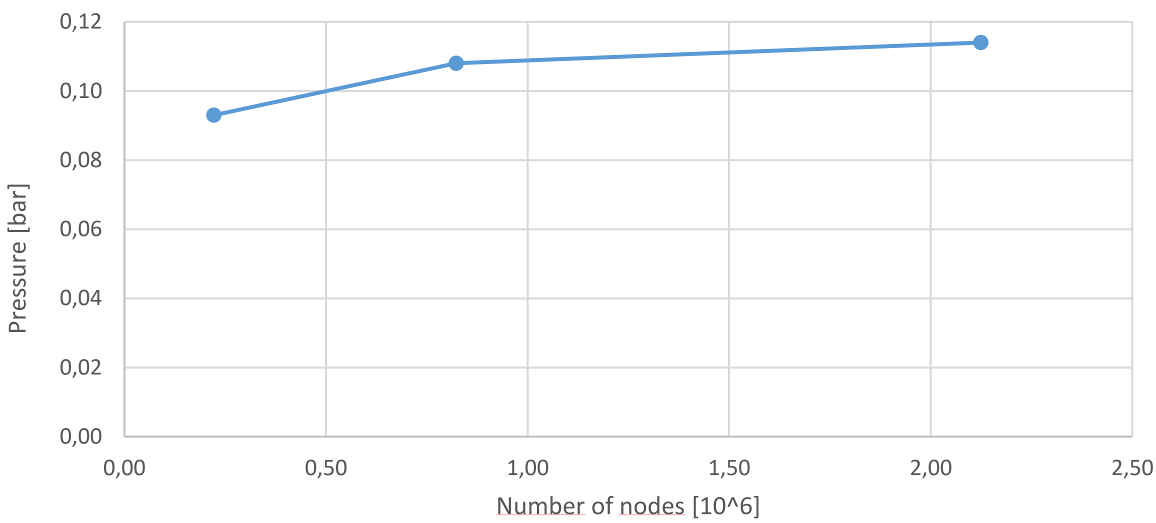

Chart 7 Grid independence: outlet manifold pressure drop

VALIDATION

The total pressure drop in the hydraulic circuit is calculated by adding the contributions relating to the two manifolds to the pressure loss generated in the microchannel calculated in paragraph 4.3.1.

Simulation domain	Pressure drop
Inlet manifold	0.06 bar
Microchannel	1.54 bar
Outlet manifold	0.11 bar
Total	1.71 bar
Analytic result	1.61 bar

Table 21 Fluid dynamic simulations validation

The validated result is now compared with an alternative simulation domain representing the entire hydraulic systems, which is expected to require a higher computational burden.

Hydraulic circuit	N° of nodes	Pressure drop	Computational time/iteration
Mesh 1	588489	1.43 bar	1.46 s
Mesh 2	1841225	1.56 bar	4.95 s
Mesh 3	2596625	1.62 bar	6.88 s
Mesh 4	4731564	1.64 bar	13.51 s
Analytic solution		1.62 bar	

Table 22 Entire hydraulic circuit simulation validation

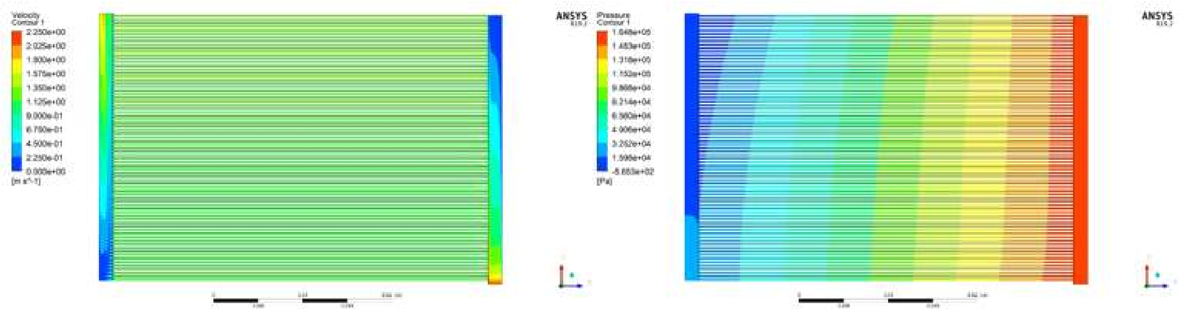

Figure 57 Cooling Plate hydraulic circuit. Velocity contour on the left and pressure contour on the right

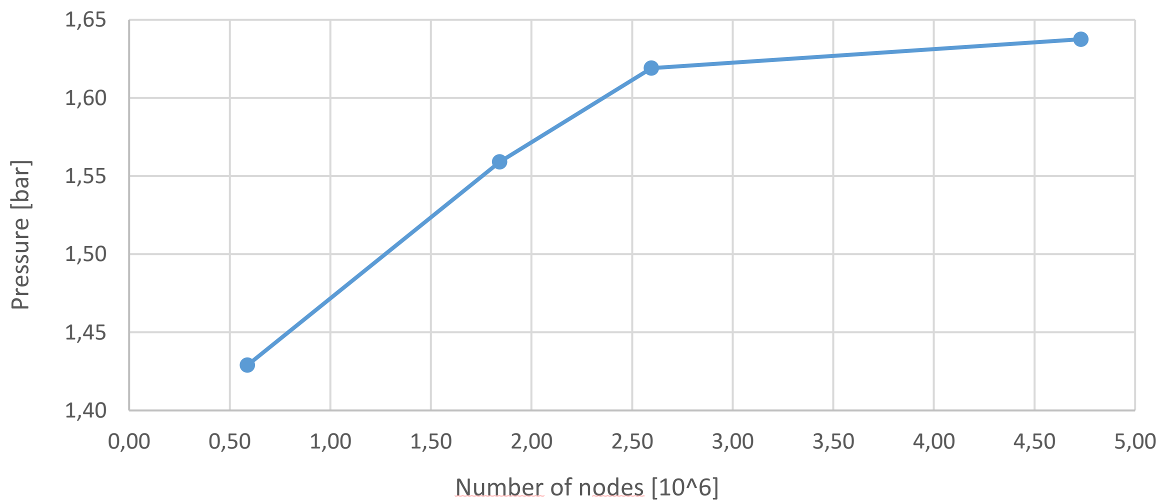

Chart 8 Grid independence: hydraulic circuit pressure drop

The latter simulation presents results slightly closer to the analytical value but its run requires approximately twice the time for each iteration. In conclusion, despite the first approach turn out to be cheaper in terms of computational calculation it is suitable to rely on the analytical results as the geometry of the pipes and the regular laminar flow of the fluid significantly simplify the study of the problem.

4.4 Microchannel pressure testing

The previous chapters show the manufacturing technique and the fluid dynamic behavior of the innovative NA62 microfluidic cooling device, but no feasibility considerations regarding the pressure sealing of microchannels have been made so far. The fluid pressure inside the microchannels can cause component failure, compromising the operation of the whole GTK measuring system. In this regard, it is well known that the failure pressure of a microchannel depends on its width and the thickness of the two joined wafers [26]. This entails a constraint on the geometry of the wider channels (manifolds) and on the minimum thickness of the wafers which goes against the need to minimize the thickness of the cooling plate for measurement purposes. For these reasons, it is important to understand the failure modes and the operating conditions in which they occur. The execution of experimental tests therefore allows to quantify the strength of direct bonding and provides a preliminary quality control that provides a guideline for the continuous improvement of the production process. [27].

This paragraph describes an empirical testing procedure conceived by the CERN PH Department for LHCb and NA62, able to collect a great amount of data with a good repeatability and slight scattering of the results [26]. The protocol includes the following four steps:

1. Testing;
2. Observation under the optical microscope;
3. Writing a report;
4. Packaging of samples in labeled boxes.

These activities are iterated for a large number of LHCb specimens grouped in batches of about twenty units in order to generate a relevant statistical population to be observed. Batches may differ in the thickness of the silicon wafers and they always contain samples whose microchannel width is equal to 500, 350, 200, 100, 50 micrometers respectively. The tests carried out in this analysis concern batches produced in 2017 and 2018 and characterized by the same thickness of the silicon wafers. The individual batches results are compared then each other to certify any improvements in the management of the manufacturing process.

At the end of paragraph, a quick presentation of the results achieved by testing the most recent batch NA62 follows.

4.4.1 Testing

The test consists in the injection of deionized water into a specimen containing a closed hydraulic circuit in order to increase the fluid pressure up to the breaking point. The water is injected into the specimen through a manual hydraulic pump able to manage a maximum pressure of 700 bar and by gradually increasing the pressure.

SAMPLES

To perform numerous tests, it is unthinkable and useless to use prototypes of the entire cooling plate, therefore simpler and cheaper samples have been designed in such a way as to achieve the desired results as well. The specimen has a single inlet and a closed channel both etched into the lower silicon wafer. The inlet leads the fluid coming from the connector described in the next section to the microchannel which is covered at its top by a second wafer joined to the first by direct bonding. The sample is generally characterized by standard and varying dimensions shown in the figure below, but in this analysis the following dimensions are common to all the samples tested.

Size	[mm]
T1	0.14
T2	0.24
D	0.12

Table 23 Dimensions common to LHCb specimens

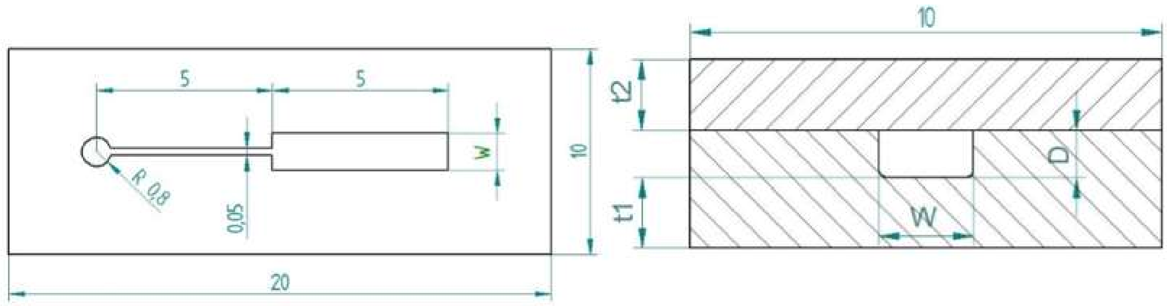

Figure 58 Microchannel sample cross-section [27]

CONNECTOR

The connector is a fundamental component of the test bench as it allows:

- Sample hole alignment to allow water injection;
- Solid clamping to avoid leakage;
- High pressure seals;
- Free failure of the sample.

The connector is designed to test specimens of any size and is housed in a specific slot obtained on a plastic platform installed on the test bench. During the test, the bench is covered by a protective case inserted through two metal prismatic guides with the intention of retaining residual debris caused by breakage.

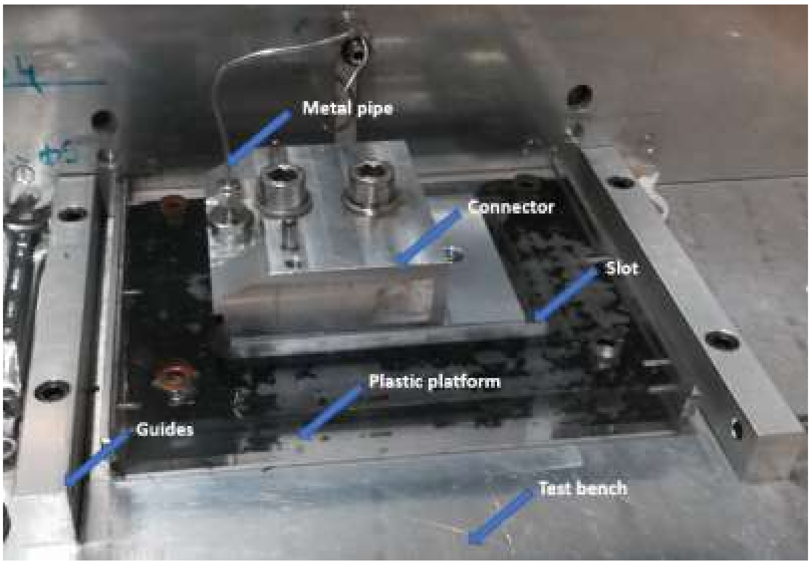

Figure 59 Pressure test bench description

Figure 60 Pressure test safety chamber

The connector has a metal structure divided into two parts aligned by means of two pins in order to form a clamp capable of effectively blocking the specimen. The sample is placed in a slot milled in the lower part of the connector and is tightened thanks to the action of two clamping screws screwed with a torque wrench. The upper part houses a fluidic connector that interfaces directly with a metal pipe that carries the pressurized water inside the sample.

An O-ring is placed between the connector and the inlet hole of the specimen to avoid water leaks, whereas two more gaskets are positioned in the slots provided as a counterbalance. The counterbalance is also achieved in the lower part where there are two machined grooves in which a slip gauge as thick as the sample is inserted.

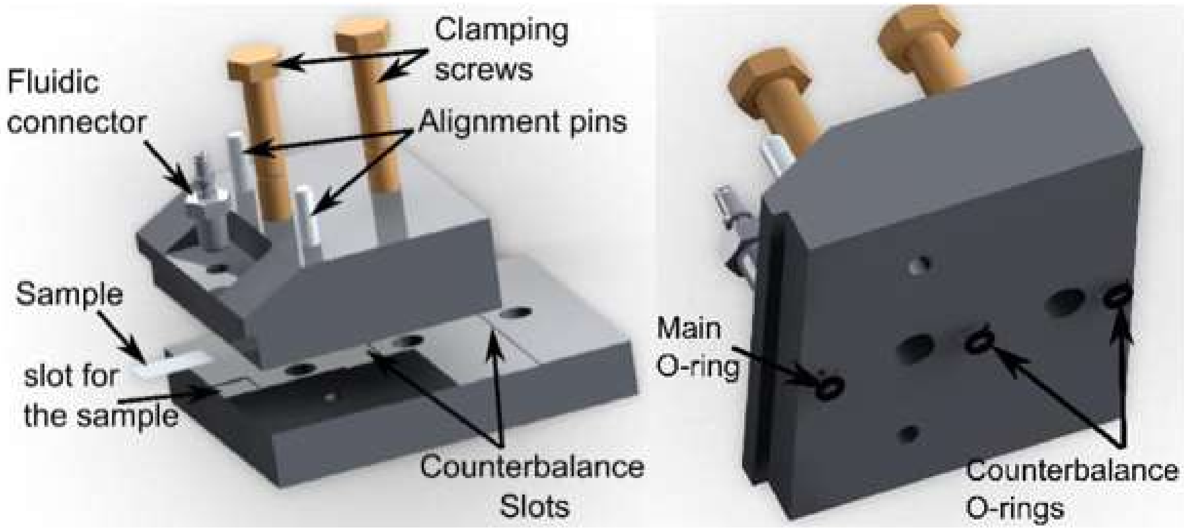

Figure 61 Pressure test connector [27]

DATA ACQUISITION SYSTEM

Data collection is carried out by means of a pressure sensor connected to a data acquisition system managed through a LabView program entitled “Manual water pump”.

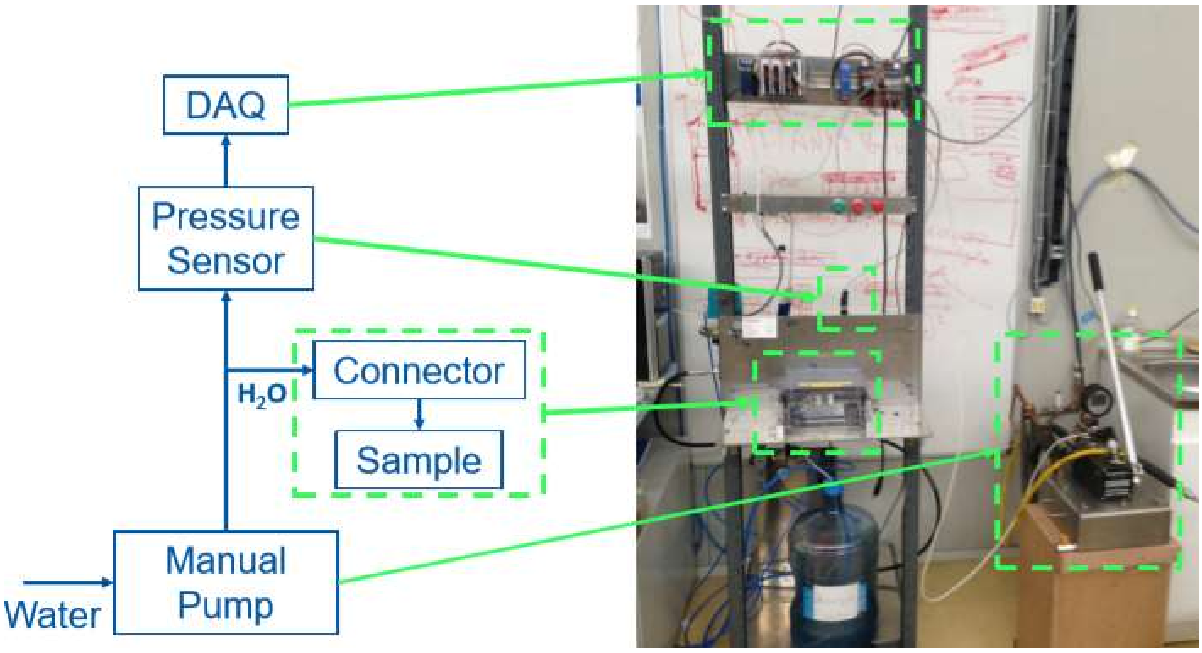

Figure 62 Pressure test bench scheme [27]

The program records and displays the pressure trend inside the specimen on the monitor, reporting in real time the maximum pressure value reached. The breaking point is reached when the system registers a sudden drop in pressure followed by the slight leakage of water from the specimen. Despite this, the breaking point is not reached in some tests because the acquisition system registers a maximum pressure of 600 bar after which the test is stopped.

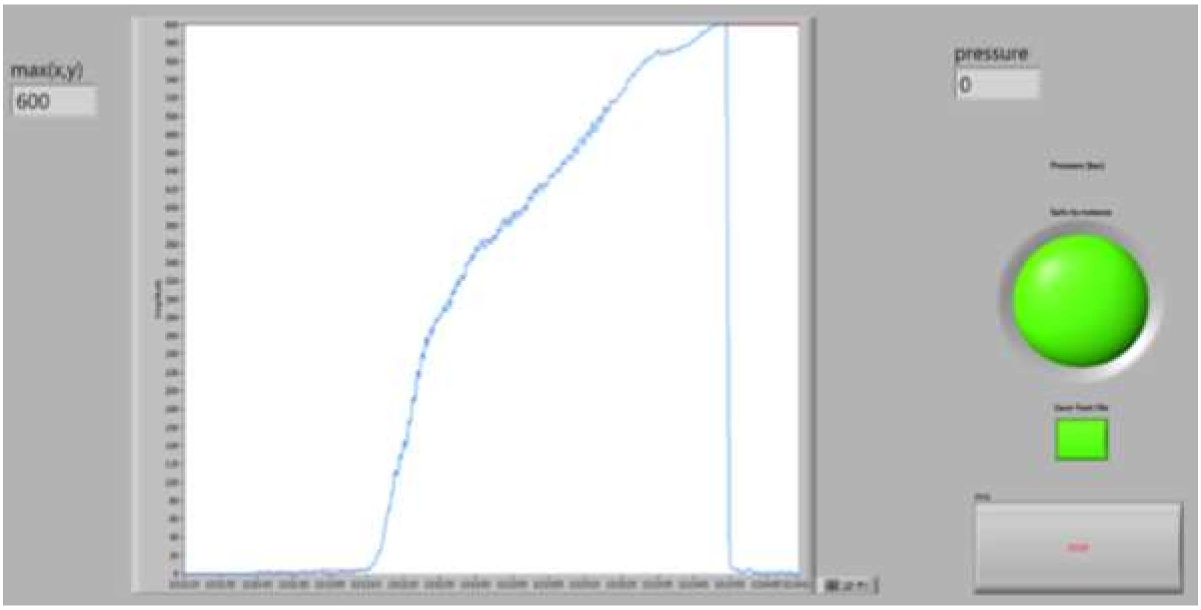

Figure 63 Pressure trend during the test

After recording the maximum pressure value, the setup is restored so as to prepare it for the next test. All the samples of the batch marked by different microchannel width are tested by iterating this standard procedure.

4.4.2 Observation under the optical microscope

The observation phase allows to recognize the failure modes, so it is essential for the preparation of the report and for statistical analysis. Thanks to the Leica optical microscope, it is possible to distinguish six different failure modes that prove the correct manufacture of the components or any problems related to the adhesion of the wafers or the presence of defects. Six different failure modes are identified during the inspection, but only one of these certifies and verifies the technical requirements.

All the failure modes are listed and described below:

Failure Mode	Description
Membrane cover wafer failure (T2) 	This failure mode respects the requirements because it follows the preferential slip planes and starts from the interface between the two wafers. The crack spreads through the cover wafer starting from an area a with a small radius of curvature.
Membrane etched wafer failure (T1) 	The crack spreads through the etched wafer. This fracture mode is not desired because it originates from an area with a radius of curvature greater than that observed in the previous case.
Clamping zone failure 	The crack starts from the inlet hole and does not spread throughout the sample.
Shattered 	The crack starts from the inlet hole and spreads throughout the sample.
T2 and then shattered 	The crack starts from the membrane cover wafer failure area and spreads through the entrance. Before reaching the entrance hole, a crack crosses the sample.
Both wafers failure 	It is a very rare fracture mode and affects both wafers in the microchannel area.

Table 24 Failure modes

A preliminary statistical analysis shows that out of 349 tested samples 234 have reached the breaking point and 115 are tested up to 600 bar without failure. In most cases, the unbroken samples have a width of 100 or 50 micrometers because weaker forces are generated within the microchannel at the same pressure. The results show that about 74% of the samples break properly, while the remaining 26% follow the other five failure modes.

Failure mode	N° of samples	%
Membrane cover wafer failure (T2)	173	73,93
Membrane etched wafer failure (T1)	13	5,56
Clamping zone failure	25	10,68
Shattered	11	4,70
T2 and then shattered	10	4,27
Both wafers failure	2	0,85
Total	234	100

Table 25 Failure modes statistics

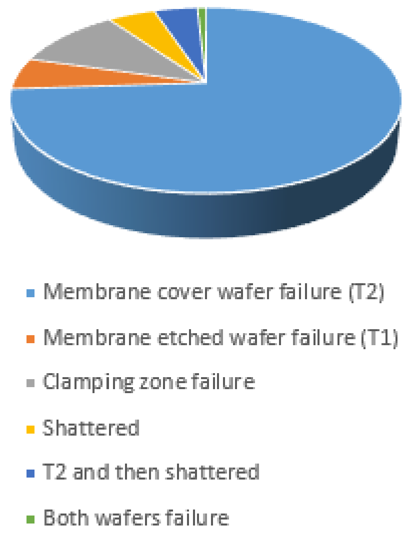

4.4.3 Report

The procedure involves writing a report for each wafer tested, in which the information listed below is reported:

- Project and supplier name;
- Batch and wafer number;
- Testing date and operator;

- Material of the wafers and type of bonding;
- Main dimensions (D, T1, T2);
- Failure pressure;
- Fracture mode and eventual observation;
- Plot of results.

The results are shown on a chart in which the different fracture modes are represented with different symbols and colors. The x-axis plots the microchannel width and y-axis plots the failure pressure. For example, the following chart illustrates the outcome of the test performed for wafer 23 belonging to batch 18S0522.

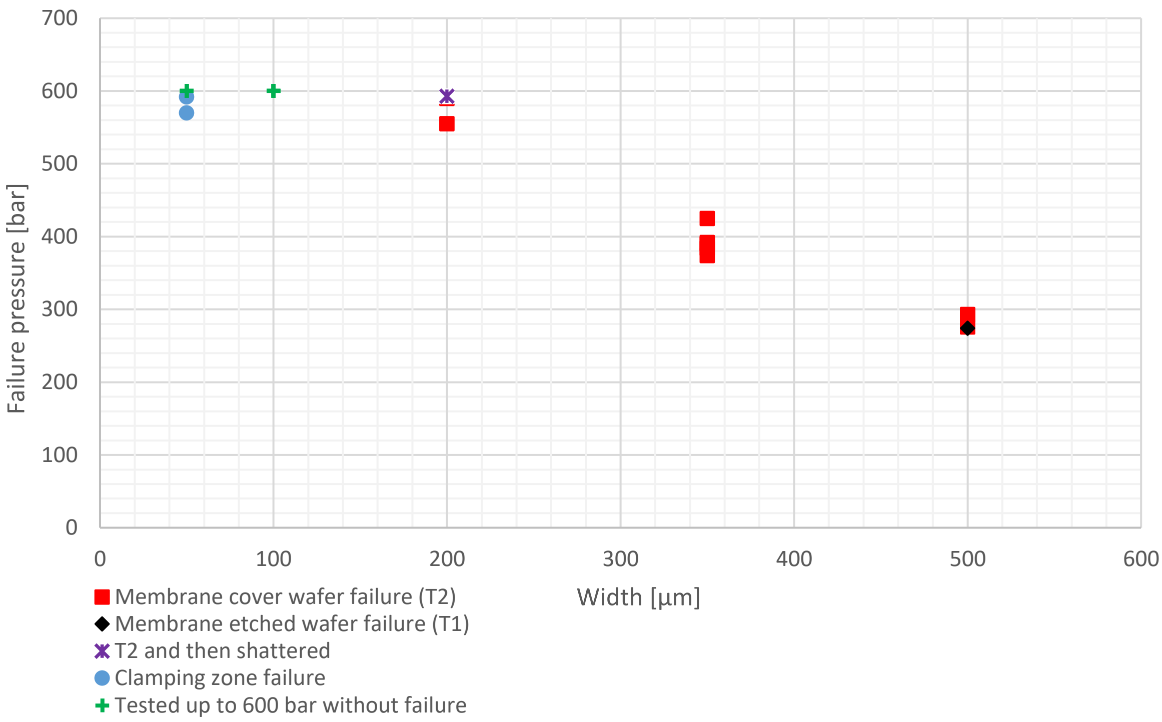

Chart 9 LHCb pressure test D18S0522-P23

The report is then inserted into a database that collects the knowledge base relating to the microchannel fracture mechanics.

4.4.4 Packaging of samples in labeled boxes

The testing procedure ends with the packaging. Groups of samples belonging to the same wafer are thus stored in labeled boxes in order to identify the reference batches.

Figure 64 Labeled box

Finally, the behavior of the samples belonging to the same batch is averaged with the aim of obtaining a comparison between different batches. In this way it is possible to verify the effective improvement of the microchannel performance over time. The graph below illustrates the averaged breaking point trends obtained after testing microchannels belonging to three batches produced in 2018 and a batch dating back to 2017.

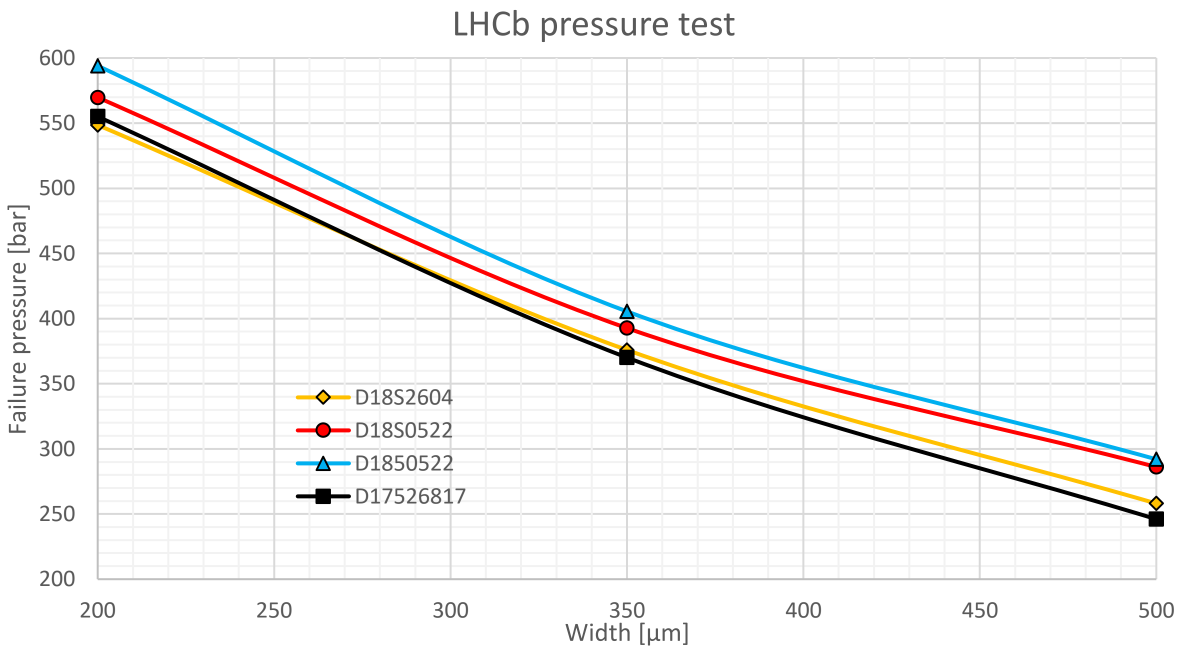

Chart 10 LHCb pressure test

A clear improvement in performance is confirmed by the upward translation of the curves relating to the 2018 batches, but it should be noted that all lots meet the requirements imposed by the LHCb experiment in which microchannel technology is implemented. The upper pressure limits set by the experiment is 150 bar [26], but a greater technical proficiency is continuously sought in order to limit any geometric and operating constraints acting on the future design of such innovative cooling devices.

4.4.5 NA62 samples pressure tests

The NA62 report is discussed separately in this paragraph because only one batch is available for testing. The batch holds fourty eight samples which are not enough to perform a robust statistical analysis, but the results obtained are significant. It emerged that the totality of the specimens shows membrane cover wafer failure and that the failure pressure values detected have a strong repeatability. This is probably due to the different thickness of the specimen wafers displayed in the following table:

Size	[mm]
T1	0.50
T2	0.20
D	0.28

Table 26 Dimensions common to NA62 specimens

It must actually be pointed out that in the LHCb specimens the thickness T1 is less than T2, while here the opposite occurs. This highly promotes the cover wafer failure at the sharp microchannel edge where a higher notch factor exists.

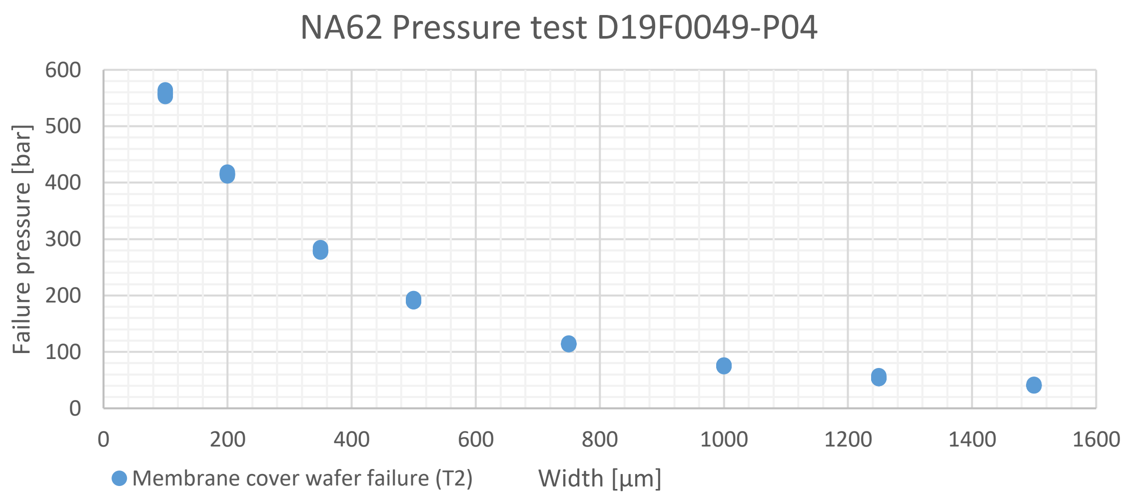

Chart 11 NA62 pressure test D19F0049-P04

In the plot it is possible to verify that the cooling plate manifold 1.60 x 0.28 mm^2 cross-section is resistant to the maximum recorded pressure (1.61 bar) considering that a specimen with a 1.5 x 0.28 mm^2 cross-section can withstand a pressure of about 40 bar.

5. GTK updated heat sink: Cooling Frame

5.1 Setup and preliminary investigations

Chapter 3 ended with the intent of designing a new layout of the cooling system able to improve the measurement accuracy of the third GTK station. A reasonable answer to this question is to reduce the amount of material traversed by the particles in the sensitive area to prevent scattering. This goal can be successfully achieved by removing microchannels placed under the sensor, but this solution implies a total redesign of the cooling system itself. The engineering challenge involves dissipating the same thermal power, benefiting from a limited area to place microchannels. The displayed solution proposes to put microchannels around the sensor, right below the EoC region so as to be in direct contact with the main heat source. Furthermore, to increase the exchange surface and improve the efficiency of the system, the microchannel cross-section has been modified by increasing the depth and decreasing their width. This last action also allows to bring near the channels reducing the pitch and providing the opportunity to add more in parallel.

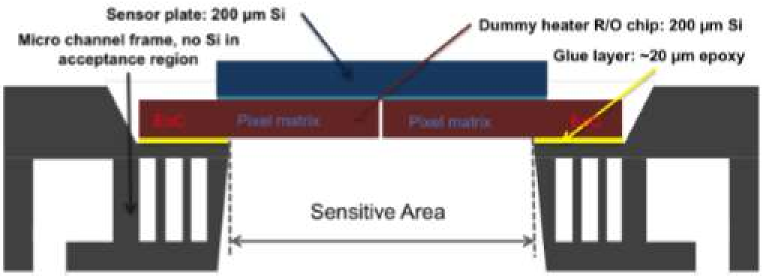

Figure 65 Cooling frame configuration [8]

The aspect ratio is set at 3, resulting in a 100 µm x 300 µm cross-section that respects the constraint discussed in paragraph 4.1 and enables the establishment of a regular pitch equal to 200 µm. This sizing maximizes the depth of the channels, since no stringent constraints are imposed in that region in terms of silicon thickness. In general terms, inlets and outlets can be placed in such a way as to have longitudinal or transverse microchannels as can be seen in figures 66 and 67.

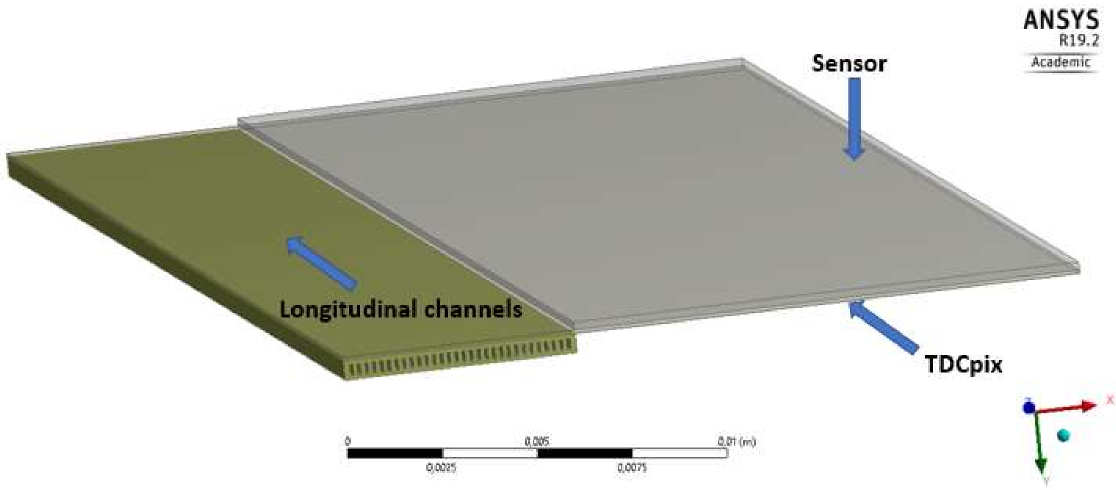

Figure 66 Longitudinal channels layout

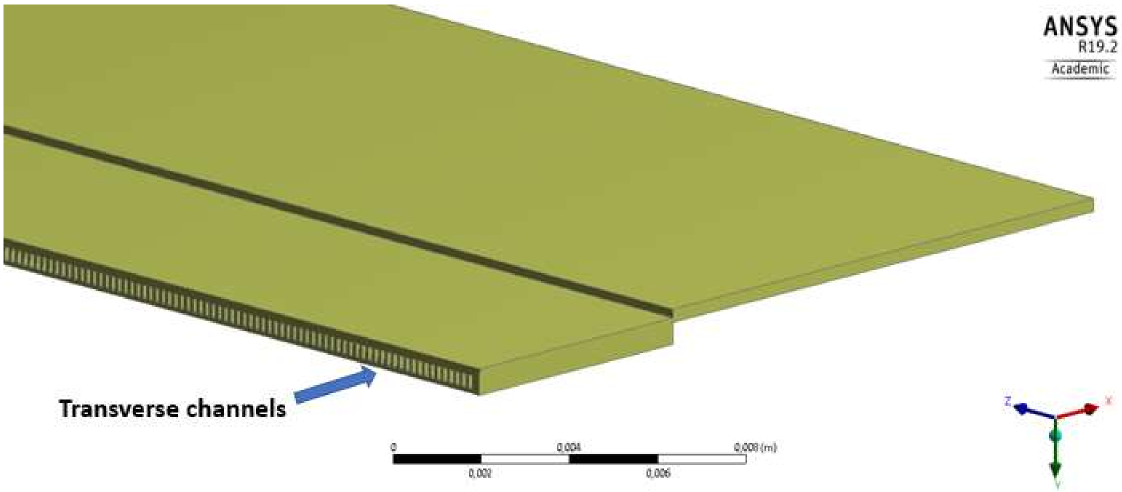

Figure 67 Transverse channels layout

Advantages and disadvantages of these layouts will be explained in the next paragraph, but it is important to first highlight the boundary conditions that arise from this new configuration. In both cases the side walls of the channels are subjected to a constant heat flux density because channels are all located under the EoC region which dissipates a thermal power density of 4.8 W/cm². Moreover, thanks to the high thermal conductivity of the silicon, it is proven by simulation that all points belonging to the lateral surface of a channel at a given coordinate have the same temperature. These two considerations considerably simplify the study of these systems, since by imposing the H1 boundary condition (described in chapter 2) on the side walls of the channels it is possible to analytically describe the heat transfer between the fluid and the adjacent wall. In fact, with an analytical demonstration similar to that presented in paragraph 4.3.2 the fluid bulk temperature and the adjacent wall temperature can be readily calculated and compared with the simulation results. The graphs below show the difference between the trends of the mentioned temperatures obtained from analytical calculation and from the simulations concerning the thermofluidynamic behavior of a representative portion of the physical domain. This domain includes a single longitudinal microchannel used for cooling a part of the upper heating EoC surface of equal length and width equivalent to the pitch between the channels. It is actually sufficient to analyze a single intermediate channel to understand the thermal phenomena in the target area without the influence of any edge effects, being the configuration in parallel. The data relating to the example calculation are listed below:

Data	
Number of channels	41
Pitch	0.15 mm
Channel length	60 mm
Channel width	0.10 mm
Channel depth	0.30 mm
Aspect ratio	3
Hydraulic diameter	0.15 mm
Total mass flow rate	3 g/s
Channel mass flow rate	0.073 g/s
Mean velocity	1.35 m/s

Table 27 Cooling frame thermofluidynamic simulation data

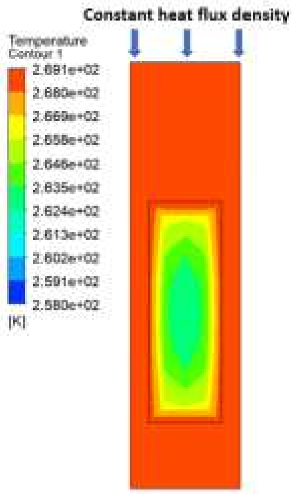

Figure 68 H1 boundary condition

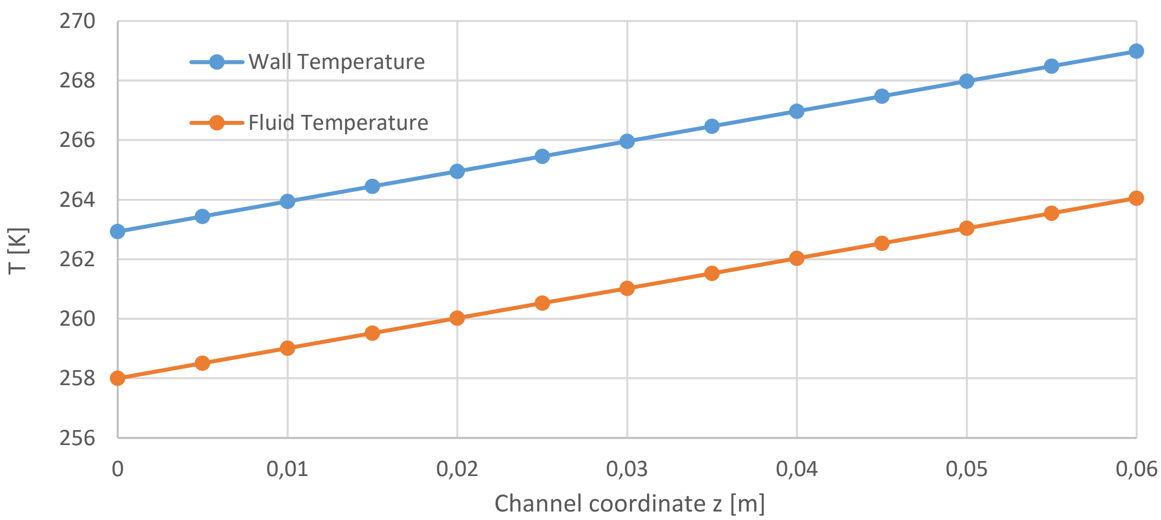

Chart 12 Temperature: analytic solution

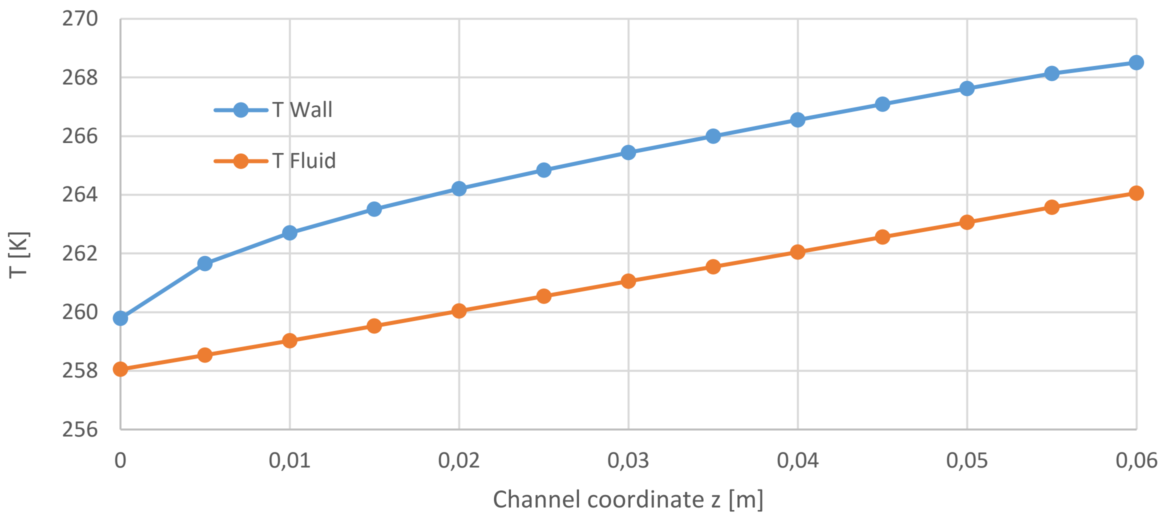

Chart 13 Temperature: simulation solution

The trends are almost identical except near the inlet where the entrance effects modify the regularity recorded by the analytical solution that neglects the fluid development in that area. The numerical values listed in the table validate the simulation output which is not otherwise comparable with experimental results because of the absence of a prototype to be tested at this stage of the project.

Single channel	Outlet bulk temperature	Adjacent wall temperature	Pressure drop
Analytic solution	264.05 K	268.98 K	1.83 bar
Simulation result	264.06 K	268.70 K	1.82 bar

Table 28 Cooling Frame thermofluidynamic simulation results

A further analytical validation of the simulation is presented taking into account even the stretch of fluid development through the evaluation of the Nusselt number, since the value of the applied thermal power density is constant in this case. It is known in the microchannel literature that the Nusselt number has high values at the entrance due to the establishment of the boundary layer and which then tends asymptotically to a defined value after reaching the development of the flow [28]. The asymptotic value depends on the boundary conditions and the proportions of the microchannel cross-section. For H1 boundary condition and an aspect ratio equal to three the Nusselt number is [28]:

$$Nu_{\infty} = 8.235\,(1 - \frac{2.0421}{\alpha} + \frac{3.0853}{\alpha^2} - \frac{2.4765}{\alpha^3} + \frac{1.0578}{\alpha^4} - \frac{0.1861}{\alpha^5} = 4.79 \qquad (5.1)$$

The asymptotic value can also be consulted directly from tables in the literature [18]

Cross-section	Aspect ratio	Nu constant temperature	Nu constant heat flux density	Darcy factor
Rectangular 	1	2.98	3.61	56.92/Re
	2	3.39	4.12	62.20/Re
	3	3.96	4.79	68.36/Re
	4	4.44	5.33	72.92/Re
	6	5.14	6.05	78.80/Re
	8	5.60	6.49	82.32/Re
	∞	7.54	8.24	96.00/Re

Table 29 Nusselt number for different boundary conditions and aspect ratios

The literature also provides a way to calculate the thermal entrance length “l” [28]:

$$l_{th}^{*} = \frac{l}{Re \cdot Pr \cdot D_h} \tag{5.2}$$

Where:

- Re is the Reynolds number;
- Pr is the Prandtl number;
- D_h is the hydraulic diameter;
- l_{th}^{*} is a characteristic length dependent on the aspect ratio [28].

$$\begin{aligned} l_{th}^{*} = -1.275 \cdot 10^{-6} \cdot \alpha^{6} + 4.709 \cdot 10^{-5} \cdot \alpha^{5} - 6.902 \cdot 10^{-4} \cdot \alpha^{4} + 5.014 \cdot \\ \cdot 10^{-3} \alpha^{3} - 1.769 \cdot 10^{-2} \cdot \alpha^{2} + 1.845 \cdot 10^{-2} \cdot \alpha + 5.691 \cdot 10^{-2} \end{aligned} \tag{5.3}$$

$$l_{th}^{*} = 0.043\ m$$

$$Re = \frac{v_m \cdot D_h}{\nu} = \frac{1.35 \cdot 1.5 \cdot 10^{-4}}{8.2 \cdot 10^{-7}} = 247.18$$

$$Pr = \frac{\mu \cdot c_p}{k} = \frac{1.48 \cdot 10^{-3} \cdot 975}{6.27 \cdot 10^{-2}} = 23$$

$$l = l_{th}^{*} \cdot Re \cdot Pr \cdot D_h = 0.037\ m$$

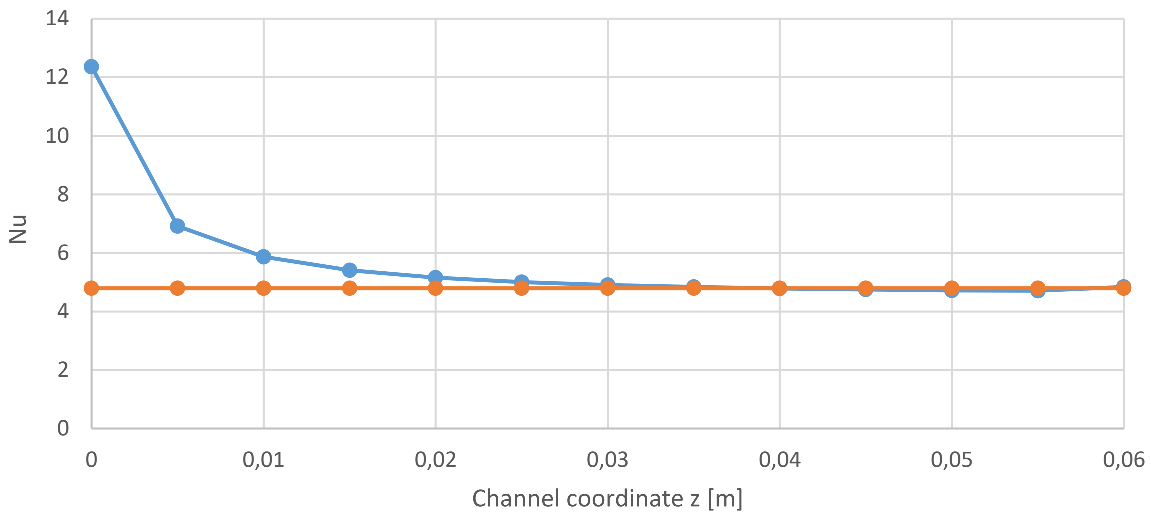

Chart 14 Nusselt number analytic validation

The plot verifies the achievement of the asymptotic Nusselt number and validates the thermal entrance length, proving the correct development of the flow at the inlet.

5.2 Comparison between two alternative layouts

In this paragraph the two different cooling frame configurations proposed in the previous section will be described and compared in terms of:

- Pressure drop;
- Max sensor temperature;
- Max sensor temperature difference;
- Volume of removed material.

Advantages and disadvantages of these alternative approaches for the design of the new cooling system will be shown to understand what could be basically the best solution. It should be noted that thanks to the symmetry of the cooling frame, models representing only half of the domain will be examined for computational savings. Furthermore, all the calculations and simulations presented hereafter refer to a mass flow rate of 3 g/s.

LONGITUDINAL CHANNELS DESIGN

This layout features 30 parallel channels as long as the largest system size. Microchannels are located under the EoC region and have the following properties.

Microchannel cross-section	Rectangular
Number of microchannels	30
Length	60.8 mm
Width	0.1 mm
Depth	0.3 mm
Pitch	0.2 mm

Table 30 Longitudinal microchannel dimensions

The significant length of the channels does not minimize the pressure drop and creates a strong temperature gradient between the inlet and outlet. However, both the maximum sensor temperature and the temperature gradient are within the design specifications.

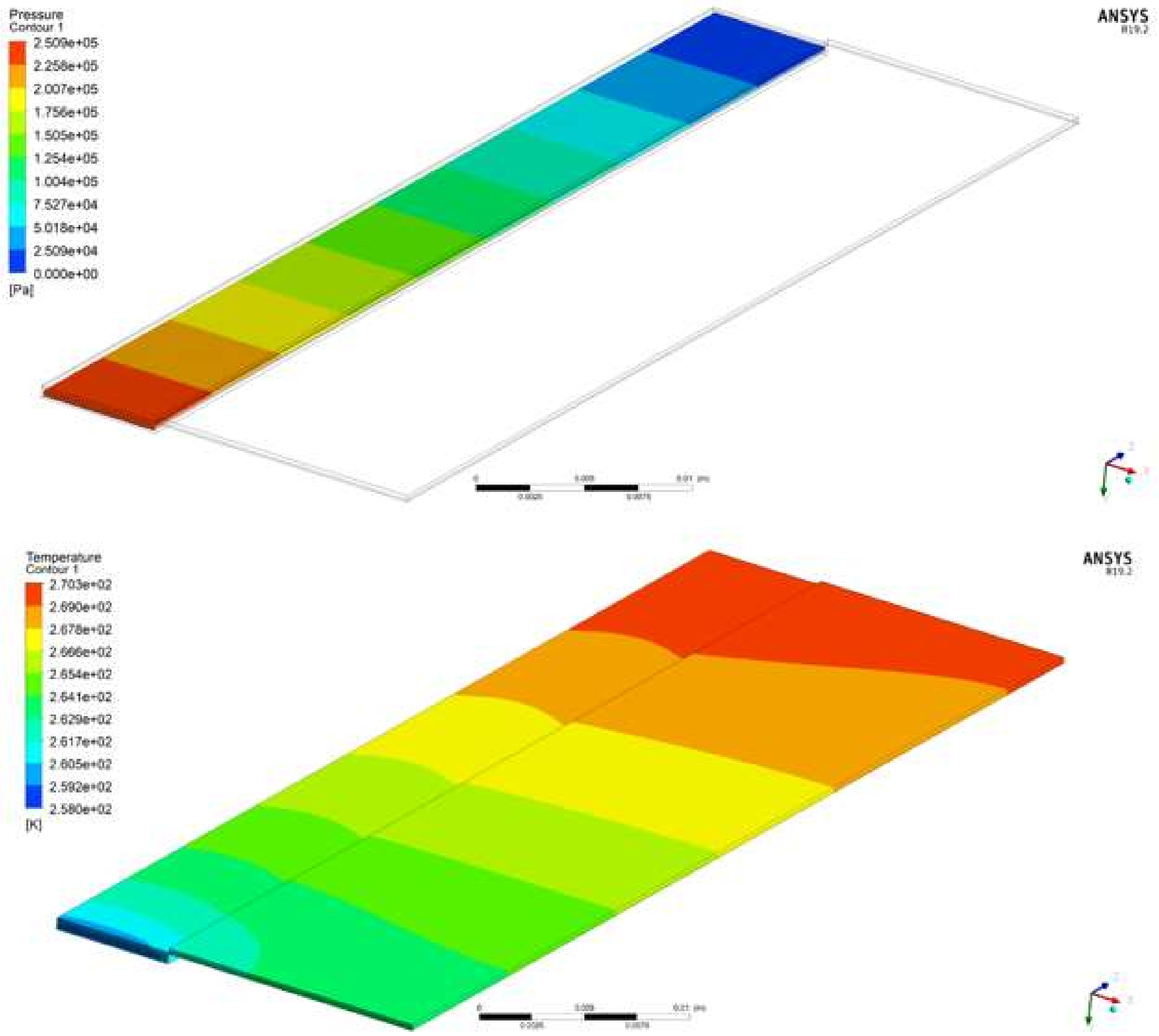

Figure 69 Simulation results. Pressure contour above and temperature map below

Simulation results	
Pressure drop	2.51 bar
Max sensor temperature	270.7 K
Max sensor temperature difference	9 K

Table 31 Longitudinal channels simulation results

It is also interesting to know the volume of material removed if the channels are made by laser etching, since the time and cost of construction mainly depends on this parameter. To reproduce this type of layout it is necessary to remove 54.7 mm^3 of silicon.

TRANSVERSE CHANNELS DESIGN

This layout features 302 parallel channels as long as the smallest EoC size. Microchannels are located under the EoC region and have the following properties.

Microchannel cross-section	Rectangular
Number of microchannels	302
Length	6.2 mm
Width	0.1 mm
Depth	0.3 mm
Pitch	0.2 mm

Table 32 Transverse microchannel dimensions

The small length of the channels minimizes the pressure drop and increases the cooling efficiency. The cold fluid inlet is placed near the sensor to be cooled, reducing the maximum sensor temperatures. Furthermore, since the inlets are all arranged along the side adjacent to the sensor, the temperature gradients turn out to be extremely low. Thanks to the symmetry of this configuration, it is possible to simulate the entire 302 channel system with an extremely simple domain. The representative geometry includes a single intermediate channel used to cool down a portion of heating surface as wide as the pitch between microchannels.

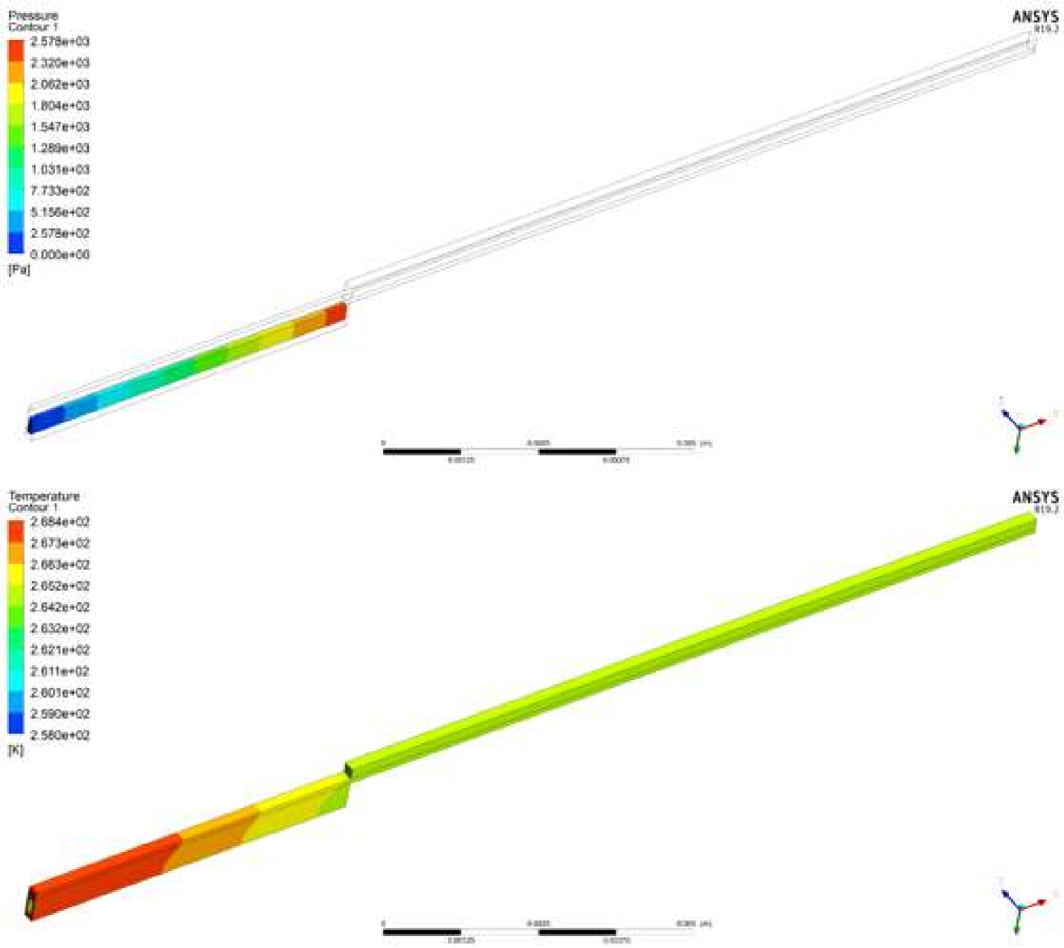

Figure 70 Simulation results. Pressure contour above and temperature map below

Simulation results	
Pressure drop	0.03 bar
Max sensor temperature	264.7 K
Max sensor temperature difference	0.1 K

Table 33 Transverse microchannel simulation results

In this case the quantity of material to be removed is slightly higher than the previous one and it is equal to 56.1 mm³ of silicon.

DISCUSSION OF FINDINGS

Except for the amount of material to be removed, the cross-channel configuration undoubtedly seems to guarantee greater performance, but at this stage of the analysis it is also necessary to consider how to effectively fill the microchannels. In this regard, the two layouts will be examined as a whole by introducing the manifolds that distribute and collect the fluid circulating in the microchannels.

LONGITUDINAL CHANNELS SYSTEM

In the longitudinal channel configuration, the introduction of manifolds does not imply changes in geometry to the layout described above. Manifolds can be easily placed at the ends of the microchannels in order to serve all thirty channels respecting the overall dimension restrictions. The orientation of the manifolds must be perpendicular to the direction of the channels to limit the lateral dimensions in order to fit within the space provided for the construction platform. The figure below shows a potential suitable sizing for the cooling frame which even preserves the laminar flow (Re = 2100) in the entire system.

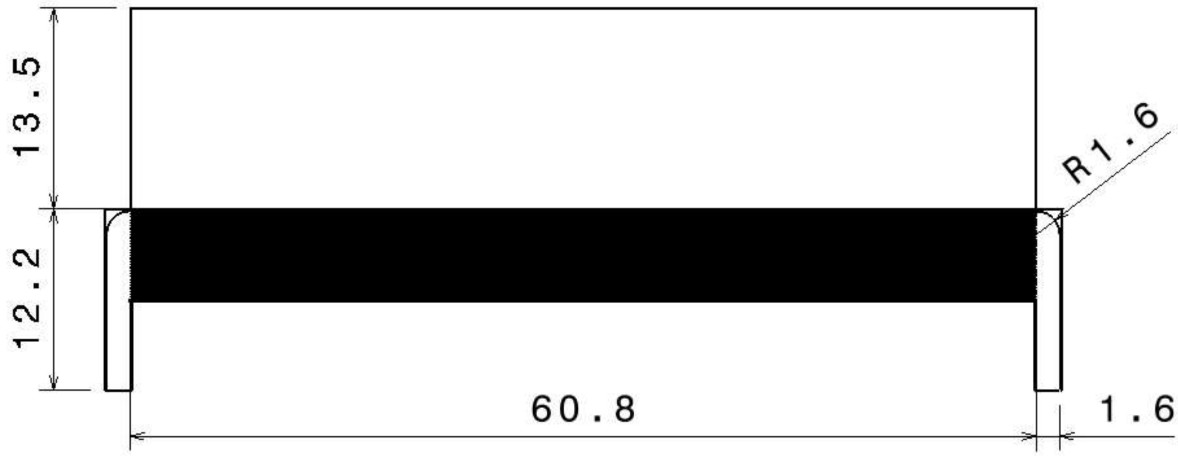

Figure 71 Main longitudinal channels layout dimensions

Both ducts are etched into the lower wafer and covered at the top by a second wafer as occurs in the creation of the channels. The cross-section is as deep as the channels to reduce the concentrated load losses and has a width of 1.6 mm to ensure matching with the connectors described in the paragraph 4.2.3. As regards performance, the pressure drop is calculated by adding the contribution of the two manifolds to the previously calculated value.

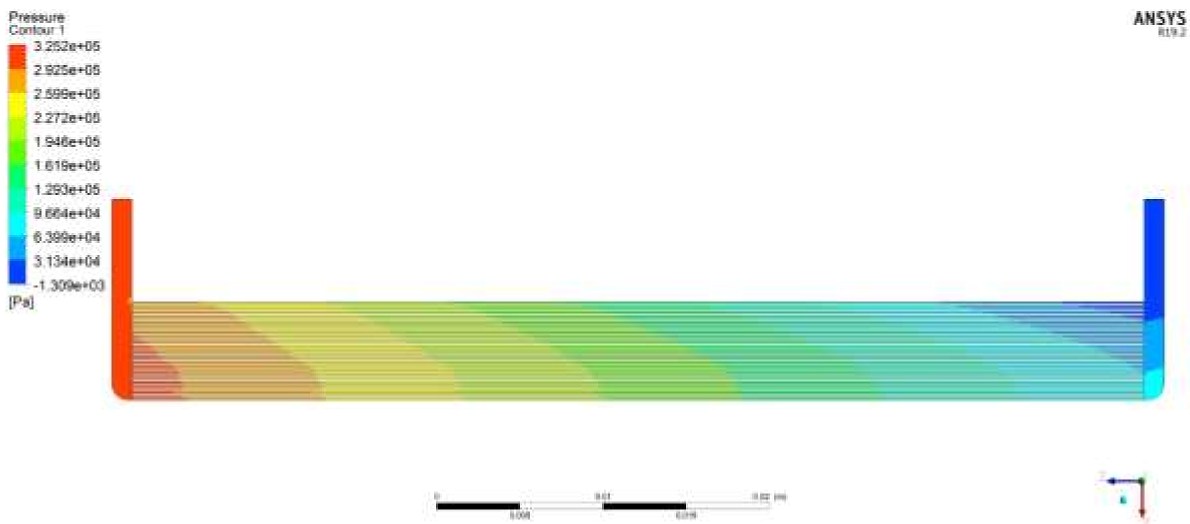

Figure 72 Longitudinal channels layout pressure contour

Pressure drop	
Microchannels	2.51 bar
Manifolds	0.73 bar
Total	3.24 bar

Table 34 Longitudinal channels layout pressure drop

The overall result slightly exceeds the pressure drop constraint (3 bar) but is still acceptable because the design limit provided is to be considered indicative. Regarding instead the thermodynamic behavior of the system, it is sufficient to rely on the contours shown previously in figure 2 because, as mentioned before, the introduction of the manifolds does not make any design changes to the microchannels layout.

TRANSVERSE CHANNELS SYSTEM

As a matter of principle, the cross-channel configuration appears to be the most effective cooling solution, but further investigations are needed because the introduction of manifolds involves deep changes in the geometry of the system. The manifolds are both integrated in the silicon plate here as well and must distribute and collect the circulating fluid in 302 channels without taking up space under the sensor or overly reducing the length of the microchannels. It is therefore required that the inlet manifold width is small but at the same time large enough to effectively distribute the fluid within the channels. The output manifold is sized like the input manifold to respect the symmetry of the hydraulic circuit, but it does not affect the performance of the channels because it is not located below the EoC area. Both manifolds have approximately the same sensor length and a rectangular cross-section whose dimensions are expressed in table 35.

Manifold geometric dimensions	
Length	60.55 mm
Width	0.9 mm
Depth	0.3 mm

Table 35 Transverse channel layout manifold main dimensions

With this arrangement, manifolds are as deep as the microchannels to reduce the concentrated pressure drops and the length of the channels decreases up to 5.6 mm. Two pipes etched in the silicon are also required to interface the manifolds to the KOVAR connectors, but they cause an increase in fluid dynamic losses.

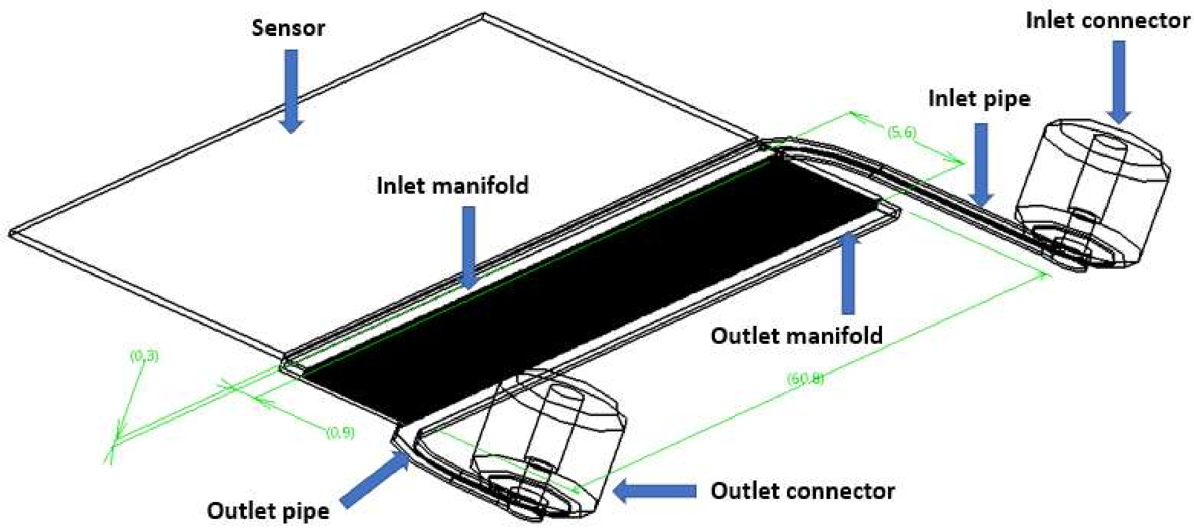

Figure 73 Transverse microchannels layout main dimensions

Feeding the circuit with a mass flow rate of 3 g/s the flow in the pipes and manifolds is probably not laminar due to the narrow duct cross-sections. The resulting high velocity of the fluid inside them raises the Reynolds number (Re = 3300) by moving the analyzed problem to the transition zone of the Moody diagram and so reducing the reliability of the simulation outcome. To ensure a laminar flow rate inside the manifolds and pipes it would be necessary to limit the flow rate to 2 g/s (Re = 2200), but in this way the comparison with the longitudinal channel system would not be consistent. For this reason, the simulation values collected under standard flow conditions are shown below.

Simulation results	
Pressure drop in the inlet pipe	0.70 bar
Pressure drop in the model	1.51 bar
Pressure drop in the outlet pipe	0.54 bar
Total pressure drop	2.75 bar
Max sensor temperature	277.4 K
Max ΔT in the sensor	15 K

Table 36 Transverse microchannels layout simulation results

The domain is divided into three parts to reduce the maximum computational burden required in terms of the number of finite elements, since the pipes and the core body of the system are arranged in series.

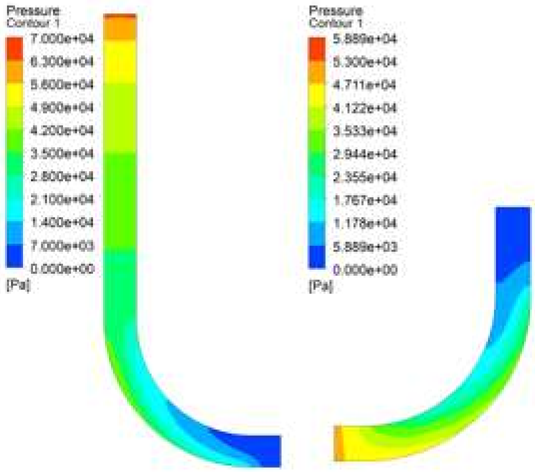

Figure 74 Pressure drop in the inlet and outlet pipes

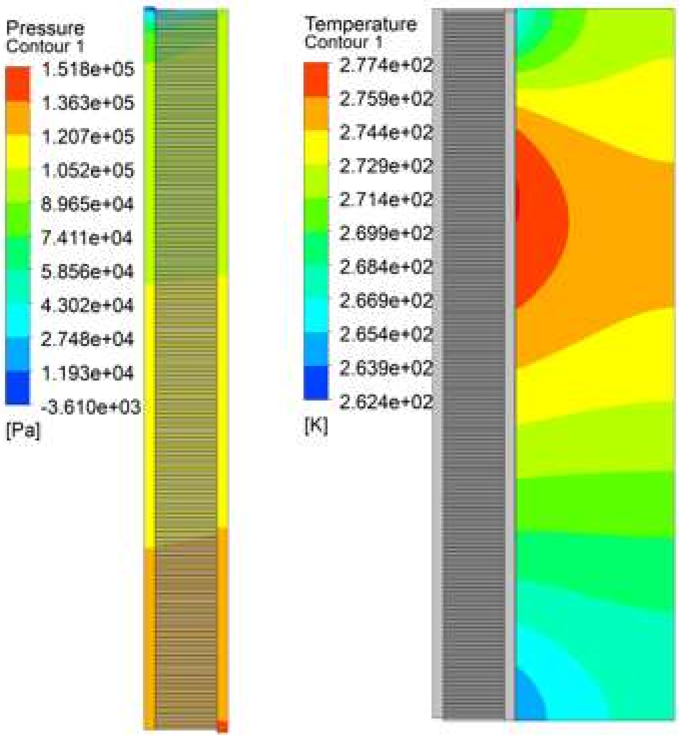

Figure 75 Simulation results. Pressure contour on the left and temperature map on the right

All the parameters except the maximum temperature difference of the sensor respect the design requirements, but results deviate considerably from the expectations. It should be noted that the greatest deviations are recorded especially in terms of homogeneity of the sensor temperature which is the greatest theoretical strength of this configuration. This lack of performance is mainly due to the introduction of the inlet manifold which distributes the fluid into the channels with a variable temperature as the fluid flowing in the manifold heats up on its way to the last channels. Furthermore, the inclusion of the manifold reduces the length of the channels and consequently also the heat exchange surface. Regarding instead the maximum temperature, the peak is recorded before the end of the inlet manifold because the simulation shows a marked slowdown in the flow in the intermediate channels. This irregular flow is due to a software calculation error resulting from the too small size of the manifold which cannot distribute the fluid effectively.

CONCLUSIONS

Because of the problems arising with the implementation of manifolds in the transverse channels layout, the configuration with longitudinal channels is definitely preferred. This solution is straightforward and easy to implement in the silicon platform. Moreover, the steadily laminar fluid flow makes it more reliable and ready to be analyzed with CFD simulations or analytical calculations.

5.3 Fluid flow optimization

In the previous paragraph, the regularity of the fluid flow within the longitudinal channel system is not assessed, or even how the flow characteristics change as the geometry of the pipes varies. By observing the contour representing the value and direction of the coolant speed in the domain, it is possible to judge the regularity of the flow and the contingent generation of vortices that hinder the smooth operation of the hydraulic circuit. Figure 76 shows the velocity distribution in the inlet manifold with a 1 mm tip radius.

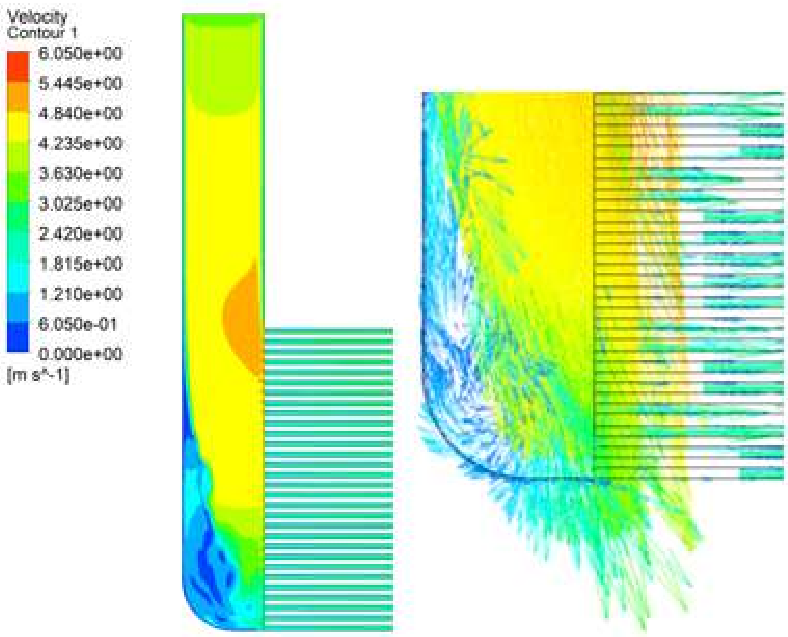

Figure 76 Distribution of velocity vectors around the 1mm tip radius

The manifestation of vortices at the end of the pipe requires a progressive reduction of the manifold width in order to facilitate the access of the fluid into the microchannels. The solution may include a modification of the shape of the duct or simply an increase of the tip radius.

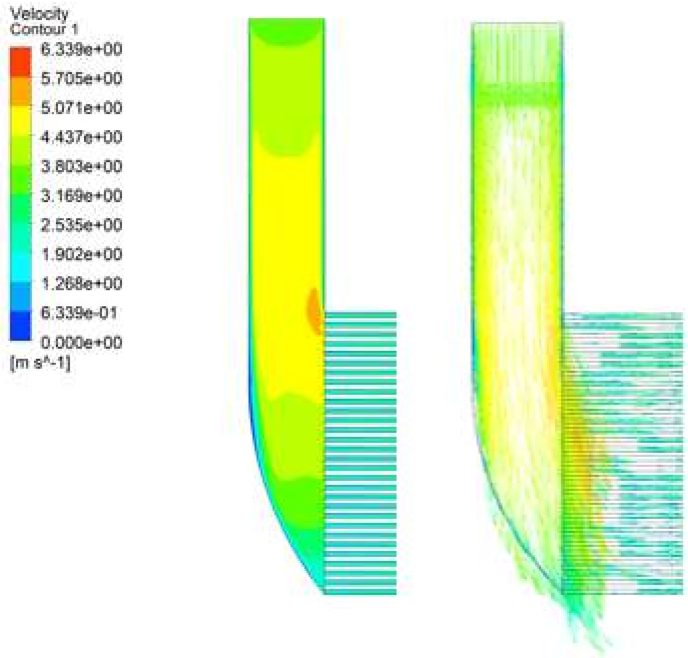

Figure 77 Distribution of velocity vectors around the 7mm tip radius

Figure 77 shows that with a tip radius of 7 mm, the generation of vortices is successfully avoided. On the other hand, there is no flow irregularity along the outlet manifold.

5.4 Cooling Frame mechanical stability

This chapter discusses the mechanical stability of the cooling frame through a structural simulation to evaluate the maximum deflection of the electronic component considering the self-weight of the sensor and the TDCpix pixel area as the load. The static behavior of the heat sink is neglected in the design of the device currently implemented in the GTK because the cooling plate also acts as a support for the electronics. On the other hand, the lack of support material in the cooling frame could cause a deflection of the electronics that could damage the fragile bump-bonds, compromising the operation of the spectrometer. The system is shaped like a silicon plate as thick as the sensor and the TDCpix joined together and placed on two supports along the larger sensor size. The side surfaces of the plate are considered as stuck to render the continuity of silicon, whose properties are listed in the following table.

Material properties	
Density	2330 kg/m³
Young modulus	131 GPa
Tensile yield strength	62000 MPa

Table 37 Silicon mechanical properties

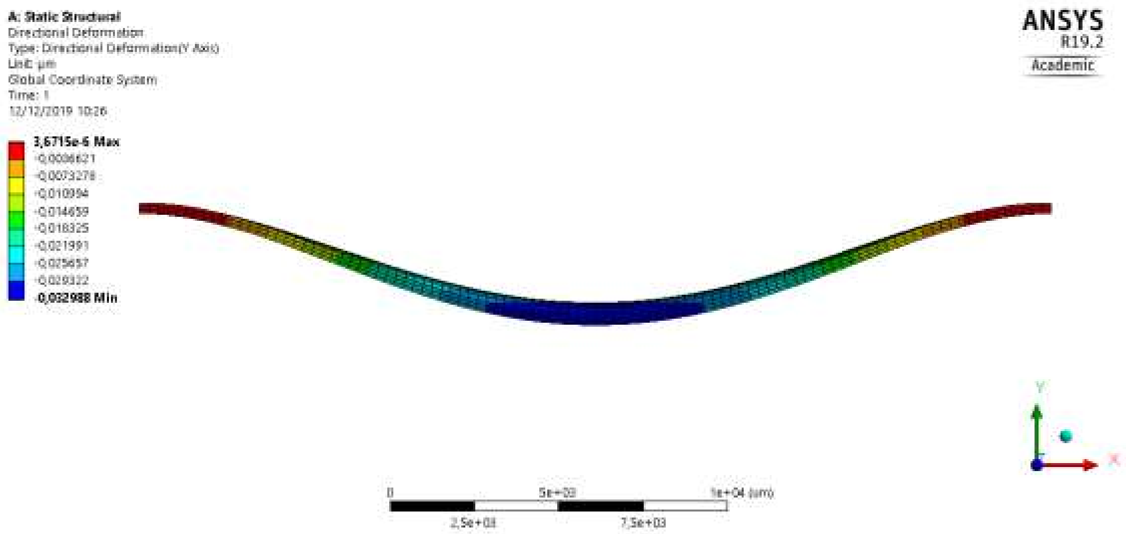

Figure 78 Silicon plate deflection

A maximum inflection of 3 µm is recorded, so there is no risk of breaking the bump bonds.

6. Conclusions

6.1 Discussion of findings

In this work the design of a HEP detector cooling has been deeply investigated. Considering the project requirements, it has been proved that the cooling can benefit from the introduction of microchannel technology. The analyses have confirmed that the integration of microchannels in a silicon cooling plate complies with the strict technical specifications, providing a more detailed knowledge of its thermofluidynamic behavior. In this regard, CFD simulations results have been successfully validated through analytical calculations and experimental data. Referring to the simulation outcome, experimental pressure tests in the workshop have proved the microchannel mechanical resistance to operating pressures recorded. Afterwards, two different microchannel production techniques have been presented, accompanied by the documentation of the quality assessment carried out in the EPFL clean room in Lausanne. In a further step, the opportunity to reduce the scattering of the acquired data has led to the development of a new configuration for the GTK cooling system with zero material budget in the sensitive area. Two different layouts have been proposed highlighting their peculiarities and disadvantages in order to choose the most suitable solution. Simulation results have motivated the choice pursued also acting as a valid tool for the optimization of flows and for the verification of structural stability.

6.2 Outlook

In chapter 4 the difficulties encountered in the validation process of thermodynamic simulations has been explained in detail. Using a thermal imaging camera may overcome the adhesion problems between the resistance thermometers and the sensor surface, but some problems related to light reflection have been detected so far. In this regard, efforts are being made to have thermal imaging cameras reliable enough to reproduce temperature distributions and validate simulations more accurately in the near future.

On the other hand, the cooling frame updating is moving forward with the design and manufacture of the first prototype. Microchannels will be produced by DRIE etching technique while the two silicon wafers will be joined via anodic bonding thanks to the interposition in the middle of a thin layer of glass. The use of anodic bonding together with some slight geometric changes aims to lower the cost of the prototype by simplifying the production process. CFD models have already been updated to fit the slightly different geometry of the prototype, but further simulations are needed to optimize the shape of manifolds. The next steps will involve the drafting of the entire prototype assembly and the design of the photolithography mask, in order to start production as soon as possible. It is expected that the ultimate cooling frame will be installed in the third GTK station in occasion of the next data taking scheduled for 2021. Its implementation will lead to scattering reduction and significant measurement improvements and it will represent a new step for the continuous technological development of the NA62 experiment setup.

Bibliography

[1] Experimental investigation and empirical correlations of single and laminar convective heat transfer in microchannel heat sinks: Yuling Zhai, Guodong Xia, Zhouhang Li, Hua Wang;

[2] Numerical investigation of fluid flow and heat transfer effects in minichannels and microchannels under h2 boundary condition: Viral Dharaiya;

[3] CERN official website;

[4] Low Mass Integrated Cooling: Alessandro Mapelli;

[5] The NA62 GigaTracker: a low mass high intensity beam 4D tracker with 65 ps time resolution on tracks: G. Aglieri Rinella, D. Alvarez Feito, R. Arcidiacono, C. Biino, S. Bonacini, A. Ceccucci, S. Chiozzi, E. Cortina Gil, A. Cotta, Ramusino, H. Danielsson, J. Degrange, M. Fiorini, L. Federici, E. Gamberini, A. Gianoli, J. Kaplon, A. Kleimenova, A. Kluge, R. Malaguti, A.Mapelli, F. Marchetto, E. Martín Albarrán, E. Migliore, E. Minucci, M. Morel, J. Noël, M. Noy, G. Nüessle, L.Perktold, M. Perrin-Terrin, P. Petagna, F. Petrucc,i K. Poltorak, G. Romagnoli, G. Ruggiero, B. Velghe, H. Wahl;

[6] L'esperimento NA62: INFN website;

[7] The beam and detector of the NA62 experiment at CERN: E. Cortina Gil et al 2017 JINST 12 P05025;

[8] Development of a novel micro channel cooling system for the NA62 GTK detector: Nüessle Georg;

[9] I rarissimi decadimenti del mesone k. L'esperimento NA62 del CERN presenta i suoi ultimi risultati: INFN website;

[10] L'esperimento NA62 al CERN: AISF website;

[11] A 3D numerical study of heat transfer in a single-phase micro-channel heat sink using graphene, aluminum and silicon as substrates: Ahmed Jassim Shkarah, Mohd Yusoff Bin Sulaiman, Md Razali Bin Hj Ayob, Hussein Togun, 2013;

[12] Numerical investigation of fluid flow and heat transfer effects in minichannels and microchannels under h2 boundary condition: Viral Dharaiya, 2011;

[13] Single-phase heat transfer in microchannels: The importance of scaling effects: P. Rosa, T.G. Karayiannis, M.W. Collins, 2009;

[14] Effect of pumping power on the thermal design of converging microchannels with superhydrophobic walls: Hamidreza Ermagan, Roohollah Rafee, 2018;

[15] Etching technology for microchannels: R. Willem Tjerkstra, Meint de Boer, Erwin Berenschot, J.G.E. Gardeniers, Albert van den Berg, Miko Elwenspoek MESA Research Institute, University of Twente;

[16] MNX MEMS and Nanotechnology exchange web site;

[17] Deep reactive-ion etching: Wikipedia;

[18] Termodinamica e trasmissione del calore: Yunus A. Çengel;

[19] Principles of heat and mass transfer: F. P. Incropera, D.P. Dewitt, T.L. Bergman, A.S. Lavine, Wiley 2013;

[20] Effect of hydraulic diameter and aspect ratio on single phase flow and heat transfer in a rectangular microchannel: Amirah M. Sahar, Jan Wissink, Mohamed M. Mahmoud, Tassos G. Karayiannis, Mohamad S. Ashrul Ishak;

[21] The NA62 Gigatracker, from silicon microchannel cooling plates to tracking detectors: A. Mapelli, vertex 2017;

[22] Microfabricated silicon substrates for pixel detectors assembly and thermal management: aka Silicon Microchannel Cooling Plates: A. Mapelli, 2019;

[23] Ansys Fluent 12.0 User's Guide;

[24] Theoretical Microfluidics: H. Bruus, Oxford University Press, 2008;

[25] Design of a compact cooling system for the future ITS off-detector electronics in the ALICE experiment at CERN: C. Cantarello;

[26] Silicon micro-fluidic devices for high energy physics applications: Testing procedure and failure analysis, Oussama Fliss, 2015;

[27] Pressure test bench scheme Pressure Testing of ScSi MicroChannels, D. Alvarez, J. Degrange, A. Mapelli, J. Noel, October 2017;

[28] Handbook of single-phase convective heat transfer: S. Kakac, R.K. Shah, W. Aung;

[29] Reynolds Number: R. Shankar Subramanian, Clarkson University;

[30] Tabelle e diagrammi perdite di carico acqua: Marco Doninelli and Mario Doninelli, Caleffi;

[31] Le perdite di carico nei circuiti idraulici: Luigi Fanizzi, ECOACQUE.

List of figures

List of charts

List of tables

Acknowledgement

I would like to thank Prof. Vladimir Viktorov and Prof. Carlo Ferraresi for the supervision and for having entrusted me with this Master Thesis project. I would also like to thank INFN Turin for providing the tools, software and hardware necessary for carrying out the studies and for financing all the activities developed this year. I am grateful to thank Flavio Marchetto for his scientific support, for visiting the facility and establishing direct contact with the NA62 collaboration. Finally, I would like to thank the NA62 collaboration and, specifically, Mathieu Perrin Terrin and Alessandro Mapelli for the close cooperation and experience at the EPFL in Lausanne.